VOLUME VIII
ISSUE II

JOURNAL OF
MATHEMATICAL SCIENCES
AND MODELLING

Language Editor

Tolga Aktürk
Yıldız Technical University
TÜRKİYE

Technical Editor

Arzu Öztürk Özkoç
Duzce University
TÜRKİYE

Ayla Erdur Kara
Tekirdag Namık Kemal University
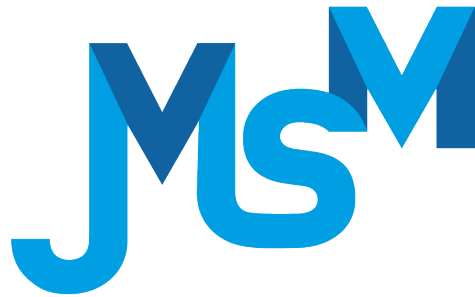TÜRKİYE

iii

Contents

Journal of Mathematical Sciences and Modelling

Research Article

Modelling and Chaotic Based Parameter Optimization of Sliding Mode Controller

Muhammed Salih Sarıkaya[1*], Onur Demirel[1], Sezgin Kaçar[2] and Adnan Derdiyok[1]

[1]*Department of Mechatronics Engineering, Faculty of Technology, Sakarya University of Applied Sciences, Sakarya, Türkiye*
[2]*Department of Electrical and Electronics Engineering, Faculty of Technology, Sakarya University of Applied Sciences, Sakarya, Türkiye*
Corresponding author

Article Info

Abstract

This study presents a sliding mode controller design for DC motor speed control using optimization algorithms. The design of sliding mode controllers typically requires expert input during the parameter determination phase. Traditionally, these parameters are set through trial-and-error methods based on the experience of specialists. However, this approach can be both time-consuming and costly. The application of optimization methods automates the parameter-tuning process, reducing human intervention and, in turn, minimizing both design time and costs. The goal of this study is to enhance the performance of optimization methods by hybridizing them with chaotic systems. The random structures of chaotic systems allow optimization algorithms to explore a broader solution space, thereby improving their performance. The analyses conducted in this study reveal that hybrid chaotic algorithms outperform their original ones. The data indicate that the use of hybrid algorithms generally leads to a decrease in Steady-State Error. Additionally, it is observed that when all hybrid algorithms are employed, the sliding mode controller does not exhibit any overshoot. The results demonstrate that the sliding mode controller performs effectively, achieving low settling time, rise time, and steady-state error, while also preventing chattering. Among the methods examined, the sliding mode controller optimized with the Chaotic Henry Gas Solubility Optimization algorithm delivers the best performance, ensuring optimal system stability.

1. Introduction

Sliding Mode Controllers (SMCs) are recognized as an important controller in nonlinear dynamic system control, known for their robustness and efficiency. One of the most important advantages of these controllers is their robustness to system uncertainties and disturbances. SMCs are widely applied in fields such as robotics, aerospace, electric vehicles, energy systems, and automotive industries. However, to maximize the performance of a sliding mode controller, precise tuning of specific controller parameters is essential. The accurate selection of these parameters is critical for system stability. Traditionally, determining controller parameters has been done through trial and error, which is a time-consuming and complex process. This problem can be overcome by optimization methods. Optimization methods allow the sliding mode controller parameters to be tuned more efficiently. These methods simplify controller design, reduce human intervention, and enhance system performance.

Optimization methods help to identify the most suitable parameters or strategies for a given system or process, thereby reducing costs, increasing efficiency and improving processes. In the context of control systems, optimization methods serve as a crucial tool for enhancing controller performance and making the system more robust. Moreover, in recent years, hybrid approaches have been developed to improve the performance of optimization methods. One such approach involves hybridizing optimization methods with chaotic systems. Due to their high sensitivity and randomness, chaotic systems facilitate a broader exploration of the solution space in optimization processes, leading to better results.

One of the commonly used optimization methods in the literature is the Henry Gas Solubility Optimization (HGSO) algorithm. This algorithm simulates gas solubility behavior, providing a robust foundation for optimization tasks in various fields such as machine learning and control systems [1, 2]. Furthermore, it can be further enhanced by integrating with other metaheuristic algorithms, such as Simulated Annealing (SA), Harris Hawk Optimization (HHO), and the Aquila Optimizer (AQO) [3–6]. The hybridization of HGSO with other metaheuristic algorithms has been shown to enhance the algorithm's performance in terms of solution accuracy and convergence speed. Additionally, there are applications of hybridizing the HGSO algorithm with opposition-based learning (OBL) strategies. Studies such as OBL/HGSO for PID parameter optimization and CNN-OBL/HGSO for autonomous vehicle systems have been conducted [7, 8]. To overcome certain limitations in engineering designs, researchers are increasingly using chaotic systems, characterized by sensitivity to initial conditions and complex, unpredictable behavior. The integration of chaotic dynamics into optimization algorithms has been shown to enhance the algorithms' capabilities to escape local optima and improve convergence rates [9, 10]. For instance, chaotic maps provide a more structured level of randomness compared to traditional random processes, allowing optimization algorithms to explore the solution space more effectively [10]. This is particularly important in the context of the HGSO algorithm, as chaotic hybridization can improve the search capabilities of the HGSO algorithm by diversifying the exploration strategies used during optimization.

The random behaviors of chaotic systems within a structured framework have led to their hybridization with various metaheuristic optimization methods. The studies in the literature related to this are as follows; Chaotic PID-controlled Particle Swarm Optimization (PSO), logistic and tent map PSO for complex functions, chaotic quantum particle swarm optimization with support vector regression (SVRCQPSO), hybrid multi-stage probabilistic selection particle swarm optimization supported by sine chaotic inertial weight and symmetric tangent chaotic acceleration coefficients (MPSPSO-ST), chaotic PSO for fuzzy system parameter optimization, singer chaotic map hybrid PSO for laser cutting problems (LPSPSO), quantum evolutionary algorithm for chaotic search strategy (QEA), evolutionary algorithms hybridized with chaotic mapping-based Aquila optimizer (CMAOE), chaotic multi-objective evolutionary algorithms, chaotic simulated annealing for the traveling salesman problem, wavelet chaotic simulated annealing neural network for the traveling salesman problem (WCSANN), chaotic simulated annealing for multi-task optimization problems, chaotic whale optimization algorithm for production scheduling problems, chaotic whale optimization algorithm tested with benchmark functions, and hybrid whale optimization algorithm with fractional chaotic map for parameter estimation in wind-diesel power systems [11–26].

In this study, a sliding mode controller has been designed for the speed control of a DC motor. The parameters of the sliding mode controller have been tuned by using optimization methods. Henry Gas Solubility Optimization (HGSO), Particle Swarm Optimization (PSO), Whale Optimization Algorithm (WOA), Simulated Annealing (SA), and Evolutionary Algorithms (EA) optimization methods have been employed. To examine the effects of chaotic systems on optimization methods, these algorithms have been hybridized with the Rössler, Duffing-Van Der Pol, and Sprott-A chaotic equations [27]. The results of the Chaotic Henry Gas Solubility Optimization (CHGSO), Chaotic Particle Swarm Optimization (CPSO), Chaotic Whale Optimization Algorithm (CWOA), Chaotic Simulated Annealing (CSA), Chaotic Evolutionary Algorithms (CEA), HGSO, PSO, WOA, SA, and EA algorithms have been compared.

The paper consists of five sections. The first section provides a brief introduction and an evaluation of recent studies. The second section presents information about the HGSO and CHGSO methods, as well as the chaotic system used. The third section deals with the optimization of sliding mode controller (SMC) parameters for DC motor speed control. In the fourth section, the performances of the optimization methods are compared. The fifth section presents an evaluation of the findings and the conclusions.

2. Materials and Methods

2.1. Henry gas solubility optimization algorithm

The Henry Gas Solubility Optimization Algorithm is a physics-based optimization method. This method is based on Henry's Law, which defines the relationship between the solubility of gases in liquids and the pressure of the gas on the liquid. According to Henry's Law, at a constant temperature, the solubility of gases in a liquid is directly proportional to the partial pressure of the gas. This algorithm considers various factors that affect the solubility of gases in a liquid and aims to increase the solubility level of the gas within the system [28].

The HGSO algorithm takes place in 8 steps.

Step 1. Initialization process: The number of gases (population size N) and their positions are initialized according to the following equation:

$$X_i(t+1) = X_{min} + r * (X_{max} - X_{min}) \tag{2.1}$$

The initial positions of the gas particles are established using equation (2.1). Here, X_{min} and X_{max} define the boundaries of the problem, r is a random number between 0 and 1, and X_i denotes the position of the ith gas particle within the gas particle population. The initial values for Henry's constant, the partial gas pressure, and the constant (enthalpy) are assigned according to the following equation.

$$
\begin{aligned}
H_j(t) &= l_1 * r \\
P_{ij}(t) &= l_2 * r \\
C_j(t) &= l_3 * r
\end{aligned}
\tag{2.2}
$$

According to equation (2.2), H_j denotes the Henry constant of the cluster j, P_{ij} represents the partial gas pressure of the ith gas particle within cluster j, C_j is the enthalpy constant of cluster j and t indicates the number of iterations. It is important to note that l_1, l_2 and l_3 are constant values, with $l_1 = 0.05$, $l_2 = 100$ and $l_3 = 0.01$ [28].

Step 2. Clustering: The gas particle population is segmented into clusters that each contain an equal number of gas particles. Because the clusters consist of similar gases, the Henry and enthalpy constants are uniform across the clusters.

Step 3. Evaluation: Each gas particles within the clusters are assessed using the objective function. Following this assessment, the gas particles are ranked from best to worst results.

Step 4. Updating the Henry constant: The Henry constant is updated according to equation (2.3).

$$H_j(t+1) = H_j(t) * e^{-C*[\frac{4}{T(t)} - \frac{1}{T^0}]}$$
$$T(t) = e^{-\frac{t}{iter}}$$

(2.3)

In equation (2.3), H_j represents Henry's constant of cluster j, T denotes temperature, $T^0 = 298.15K$ is the reference temperature [28], t refers to the current iteration, and *iter* is the total number of iterations.

Step 5. Updating the solubility: Gas solubility is updated according to equation (2.4).

$$S_{ij}(t) = K * H_j(t+1) * P_{ij}(t)$$

(2.4)

According to equation (2.4), S_{ij} represents the solubility of ith gas particle in cluster j, P_{ij} denotes the partial gas pressure of ith gas particle in cluster j, and K is a constant value.

Step 6. Updating the positions: The positions of gas particles are updated according to equation (2.5).

$$X_{ij}(t+1) = X_{ij}(t) + F * r * \Upsilon * (X_{ibest}(t) - X_{ij}(t)) + F * r * a * (S_{ij}(t) * X_{best}(t) - X_{ij}(t))$$
$$\Upsilon = \beta * e^{-\frac{F_{best}(t)+\varepsilon}{F_{ij}(t)+\varepsilon}}$$
$$\varepsilon = 0.05$$

(2.5)

In equation (2.5), X_{ij} is the position of ith gas particle in cluster j, while r is a random number ranging from 0 to 1. X_{ibest} refers to the position of optimal gas particle, and X_{best} denotes the position of optimal gas particle within the entire population. The parameter Υ indicates the capability of the ith gas particle in cluster j to interact with other gases in its cluster. Parameter a defines the influence of gas particles on the $i^{th}h$ gas particle in cluster j (a=1), while β is a constant value. F_{ij} represents the value of the objective function for the ith gas particle in cluster j, whereas F_{best} refers to the value of the objective function for the optimal gas particle across the entire population. Additionally, F is a flag (F=±1) that alters the direction of movement for the gas particle's position.

Step 7. Escape from local optima: To escape the local optimum, the gas particles are organized, and the less effective gas particles are identified. The selection process is carried out according to equation (2.6).

$$N_w(t) = N * (r * (M_2 - M_1) + M_1)$$
$$M_1 = 0.1$$
$$M_2 = 0.2$$

(2.6)

Here, N is the gas particle number, N_w is the inferior gas particle number to be selected.

Step 8. Updating the positions of the worst agents: The positions of the gas particles chosen in step 7 are randomly updated within the global boundaries of the problem.

$$G_{ij}(t+1) = G_{min} + r * (G_{max} - G_{min})$$

(2.7)

According to equation (2.7), G_{ij} represents the position of ith gas particle in cluster j and G_{min}, G_{max} denotes the global boundaries of the problem. For clearer comprehension of the HGSO method, the pseudocode for the optimization algorithm is provided in Algorithm 2.1.

1:     Initialization X_i (i = 1, 2,... N), number of gas types i, H_j, P_{ij}, C_j, l_1, l_2 and l_3. equations (2.1) and (2.2)
2:     Divide the population agents into the number of gas types (cluster) with the same Henry's constant value H_j.
3:     Evaluate each cluster j.
4:     Get the best gas X_{ibest} in each cluster, and the best search agent X_{best}.
5:     **while** t < maximum number of iterations **do**
6:       **for** each search agent **do**
7:         Update the positions of all search agents using equation (2.5)
8:       **end for**
9:       Update Henry's constant of each gas type using equation (2.3)
10:     Update solubility of each gas using equation (2.4)
11:     Rank and select number of worst agents using equation (2.6)
12:     Update the position of the worst agents using equation (2.7)
13:     Update the best gas X_{ibest}, and the best search agent X_{best}.
14:     **end while**
15:     $t = t + 1$
16:     **return** X_{best}

Algorithm 2.1: Pseudo-code of HGSO algorithm [28]

2.2. Chaotic Henry gas solubility optimization algorithm

Chaotic systems are dynamic systems that exhibit unpredictable behaviors due to their sensitivity to initial conditions, despite having a deterministic structure. Among the most prominent characteristics of these systems are complexity, extreme sensitivity, and cyclic structures. These features of chaotic systems present significant opportunities in optimization processes. In particular, chaotic structures enhance the exploration capabilities of optimization algorithms, enabling them to avoid local optima and closer to global solutions.

The hybridization of optimization methods with chaotic systems utilizes the complex nature of these systems as an advantage, thereby enhancing algorithm performance. This hybridization is typically implemented by integrating chaotic maps into optimization algorithms. For example, the use of chaotic behavior in the exploration phases of traditional optimization algorithms expands the search area and increases the probability of finding an optimal solution.

Hybridization is particularly successful in reducing the time to solution and improving the quality of the solutions obtained. The literature indicates that hybrid optimization methods provide higher success rates. For these reasons, the Rössler chaotic system (2.8), the Duffing-Van Der Pol Chaotic System (2.9), and the Sprott-A chaotic system (2.10) have been selected for hybridizing the HGSO algorithm in this study [27, 29]. The equation and initial conditions for the Rössler chaotic system are provided below.

$$\begin{aligned} \dot{x} &= -y - z \\ \dot{y} &= x + a * y \\ \dot{z} &= b + z * (x - c) \end{aligned} \tag{2.8}$$

The parameters and initial conditions are $a = 0.2, b = 0.2, c = 5.7; x(0) = -9, y(0) = 0, z(0) = 0$, respectively [30].

$$\begin{aligned} \dot{x} &= y \\ \dot{y} &= a * (1 - x^2) * y - x^3 + b * cos(c * z) \\ \dot{z} &= 1 \end{aligned} \tag{2.9}$$

The parameters and initial conditions are $a = 0.2, b = 5.8, c = 3; x(0) = 0, y(0) = 0, z(0) = 0$, respectively [27].

$$\begin{aligned} \dot{x} &= y \\ \dot{y} &= y * z - x \\ \dot{z} &= 1 - y^2 \end{aligned} \tag{2.10}$$

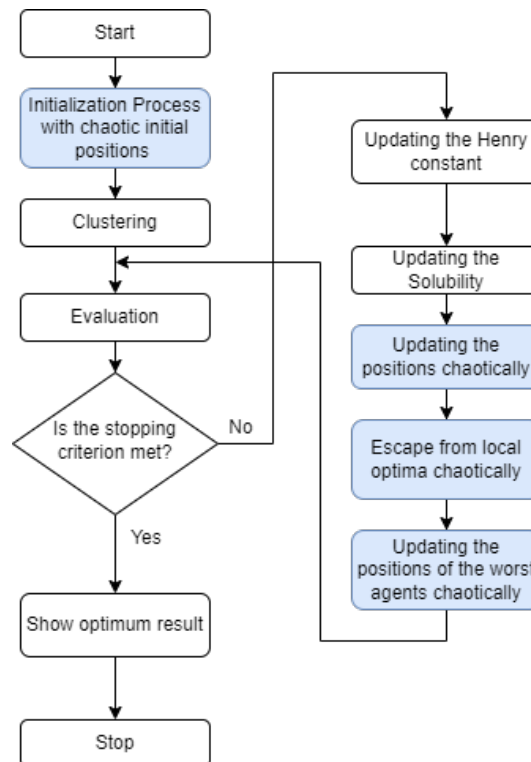The initial conditions are $x(0) = 0, y(0) = 1, z(0) = 0$ [29].

Figure 2.1: CHGSO Flowchart diagram [27]

The main objective of this study is to boost the performance of the HGSO algorithm by utilizing the advantages and features offered by chaotic systems. Unpredictability, which is the main feature of these systems, plays an important role in increasing the effectiveness of optimization algorithms. Chaotic systems, due to their inherently complex structures, contribute to the creation of a richer and more effective search space when integrated into algorithms. The non-repetitive and ergodic properties of chaotic systems enable the development of a broader and efficient search strategy in stochastic searches. This property suggests that randomness can be used in optimization processes. Specifically, the randomness in chaotic systems becomes an effective tool for improving the overall performance of the algorithm when combined with randomly generated numbers (r) and the equations (2.1),(2.2),(2.5),(2.6),(2.7) [27]. When the HGSO algorithm is hybridized with the Duffing–Van der Pol, Rössler, and Sprott-A chaotic systems, the resulting methods are denoted as $C_{d-v}HGSO$, C_rHGSO, and C_sHGSO, respectively. The flow diagram of the CHGSO algorithm is presented in Figure 2.1 to provide a clearer understanding of the chaotic updates integrated into the HGSO algorithm.

3. Modeling of Sliding Mode Controller for a DC Motor Application

The block diagram of the conventional SMC is presented in Figure 3.1.
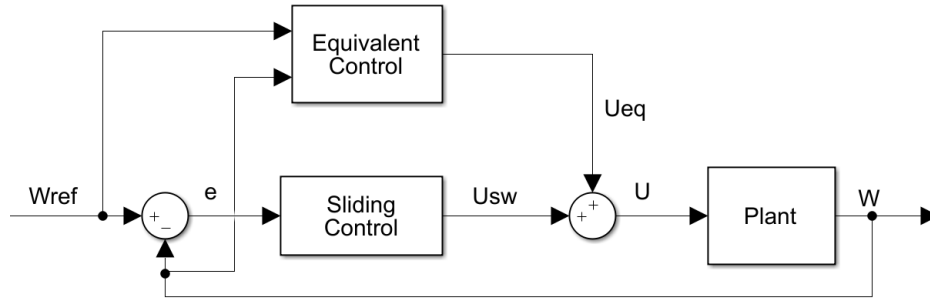
Figure 3.1: Block diagram of the conventional SMC

The control signal applied to the U motor, the equivalent control signal (U_{eq}), and the switching control signal (U_{sw}) are presented in Figure 3.1. The speed control of a DC motor has been implemented using SMC. The transfer function obtained for the speed control of the DC motor is as follows;

$$\frac{\omega(s)}{V_a(s)} = \frac{\frac{K_t}{JL_a}}{\left(\left(\frac{s+R_a}{L_a}\right)\left(\frac{s+B}{J}\right) + \frac{K_bK_t}{JL_a}\right)}. \tag{3.1}$$

The mathematical model of the DC motor is given in equation (3.1). In equation (3.1), V_a is the applied voltage to the motor, R_a is the resistance of the motor windings, L_a is the inductance of the motor windings, K_b is the electrical constant, J is the moment of inertia, B is the damping constant, K_t is the mechanical constant, and ω is the angular velocity of the motor. In this study, the parameters of DC motor [27], which were simulated for speed control, are presented in Table 3.1.

Parameter	DC motor
$R_a(\Omega)$	0.517
$L_a(H)$	0.0573
B	0.000244
$J(kgm^2/s^2)$	0.00000145
$K_b(Vs/rad)$	0.0112
$K_t(Nm/A)$	0.0112
reduction ratio	1/52

Table 3.1: The parameters of the DC motor

For simplicity, the following variables have been defined in equation (3.2).

$$A = \frac{K_t}{JL_a}$$
$$D = \frac{R_a}{L_a} + \frac{B}{J} \tag{3.2}$$
$$E = \frac{R_a}{L_a} * \frac{B}{J} + \frac{K_bK_t}{JL_a}$$

When the variable definitions are substituted into equation (3.1), the following equations (3.3)-(3.7) are obtained:

$$\frac{\omega(s)}{V_a(s)} = \frac{A}{s^2 + Ds + E} \tag{3.3}$$

$$\ddot{\omega}(t) + D\dot{\omega}(t) + E\omega(t) = AV_a \tag{3.4}$$

$$\begin{aligned} x_1 &= \omega(t) \\ x_2 &= \dot{x}_1 = \dot{\omega}(t) \\ \dot{x}_2 &= \ddot{\omega}(t) \end{aligned} \tag{3.5}$$

$$\begin{aligned} X &= \begin{bmatrix} x_1 & x_2 \end{bmatrix}^T \\ y &= x_1 = \omega(t) \\ u &= V_a(t) \end{aligned} \tag{3.6}$$

$$\dot{x}_2 = \ddot{\omega}(t) = -D\dot{\omega}(t) - E\omega(t) + AV_a. \tag{3.7}$$

In the design of SMC, the first step should be the design of the sliding surface. Typically, the switching function is chosen as a linear form of the state variables, as shown in equation (3.8) [31].

$$\begin{aligned} s(X) &= \begin{bmatrix} s_1(X) & s_2(X) & \cdots & s_m(X) \end{bmatrix}^T \\ C &= \begin{bmatrix} c_1^T & c_2^T & c_3^T & \cdots & c_m^T \end{bmatrix}^T \\ s(X) &= CX \end{aligned} \tag{3.8}$$

In traditional SMC, the expression commonly used for designing the sliding surface is in the form given by equation (3.9). Here, $\lambda \in \mathbb{R}^+$ Present a positive number denoting the gradient of the sliding surface, and n denotes the system order [31].

$$s(X,t) = \left(\frac{d}{dt} + \lambda\right)^{n-1} e(t) \tag{3.9}$$

For example, in the case of a second-order system, the surface equation is given in equation (3.10).

$$s(X,t) = \left(\frac{d}{dt} + \lambda\right)^{2-1} e(t) = \lambda e(t) + \dot{e}(t) \tag{3.10}$$

In SMC, during the design of the surface, where $s(X,t) = \dot{s}(X,t) = 0$ the error approaches zero. Therefore, the sliding mode is defined as given in equation (3.11).

$$\begin{aligned} s(X,t) &= \lambda e(t) + \dot{e}(t) = 0 \\ \dot{s}(X,t) &= \lambda \dot{e}(t) + \ddot{e}(t) = 0 \end{aligned} \tag{3.11}$$

The condition that ensures the system states reach or move towards the sliding surface is called the reaching condition. When the system is under the reaching condition, its trajectory is in the reaching phase [31]. There are various approaches to the reaching condition in sliding mode control, and the Lyapunov function is widely used. The Lyapunov function is represented by the following equation (3.12).

$$V(s) = \frac{1}{2} s^2(t) \tag{3.12}$$

Here, for stability, the conditions $V > 0$ and $\dot{V} < 0$ must be satisfied.

$$\dot{V}(s) = \frac{1}{2} \frac{d}{dt} s^2(t) \leq -\eta |s(t)| \tag{3.13}$$

In equation (3.13), $\eta \in \mathbb{R}^+$ denotes a positive real number. When the derivative of $V(s)$ is taken, the stability condition described above transforms into the form shown in equation (3.14).

$$\dot{s}(t) \leq -\eta \, \text{sign}(s(t)) \tag{3.14}$$

According to equation (3.14), since there is a condition for reaching $s(t) = 0$ in finite time, it is referred to as the reaching condition. For $\eta > 0$, the system state trajectories will reach the sliding surface $s(t) = 0$ and remain on that surface.

In SMC, for the design of the sliding surface, equation (3.15) can be used, and by utilizing equation (3.16) for the derivative of the sliding surface function, if its derivative is set equal to zero. By substituting into the equation and simplifying, the following equations (3.17)–(3.21) are obtained.

$$s(t) = Ce(t) + \dot{e}(t) = C(\omega_r(t) - \omega(t)) + (\dot{\omega}_r(t) - \dot{\omega}(t)) \tag{3.15}$$

$$\dot{s}(t) = 0 = -K\,\text{sign}(s(t))$$
$$\dot{s}(t) = C(\dot{\omega}_r(t) - \dot{\omega}(t)) + (\ddot{\omega}_r(t) - \ddot{\omega}(t)) = 0 = -K\,\text{sign}(s(t)) \tag{3.16}$$

$$\dot{s}(t) = C(\dot{\omega}_r(t) - \dot{\omega}(t)) + \ddot{\omega}_r(t) - (-D\dot{\omega}(t) - E\omega(t) + uA) = -K\,\text{sign}(s(t)) \tag{3.17}$$

$$\dot{s}(t) = (C\dot{\omega}_r(t) - C\dot{\omega}(t)) + \ddot{\omega}_r(t) + D\dot{\omega}(t) + E\omega(t) - uA = -K\,\text{sign}(s(t)) \tag{3.18}$$

$$\dot{s}(t) = (C\dot{\omega}_r(t) - C\dot{\omega}(t)) + \ddot{\omega}_r(t) + D\dot{\omega}(t) + E\omega(t) + K\,\text{sign}(s(t)) = -u(t)A \tag{3.19}$$

$$u(t) = \frac{1}{A}\left[C\dot{\omega}_r(t) - C\dot{\omega}(t) + \ddot{\omega}_r(t) + D\dot{\omega}(t) + E\omega(t) + K\,\text{sign}(s(t))\right] \tag{3.20}$$

$$u(t) = \frac{1}{A}\left[(D-C)\dot{\omega}(t) + E\omega(t) + C\dot{\omega}_r(t) + \ddot{\omega}_r(t) + K\,\text{sign}(s(t))\right] \tag{3.21}$$

In order to reduce chattering in SMC, the control signal is modified using a smooth sigmoid function. The resulting control signal is given in equation (3.22).

$$u(t) = \frac{1}{A}\left[(D-C)\dot{\omega}(t) + E\omega(t) + C\dot{\omega}_r(t) + \ddot{\omega}_r(t) + K\left(\frac{s}{|s|+\delta}\right)\right]$$
$$0 < \delta < 1 \tag{3.22}$$

The parameters K, C, and δ in equation (3.22) are values that need to be determined. The block diagram of the designed system is shown in Figure 3.2.
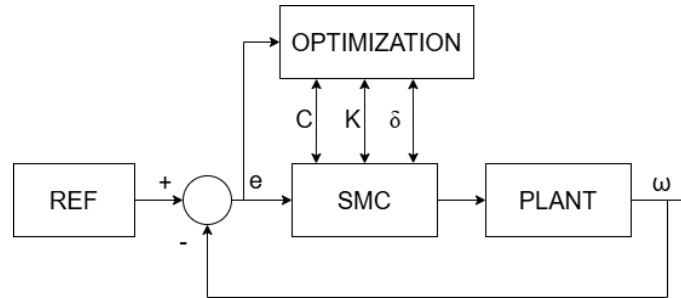

Figure 3.2: Block diagram of the designed system

4. Results

In this section, simulation results are presented to demonstrate the performance of the optimized controllers. Table 4.1 presents the parameters used in optimization methods compared in the study.

Method	Parameters
	Number of iterations: 50
$C_{d-v}HGSO$	Number of gas particles: 50
C_rHGSO	Number of clusters: 5
C_sHGSO	M1 = 0.1, M2 = 0.2
$HGSO$(2019)	L1 = 0.005, L2 = 100, L3 = 0.01
[28]	
	a, b, k = 1
	e = 0.05
$C_{d-v}PSO$	Number of iterations: 50
C_rPSO	Number of swarm: 50
C_sPSO	C1 = 2.1(Individual learning coefficient)
PSO(1998) [32]	C2 = 2.1(Social learning coefficient)
$C_{d-v}WOA$	
C_rWOA	Number of iterations: 50
C_sWOA	Number of whales: 50
WOA(2016)	
[33]	
$C_{d-v}sA$	Number of iterations: 50
C_rSA	Number of materials: 50
C_SSA	Cooling rate: 0.98
SA(1987) [34]	
$C_{d-v}EA$	Number of iterations: 50
C_rEA	Number of parents: 20
C_sEA	Number of children: 4
EA(2002) [35]	

Table 4.1: Algorithm parameters

The parameters K, C, and δ of the sliding mode controller, as specified in equation (3.22), have been optimized using the HGSO [28], PSO [32], WOA [33], SA [34], EA [35], algorithms and chaotic variants. The parameters adjusted by these algorithms are presented in Table 4.2.

Method	C	K	δ	Fitness
$C_{d-v}HGSO$	398.062587	209874.34347	0.329845	0.000384
C_sHGSO	362.340149	208738.325916	0.306580	0.000385
$C_{d-v}WOA$	334.291252	209715.546287	0.273285	0.000386
C_rHGSO	375.658937	208968.3768195	0.286351	0.000387
C_rWOA	350.691352	209380.016280	0.268539	0.000388
$HGSO$	350.595683	209657.567603	0.192955	0.000390
C_sWOA	310.583040	208472.372945	0.237463	0.000391
WOA	278.291252	208010.546287	0.207646	0.000392
SA	219.907082	209039.747574	0.18824	0.000398
C_rSA	256.357642	201728.395761	0.452480	0.000420
$C_{d-v}EA$	282.926727	196335.511718	0.121435	0.000448
C_sEA	320.415718	194239.978390	0.148088	0.000450
C_rEA	294.671428	197376.736512	0.153561	0.000463
C_sSA	307.340209	195382.379581	0.728305	0.000471
EA	367.261204	193033.390611	0.113622	0.000474
$C_{d-v}SA$	374.13673	196431.024497	0.926444	0.000501
PSO	340.435828	206990.671095	0.141625	0.000557
C_rPSO	370.617110	180237.177519	0.356741	0.000642
C_sPSO	385.144228	175253.264785	0.654917	0.000674
$C_{d-v}PSO$	387.398806	177413.126137	0.75771	0.000693

Table 4.2: The parameters of the SMC optimized by the algorithms for the DC motor

The parameters of the SMC optimized according to the error-based ITSE objective function are presented in Table 4.2. It is observed that the best objective function result is provided by the $C_{d-v}HGSO$ algorithm. Additionally, when the HGSO, WOA, and EA algorithms are hybridized with the chaotic equation, a convergence toward the minimum of the objective function is observed.
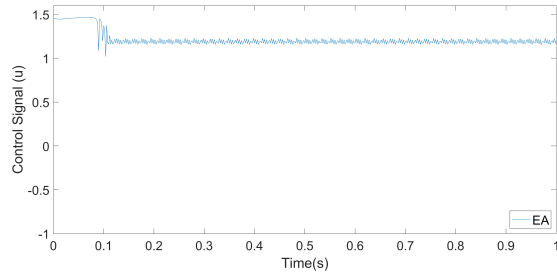
(a) The EA algorithm
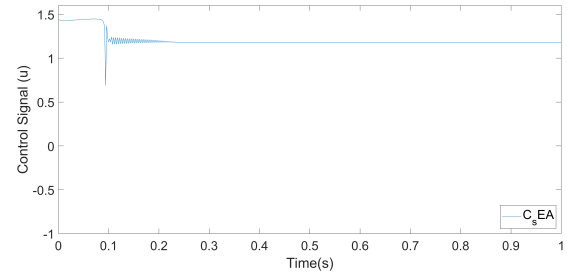
(b) The C_rEA algorithm
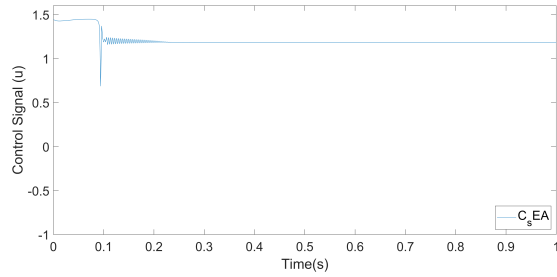
(c) The C_sEA algorithm
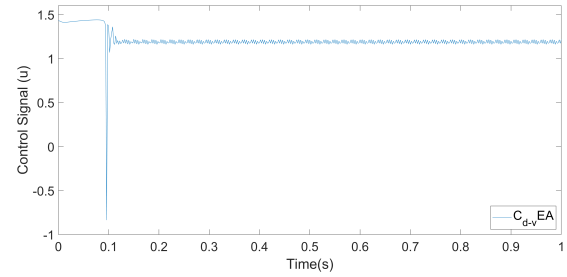
(d) The $C_{d-v}EA$ algorithm
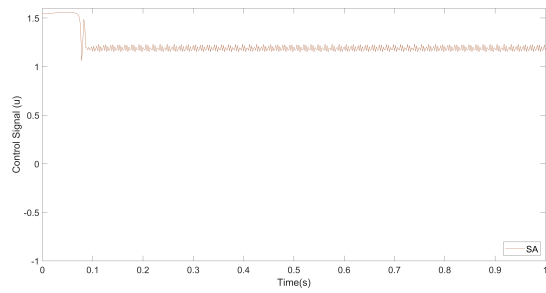
(e) The SA algorithm
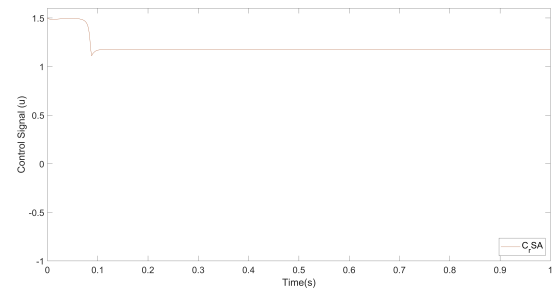
(f) The C_rSA algorithm
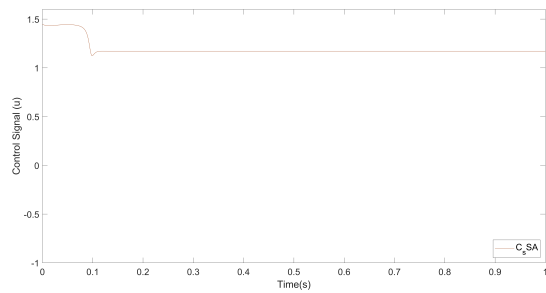
(g) The C_sSA algorithm
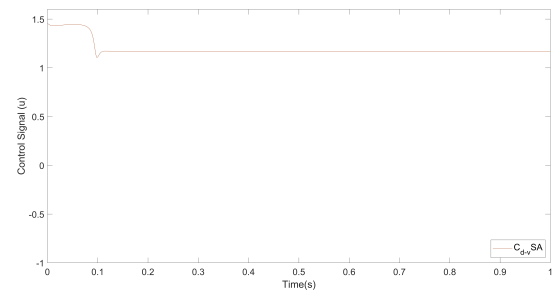
(h) The $C_{d-v}SA$ algorithm
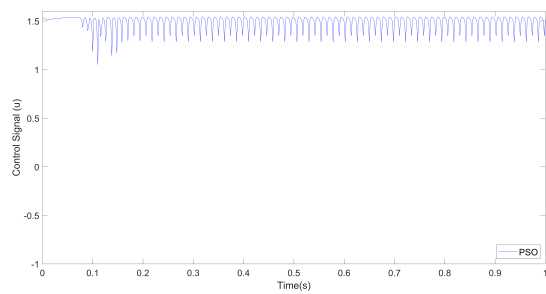
(i) The PSO algorithm
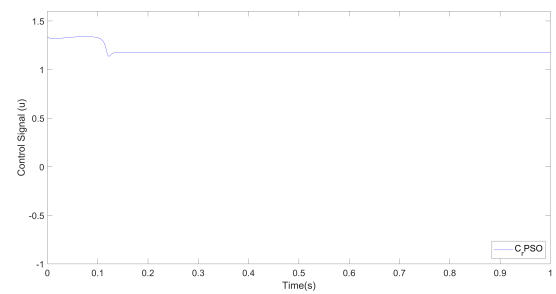
(j) The C_rPSO algorithm

Figure 4.1: The control signals generated by the algorithms for DC motor (Part 1)
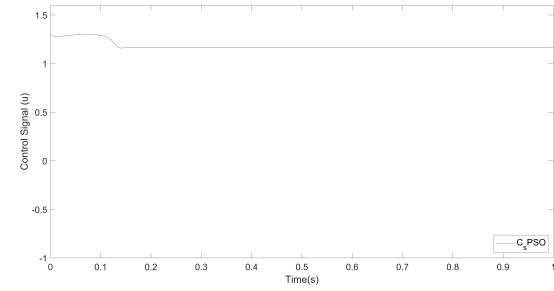
(k) The C_sPSO algorithm
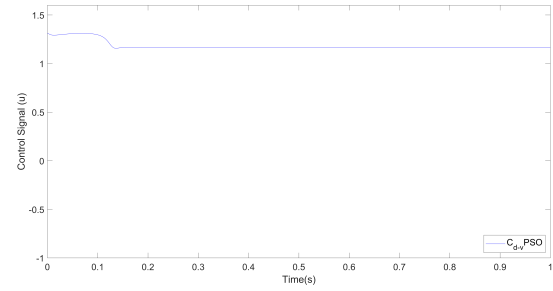
(l) The $C_{d-v}PSO$ algorithm
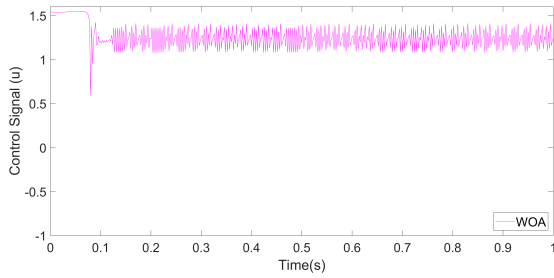
(m) The WOA algorithm
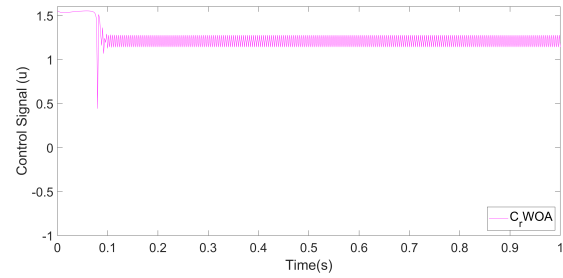
(n) The C_rWOA algorithm
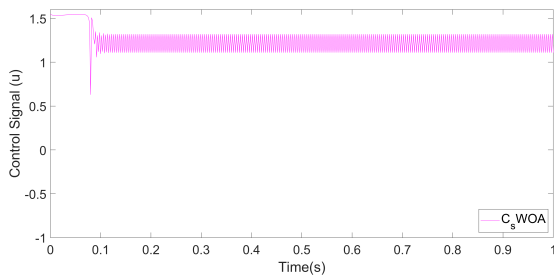
(o) The C_sWOA algorithm
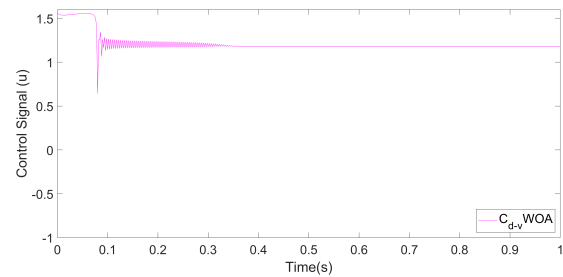
(p) The $C_{d-v}WOA$ algorithm
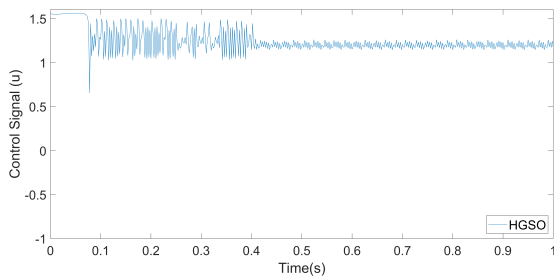
(q) The HGSO algorithms
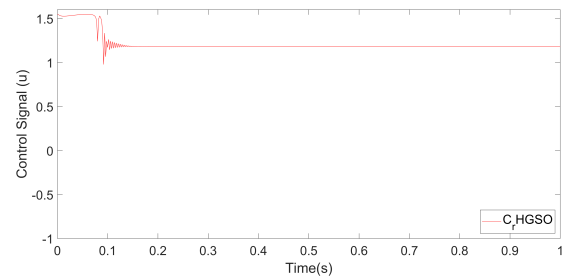
(r) The C_rHGSO algorithm
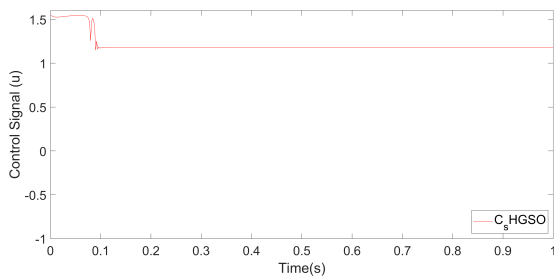
(s) The $C-sHGSO$ algorithm
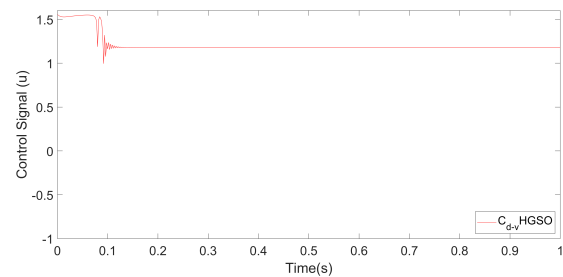
(t) The $C_{d-v}HGSO$ algorithm

Figure 4.1: The control signals generated by the algorithms for DC motor (Part 2)

Figure 4.1 presents the control signals generated by the optimized SMC for the DC motor. It can be observed that the chattering is reduced in the optimization methods hybridized with chaotic equations. As the parameter δ in the smooth sigmoid function approaches one, the reduction

in chattering is expected. When reviewing Table 4.2, it is evident that the δ values in the hybrid algorithms are closer to 1 compared to the original algorithms. For this reason, it has been observed that hybrid algorithms are more effective in optimizing δ.

(a) The responses of the EA algorithms

(b) Zoomed-in view of (a)

(c) The responses of the SA algorithms

(d) Zoomed-in view of (c)

(e) The responses of the PSO algorithms

(f) Zoomed-in view of (e)

(g) The responses of the WOA algorithms

(h) Zoomed-in view of (g)

(i) The responses of the HGSO algorithms

(j) Zoomed-in view of (i)

Figure 4.2: The step response of the optimized SMC for the DC motor.

Figure 4.2, the speed responses of the DC motor controlled by the sliding mode controller to a unit step reference signal are presented. In Figure 4.2d, it is observed that, except for the SA algorithm, the other algorithms demonstrate lower tracking errors when hybridized with chaotic systems. An analysis of the control signals reveals that the EA and chaotic EA algorithms exhibit similar responses, and no significant reduction in chattering is observed in $C_{d-v}EA$ after hybridization. However, a noticeable decrease in chattering is observed in the Rössler and Sprott-A systems. Although the rise time (Tr) and settling time (Ts) exhibit some degradation in the chaotic PSO algorithm compared to the PSO, a notable reduction in chattering is achieved, indicating improved control smoothness. For the SA and chaotic SA algorithms, although a slight improvement in chattering is noted after hybridization, there are deteriorations in rise time, settling time, and steady-state error.In the evaluation of the WOA and chaotic WOA algorithms, it is noted that the chaotic WOA algorithms do not exhibit any change in settling time and rise time. However, a significant improvement is observed in chattering and steady-state error. The analysis of the results produced by the HGSO and chaotic HGSO algorithms reveals that hybridizing the HGSO algorithm with chaotic systems leads to a reduction in steady-state error and an improvement in settling time. Additionally, while the rise time improves in $C_{d-v}HGSO$, it remains unchanged in the other variants. An examination of the control signals indicates a significant reduction in chattering, where a notable improvement in chattering is observed within the first 0.45 seconds, during which the system remains within the settling band in the speed response.

Based on Figure 4.2, a detailed analysis of the effects of the algorithms on performance metrics is presented in Table 4.3 by examining the responses of the DC motor to the unit step reference signal.

Algorithm	Tr	Ts(%1)	Steady-State Error
$C_{d-v}HGSO$	0.068	0.084	0.0022
$C_r HGSO$	0.070	0.088	0.0023
$C_s HGSO$	0.070	0.086	0.0024
$HGSO$	0.070	0.090	0.0025
$C_{d-v}WOA$	0.070	0.088	0.0024
$C_r WOA$	0.072	0.090	0.0026
$C_s WOA$	0.072	0.090	0.0028
WOA	0.072	0.090	0.0030
$C_{d-v}EA$	0.082	0.096	0.0014
$C_r EA$	0.082	0.098	0.0014
$C_s EA$	0.080	0.094	0.0020
EA	0.078	0.102	0.0018
$C_{d-v}SA$	0.080	0.100	0.0094
$C_r SA$	0.080	0.102	0.0092
$C_s SA$	0.076	0.094	0.0058
SA	0.070	0.090	0.0026
$C_{d-v}PSO$	0.096	-	0.0140
$C_r PSO$	0.098	-	0.0130
$C_s PSO$	0.094	0.124	0.052
PSO	0.074	-	0.0175

Table 4.3: Comparison of the Step Response of the SMC for the DC motor

When examining the results presented in Table 4.3, the Friedman test was conducted to determine whether at least one of the methods could be considered statistically acceptable. In accordance with common practice in the literature, the significance level was set at $a = 0.05$ [36]. When this test was applied to Table 4.3, the obtained p-value was 0.002727. Since $p < a$, H_0 hypothesis (stating that the methods have similar effects) was rejected, and the alternative hypothesis (H_1, stating that there is a statistically significant difference among the methods) was accepted.

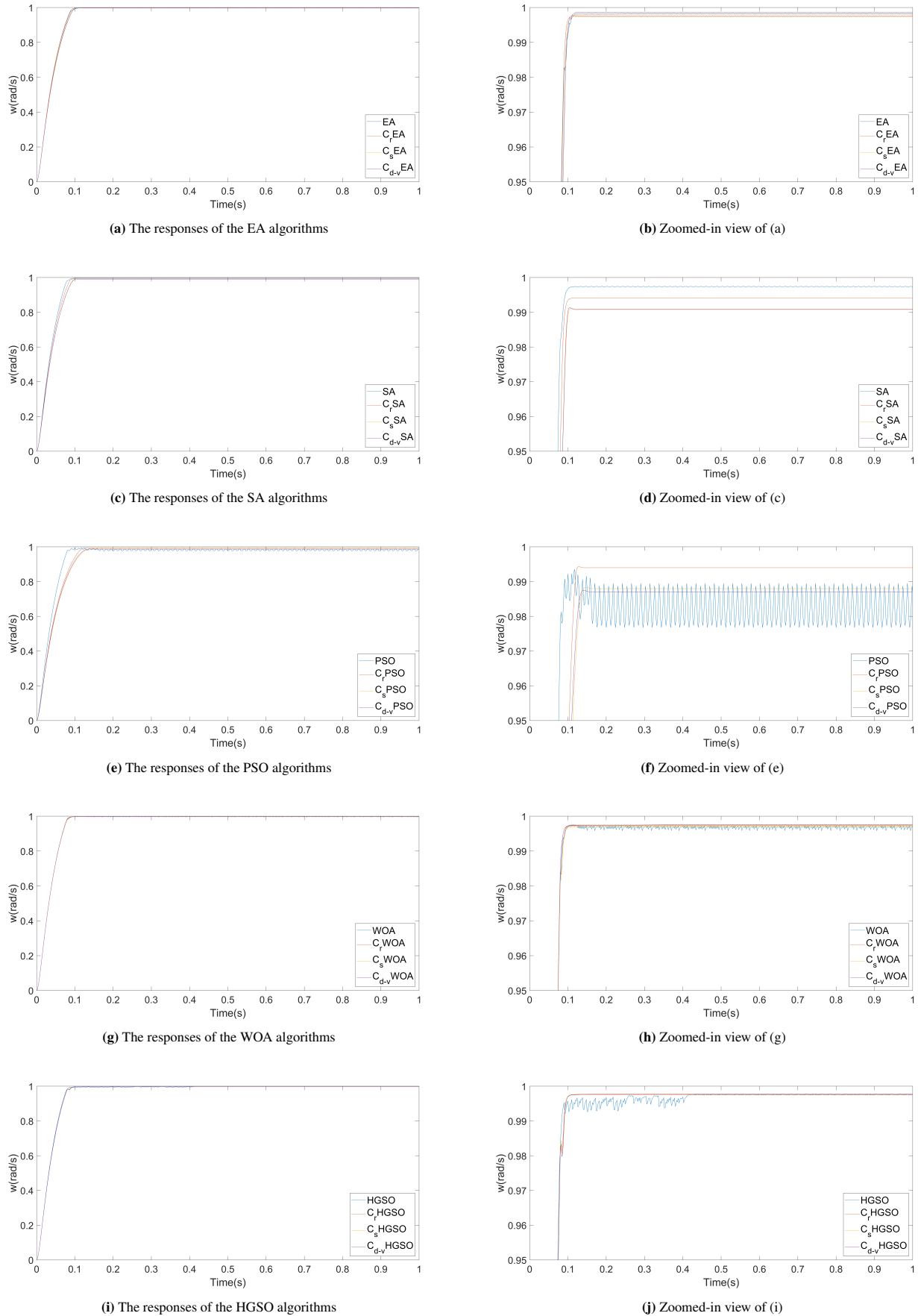Optimization algorithms were applied to a different DC motor whose parameters are provided in Table 4.4, and the performance was evaluated based on rise time, settling time, and steady-state error criteria, as well as through the Friedman statistical test. Among the compared methods, the CHGSO algorithm yielded the best overall performance across all evaluation metrics.

Parameter	DC motor2
$R_a(\Omega)$	0.6
$L_a(H)$	0.012
B	0.0167
$J(kgm^2/s^2)$	0.0167
$K_b(Vs/rad)$	0.8
$K_t(Nm/A)$ 2	0.8

Table 4.4: The parameters of the DC motors2

5. Conclusion

The results of this study demonstrate that hybridizing the HGSO, WOA, EA, and PSO algorithms with chaotic equations significantly enhances control performance. The use of hybrid algorithms generally exhibits a tendency to decrease Steady-State Error. A lower steady-state error means that the system remains in a position closer to the reference value in the long term, and this is an indicator of an improvement in control performance. In addition, it has been observed that the SMC does not show any overshoot. While a significant

improvement was achieved in the settling time (Ts) HGSO and EA algorithms for the 1% error band, it was found that the rise time (Tr) remained constant in the HGSO and WOA algorithms. These findings offer an important advantage, especially in control applications that require high precision.

In addition, chattering caused by high frequency switching in physical systems can negatively affect the life of systems. Chattering prevention is of critical importance in terms of preventing damage to system components. The findings obtained in this study reveal that the SMC with chaotic-based optimized parameters not only provides low settling time, rise time, and steady state error, but also offers an effective performance in terms of chattering prevention.

In this context, the application of optimization algorithms in the parameter setting process of control methods reduces time and labor costs by minimizing human intervention. According to the Friedman test, at least one of the applied methods exhibits a statistically significant difference. The results of the study show that their performance can be improved by hybridizing optimization methods with chaotic systems. SMC optimized by the Chaotic Henry Gas Solubility Optimization algorithm has provided optimal stability for the system by exhibiting the best performance compared to HGSO, chaotic WOA, WOA, chaotic EA, EA, chaotic SA, SA, chaotic PSO, and PSO. When comparing the chaotic systems among themselves, it is observed that optimizing the SMC with the Duffing–Van der Pol chaotic system yields better controller responses compared to the Rössler and Sprott-A systems. These obtained results show that optimization methods integrated with chaotic systems offer significant advantages in controller design and can provide valuable contributions to future studies in this field.

Article Information

Author's contributions: All authors read and approved the final manuscript. **M.S.S.**: Research design and implementation, literature review, data analysis, and manuscript writing. **O.D.**: Literature review, manuscript revision, and editing. **S.K.**: Editing and supervision. **A.D.**: Editing and supervision.

Artificial Intelligence Statement: No AI tools or technologies were used in the preparation of this manuscript. All content was created solely by the authors.

Conflict of Interest Disclosure: No potential conflict of interest was declared by the authors.

Plagiarism Statement: This article was scanned by the plagiarism program.

References

[1] W. Cao, X. Liu, J. Ni, *Parameter optimization of support vector regression using Henry gas solubility optimization algorithm*, IEEE Access, **8** (2020), 88633-88642. https://doi.org/10.1109/ACCESS.2020.2993267

[2] M. Liu, T. Liu, M. Zhu, et al., *A PI control method with HGSO parameter regulator for trajectory planning of 9-DOF redundant manipulator*, Sensors, **22**(18) (2022), Article ID 6860. https://doi.org/10.3390/s22186860

[3] H. Abdel-Mawgoud, S. Kamel, M. Khasanov, et al., *A strategy for PV and BESS allocation considering uncertainty based on a modified Henry gas solubility optimizer*, Electr. Power. Syst. Res., **191** (2021), Article ID 106886. https://doi.org/10.1016/j.epsr.2020.106886

[4] D.T. Mosa, A. Mahmoud, J. Zaki, et al., *Henry gas solubility optimization double machine learning classifier for neurosurgical patients*, PLoS One, **18**(5) (2023), Article ID e0285455. https://doi.org/10.1371/journal.pone.0285455

[5] W. Xie, C. Xing, J. Wang, et al., *Hybrid henry gas solubility optimization algorithm based on the harris hawk optimization*, IEEE Access, **8** (2020), 144665-144692. https://doi.org/10.1109/ACCESS.2020.3014309

[6] M. Abd Elaziz, D. Yousri, *Automatic selection of heavy-tailed distributions-based synergy Henry gas solubility and Harris hawk optimizer for feature selection: Case study drug design and discovery*, Artif. Intell. Rev., **54**(6) (2021), 4685-4730. https://doi.org/10.1007/s10462-021-10009-z

[7] S. Ekinci, B. Hekimoğlu, D. Izci, *Opposition based Henry gas solubility optimization as a novel algorithm for PID control of DC motor*, Eng. Sci. Technol., Int. J., **24**(2) (2021), 331-342. https://doi.org/10.1016/j.jestch.2020.08.011

[8] S. Ravikumar, D. Kavitha, *CNN-OHGS: CNN-oppositional-based Henry gas solubility optimization model for autonomous vehicle control system*, J. Field Robot., **38**(7) (2021), 967-979. https://doi.org/10.1002/rob.22020

[9] B.M. Alshammari, A. Farah, K. Alqunun, et al., *Robust design of dual-input power system stabilizer using chaotic Jaya algorithm*, Energies, **14**(17) (2021), Article ID 5294. https://doi.org/10.3390/en14175294

[10] E. Emary, H.M. Zawbaa, *Impact of chaos functions on modern swarm optimizers*, PLoS One, **11**(7) (2016), Article ID e0158738. https://doi.org/10.1371/journal.pone.0158738

[11] D. Yan, Y. Lu, M. Zhou, et al., *Empirically characteristic analysis of chaotic PID controlling particle swarm optimization*, PLoS One, **12**(5) (2017), Article ID e0176359. https://doi.org/10.1371/journal.pone.0176359

[12] D. Tian, *Particle swarm optimization with chaotic maps and Gaussian mutation for function optimization*, Int. J. Grid Distrib. Comput., **8**(4) (2015), 123-134. http://dx.doi.org/10.14257/ijgdc.2015.8.4.12

[13] M.L. Huang, *Hybridization of chaotic quantum particle swarm optimization with SVR in electric demand forecasting*, Energies, **9**(6) (2016), Article ID 426. https://doi.org/10.3390/en9060426

[14] Y. Du, F. Xu, *A hybrid multi-step probability selection particle swarm optimization with dynamic chaotic inertial weight and acceleration coefficients for numerical function optimization*, Symmetry, **12**(6) (2020), Article ID 922. https://doi.org/10.3390/sym12060922

[15] I.A. Hodashinsky, M.B. Bardamova, *Tuning fuzzy systems parameters with chaotic particle swarm optimization*, J. Phys. Conf. Ser., **803** (2017), Article ID 012053. https://doi.org/10.1088/1742-6596/803/1/012053

[16] P. Qu, F. Du, *Improved particle swarm optimization for laser cutting path planning*, IEEE Access, **11** (2023), 4574-4588. https://doi.org/10.1109/ACCESS.2023.3236006

[17] C. Yanguang, M. Zhang, C. Hao, *A hybrid chaotic quantum evolutionary algorithm*, In 2010 IEEE International Conference on Intelligent Computing and Intelligent Systems (ICIS), (2010), pp. 771–776. https://doi.org/10.1109/ICICISYS.2010.5658622

[18] M. Verma, M. Sreejeth, M. Singh, et al., *Chaotic mapping based advanced Aquila Optimizer with single stage evolutionary algorithm*, IEEE Access, **10** (2022), 89153-89169. https://doi.org/10.1109/ACCESS.2022.3200386

[19] H. Lu, L. Yin, X. Wang, et al., *Chaotic multiobjective evolutionary algorithm based on decomposition for test task scheduling problem*, Math. Probl. Eng., **2014**(1) (2014), Article ID 640764. https://doi.org/10.1155/2014/640764

[20] H. Lu, X. Wang, Z. Fei, et al., *The effects of using chaotic map on improving the performance of multiobjective evolutionary algorithms*, Math. Probl. Eng., **2014**(1) (2014), Article ID 924652. https://doi.org/10.1155/2014/924652

[21] L. Wang, S. Li, F. Tian, et al., *A noisy chaotic neural network for solving combinatorial optimization problems: Stochastic chaotic simulated annealing*, IEEE Trans. Syst. Man Cybern. Part B: Cybern., **34**(5) (2004), 2119-2125. https://doi.org/10.1109/TSMCB.2004.829778

[22] Y. Jiang, Y. Lei, Z. Zhong, et al., *A wavelet chaotic simulated annealing neural network and its application to optimization problems*, In 2011 International Conference on Network Computing and Information Security (NCIS), (2011), 347-351. https://doi.org/10.1109/NCIS.2011.166

[23] K. Ferens, D. Cook, W. Kinsner, *Chaotic simulated annealing for task allocation in a multiprocessing system*, In 12th IEEE International Conference on Cognitive Informatics and Cognitive Computing (ICCI*CC), (2013), 26-35. https://doi.org/10.1109/ICCI-CC.2013.6622222

[24] J. Li, L. Guo, Y. Li, et al., *Enhancing whale optimization algorithm with chaotic theory for permutation flow shop scheduling problem*, Int. J. Comput. Intell. Syst., **14**(1) (2021), 651–675. https://doi.org/10.2991/ijcis.d.210112.002

[25] H. Ding, Z. Wu, L. Zhao, *Whale optimization algorithm based on nonlinear convergence factor and chaotic inertial weight*, Concurr. Comput.: Pract. Exper., **32**(24) (2020), Article ID e5949. https://doi.org/10.1002/cpe.5949

[26] Y. Mousavi, A. Alfi, I.B. Kucukdemiral, *Enhanced fractional chaotic whale optimization algorithm for parameter identification of isolated wind-diesel power systems*, IEEE Access, **8** (2020), 140862-140875. https://doi.org/10.1109/ACCESS.2020.3012686

[27] M.S. Sarıkaya, Y. H. El Naser, S. Kaçar, et al., *Chaotic-Based Improved Henry Gas Solubility Optimization Algorithm: Application to Electric Motor Control*, Symmetry, **16**(11) (2024), Article ID 1435. https://doi.org/10.3390/sym16111435

[28] F.A. Hashim, E.H. Houssein, M.S. Mabrouk, et al., *Henry gas solubility optimization: A novel physics-based algorithm*, Future Gener. Comput Syst., **101** (2019), 646-667. https://doi.org/10.1016/j.future.2019.07.015

[29] Y. Hamida El Naser, D. Karayel, *Modeling the effects of external oscillations on mucus clearance in obstructed airways*, Biomech. Model. Mechanobiol. **23**(1), (2024), 335-348. https://doi.org/10.1007/s10237-023-01778-3

[30] M. Rafikov, J.M. Balthazar, *On an optimal control design for Rössler system*, Phys. Lett. A, **333**(3-4), (2004), 241-245. https://doi.org/10.1016/j.physleta.2004.10.032

[31] J.Y. Hung, W. Gao, J.C. Hung, *Variable structure control: A survey*, IEEE Trans. Ind. Electron., **40**(1) (1993), 2-22. https://doi.org/10.1109/41.184817

[32] Y. Shi, R.C. Eberhart, *A modified particle swarm optimizer*, In Proceedings of the IEEE International Conference on Evolutionary Computation, (1998), 69–73. https://doi.org/10.1109/ICEC.1998.699146

[33] S. Mirjalili, A. Lewis, *The whale optimization algorithm*, Adv. Eng. Softw., **95** (2016), 51–67. https://doi.org/10.1016/j.advengsoft.2016.01.008

[34] P.J. Van Laarhoven, E.H. Aarts, *Simulated Annealing*, Springer, Berlin, 1987. https://doi.org/10.1007/978-94-015-7744-1_2

[35] H.G. Beyer, H.P. Schwefel, *Evolution strategies–a comprehensive introduction*, Nat. Comput., **1** (2002), 3–52. https://doi.org/10.1023/A:1015059928466

[36] L. Xie, T. Han, H. Zhou, et al., *Tuna swarm optimization: A novel swarm-based metaheuristic algorithm for global optimization*, Comput. Intell. Neurosci., **2021**(1) (2021), Article ID 9210050. https://doi.org/10.1155/2021/9210050

Research Article

Mathematical Model of COVID-19 with Imperfect Vaccine and Virus Mutation

Ceren Gürbüz Can[1]* ⊚ **and Sebaheddin Şevgin**[1] ⊚

[1]*Department of Mathematics, Faculty of Science, Van Yuzuncu Yil University, Van, Türkiye* ᴿᴼᴿ
*Corresponding author

Abstract

In this study, we investigated the effect of a partially protective vaccine on COVID-19 infection with the original and mutant viruses using a deterministic mathematical model. The model we developed consists of S (susceptible), V (vaccinated), I_1 (infected with the original virus), I_2 (infected with the mutant virus), and R (recovered) subcompartments. In the model, we examined the effect of both artificial active immunity (vaccinated) and natural active immunity (infected). Since it is known that the recovery and mortality rates of the original virus and the mutant virus are different in COVID-19, we took this into account in the study. First of all, we obtained the basic reproduction number using the next-generation matrix method. We analyzed the local stability of the disease-free equilibrium point and the endemic equilibrium point of the model using the Routh-Hurwitz criterion and the global stability with the help of Lyapunov functions. Using the Castillo-Chavez and Song Bifurcation Theorem, we demonstrate the existence of a backward bifurcation that occurs when the vaccine is not effective enough, leading to the simultaneous existence of both disease-free and endemic equilibrium points, even when the basic reproduction number is below 1. We estimated the three model parameters by parameter estimation and identified the model-sensitive parameters by local sensitivity analysis. We found that the parameter representing vaccine efficacy is the most sensitive to the basic reproduction number, and that increasing vaccine efficacy will reduce the average number of secondary cases. The three different simulations we present to illustrate the basic mechanisms underlying the dynamics of our model and to support the analytical findings suggest that there is a strong relationship between vaccine efficacy and the course of the epidemic, and that it is necessary to produce vaccines with higher efficacy and increase the vaccination rate to reduce the average number of secondary cases and the likelihood that infected individuals will remain under the influence of the epidemic for a long time.

1. Introduction

Infectious diseases have had increased opportunities to spread more rapidly and easily due to changing social living conditions. Cholera, dengue fever, Ebola, and the COVID-19 pandemic, which we are currently combating, are among the most significant outbreaks identified to date. In addition to their deadly consequences, infectious diseases have had severe demographic, economic, and social impacts on a global scale. In particular, COVID-19 has served as a striking example of how profoundly infectious diseases can affect human life, impacting the entire world.

Mathematical epidemiology, which scientifically examines the mathematical modeling of infectious diseases, primarily focuses on viral and bacterial diseases. These infectious diseases have been modeled using differential equation systems with the help of various subdivisions since 1927. In these models, the total population is categorized based on exposure to the pathogen, treatment, or immunity status. Accordingly, the population is divided into sub-compartments such as susceptible, vaccinated, infected, and recovered individuals.

Theoretical papers on disease models within the scope of epidemiology have become important tools for analyzing the spread and control of diseases. Furthermore, mathematical models are intended to assist in the comparison, planning, implementation, evaluation, and optimization of various detection, prevention, treatment, and control programs. Mathematical models used to analyze the dynamics of infectious diseases are categorized as either statistical or dynamic models in the literature. Dynamic models investigate how disease processes evolve over time. Deterministic, stochastic, network, and agent-based models are among them.

Deterministic models—one of which is the focus of our study—are sometimes referred to as compartmental models because they are constructed by partitioning the entire population into smaller groups. These models do not account for the impact of unpredictability in disease dynamics. They use differential equations for continuous-time modeling and difference equations for discrete-time modeling and are suitable for simulating large populations [1].

The impact of vaccination was the focus of one of the first mathematical models in epidemiology. W.O. Kermack and A.G. McKendrick made substantial contributions to epidemic theory by publishing three fundamental studies in 1927, 1932, and 1933 that laid the foundation for compartmental models explaining infectious disease transmission [2].

T.D. Frank analyzed the dynamics of COVID-19 infections from the perspective of bifurcation theory by modeling the R (recovered) class in the basic SEIR compartmental model as five separate subpopulations [3]. A death (D) subpopulation was incorporated into the basic SEIR model in [4], where analytical solutions were explored. The SIQ compartmental model was used in [5] to calculate possible equilibrium points and perform stability analysis via Lyapunov theory. In [6], A.E. Matouk examined the effects of two therapeutic drugs on the SIMDR model, identifying eight equilibrium points and conducting a stability analysis.

Gumel et al. modeled the I (infectious) class of the basic SEIR model as three distinct subpopulations and analyzed their equilibrium points and stability [1].

Pandemic dynamics were analyzed in [7] by comparing early COVID-19 data from Italy with later data from Turkey using a five-compartment model. In [8], the COVID-19 pandemic in Turkey was modeled using a five-compartment approach, with both local and global stability analyses conducted.

Various mathematical approaches have been developed to model the spread of COVID-19. In [9], Boulaaras et al. analyzed the stability of equilibrium points and the impact of the basic reproduction number using a classical SEIR model. Xu et al. proposed a fractional-order model for the Omicron variant and examined its stability via the Lyapunov method in [10]. Jamil et al. developed an age-structured fractal–fractional model to assess the impact of vaccination across different age groups [11].

The epidemiological dynamics of COVID-19 have become increasingly complex due to the emergence of new viral variants. To capture these dynamics, multi-strain mathematical models incorporate factors such as the relative infectiousness of variants, differential vaccine responsiveness, and inter-strain competition. In [12], Avila-Ponce de León *et al.* formulated a two-strain model focusing on the Alpha and Delta variants in the United States and demonstrated that insufficient vaccination may facilitate enhanced transmission in multi-strain contexts. Bugalia *et al.*, using data from India, investigated the role of imperfect vaccination on mutant strains and reported a loss of system stability at intermediate mutation rates in [13]. Notably, they identified a stable configuration termed the "endemic bubble" at higher mutation rates. These findings highlight that both vaccine efficacy and its ability to induce cross-strain immunity are pivotal in shaping disease trajectories. In a three-strain SEIR framework, Yaagoub and Allali showed that the basic reproduction number R_0 must be less than one for each strain to ensure disease eradication in [14]. Kim *et al.* explored optimal control strategies-vaccination, social distancing, and test-treatment based on Ghanaian data, concluding through numerical simulations that integrated interventions are more effective than standalone approaches [15]. Finally, Chen *et al.* developed an SVEIR model calibrated to Chinese data on Omicron and XBB variants, revealing that "protection awareness", modulated by the dominant strain's R_0, significantly reduces transmission potential in [16]. Collectively, these studies underscore that viral mutation, strain competition, vaccine characteristics, and public behavioral response are critical determinants of epidemic dynamics.

In the mathematical epidemiology literature, the backward bifurcation phenomenon poses significant challenges in terms of disease control. This phenomenon leads to the simultaneous existence of both disease-free and endemic equilibrium points even when the basic reproduction number is below 1, and therefore, the basic reproduction number condition being less than 1 is not sufficient for disease eradication. In [17], Gumel theoretically demonstrated that backward bifurcation can occur in classical transmission models through mechanisms such as imperfect vaccine, re-infection, different immunity periods, and risk groups. This approach was later adapted to COVID-19 models. In [18], Rwat et al. showed in their model that low vaccine efficacy can cause not only backward bifurcation but also hysteresis, making epidemic control more complicated. Numerical analyses of the model calibrated with COVID-19 transmission parameters in Malaysia revealed that even if the basic reproduction number is less than 1, a low-efficacy vaccine may be insufficient to suppress the epidemic. In [19], Omede et al. reported that backward bifurcation can also be observed in multi-strain structures in their models that take into account the competition and reinfection processes of Delta and Omicron variants, and that this situation is exacerbated by transitions between variants. Finally, Fatahillah and Aldila demonstrated that backward bifurcation exists in the imperfect vaccine model, which includes saturation effects in transmission and recovery processes, both analytically and numerically, and that this situation may limit the success of vaccine strategies in [20]. All these studies clearly demonstrate that vaccine efficacy plays a key role in epidemic control, but the epidemiological equilibrium structures become much more complex in the case of imperfect vaccines.

In this study, a deterministic compartmental model was developed to investigate the impact of both the original and mutant strains of the COVID-19 virus, as well as the role of partially protective vaccination, on the potential eradication of the pandemic. The model introduces vaccinated individuals as a distinct compartment and explicitly addresses the issue of imperfect (leaky) vaccines, where vaccine-induced immunity is incomplete, allowing vaccinated individuals to become infected, albeit with reduced probability compared to those unvaccinated. To capture heterogeneity in population response, the model includes parameters representing subgroups with differing disease-related behaviors or characteristics. Biological interpretations of all model parameters are presented in Table 2.1.

The novelty of this study lies in its investigation of the combined effects of vaccine imperfection and viral mutation on the spread of the COVID-19 pandemic, utilizing data specific to Turkey.

The main contributions of this study are as follows:

(i) Recognizing that a single mathematical model cannot fully capture a real-world event or phenomenon, we developed a new model by introducing additional parameters (mutation, leaky vaccine) and new subpopulations (individuals infected with the mutant strain), thereby differentiating our work from the existing literature.

(ii) By defining subpopulations infected with the original and mutant virus strains—extending beyond the compartments used in traditional infectious disease models—we accounted for the impact of disease progression on these distinct groups.

(iii) Through numerical simulations, we forecasted how interventions such as vaccination might influence the trajectory of the pandemic and contribute to its control.

The structure of this paper is organized as follows. In Section 2, we present the development of a mathematical model describing the transmission dynamics of COVID-19. We determine both the disease-free and endemic equilibrium points and calculate the basic reproduction number. Section 3 focuses on the local stability analysis of these equilibria. Section 4 addresses global stability using a Lyapunov function. In Section 5, we conduct a backward bifurcation analysis based on the Castillo-Chavez and Song theorem. Section 6 details the parameter estimation process, followed by sensitivity analysis in Section 7. Section 8 presents various numerical simulations, and Section 9 discusses the findings.

2. Mathematical Model

In this study, we develop a deterministic compartmental model to investigate the dynamics of COVID-19 transmission. Assuming a total population size of N, the model comprises the following compartments: S (Susceptible), V (Vaccinated), I_1 (Infected with the original strain), I_2 (Infected with the mutant strain), and R (Recovered). The nonlinear system of ordinary differential equations formulated to describe the progression of the infection is presented below, along with detailed definitions of the model parameters.

$$
\begin{aligned}
\frac{dS}{dt} &= B - \omega S - \beta_1 SI_1 - \beta_2 SI_2 - \alpha S + \mu V + \delta R \\
\frac{dV}{dt} &= -\omega V - (1-\sigma)\beta_1 VI_1 - (1-\sigma)\beta_2 VI_2 + \alpha S - \mu V \\
\frac{dI_1}{dt} &= -\omega I_1 - \omega_1 I_1 - mI_1 - r_1 I_1 + \beta_1 SI_1 + (1-\sigma)\beta_1 VI_1 \\
\frac{dI_2}{dt} &= -\omega I_2 - \omega_2 I_2 + mI_1 - r_2 I_2 + \beta_2 SI_2 + (1-\sigma)\beta_2 VI_2 \\
\frac{dR}{dt} &= -\omega R + r_1 I_1 + r_2 I_2 - \delta R
\end{aligned}
\tag{2.1}
$$

In the model, represented by the flow diagram in Figure 2.1, the susceptible population (S) increases with birth, loss of vaccine-induced immunity, and loss of natural immunity acquired through infection. This population declines through vaccination (transition to the V class), infection, and natural death. The vaccinated population (V) increases by vaccinating susceptible individuals. Since the defective vaccine was present in the model, we took into account that vaccinated people could also become infected. Thus, the vaccinated population decreases due to infection, decrease of artificial active immunity, and natural death. The infected population declines with natural death and the population recovering from the disease. The recovered population increases as individuals recover from infection and decreases as immunity acquired by infection declines.

Parameter	Description
B	Natural birth rate
ω	Natural death rate
β_1	Transmission rate of the original virus
β_2	Transmission rate of the mutant virus
α	Vaccination rate of susceptible individuals
μ	Rate of decline in vaccine-induced immunity
δ	Rate of decline in immunity gained through infection
σ	Vaccine efficacy
ω_1	Additional mortality rate caused by the original virus
ω_2	Additional mortality rate caused by the mutant virus
m	Mutation rate
r_1	Recovery rate for the original virus
r_2	Recovery rate for the mutant virus

Table 2.1: Biological interpretations of the parameters

The initial conditions for the model are taken as follows:

$$
S(0) \geq 0, \ V(0) \geq 0, \ I_1(0) \geq 0, \ I_2(0) \geq 0, \ R(0) \geq 0.
$$

By summing all the equations in the system, we obtain

$$
N' = S' + V' + I_1' + I_2' + R'.
$$

From this equality, we get

$$
N' = B - \omega(S + V + I_1 + I_2 + R) - \omega_1 I_1 - \omega_2 I_2 = B - \omega N - \omega_1 I_1 - \omega_2 I_2 \leq B - \omega N.
$$
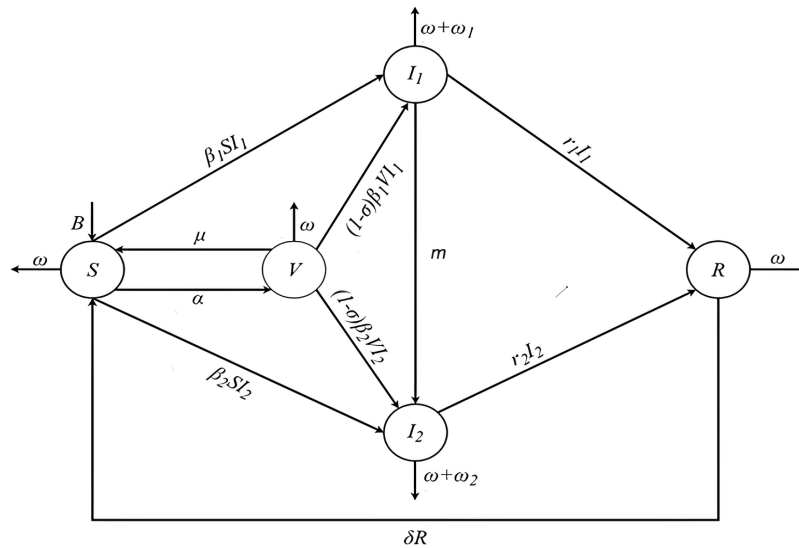
Figure 2.1: Flow diagram of the model

Thus, we have

$$D = \left\{ (S, V, I_1, I_2, R) \in \mathbb{R}_+^6 : N \le \frac{B}{\omega} \right\}$$

which is referred to as the biologically defined region of the mathematical model.

2.1. Disease-free equilibrium and endemic equilibrium

The disease-free equilibrium of the system (2.1) is

$$E_0 = (S_0, V_0, 0, 0, 0) = \left(\frac{B(\mu + \omega)}{\omega(\mu + \omega + \alpha)}, \frac{\alpha B}{\omega(\mu + \omega + \alpha)}, 0, 0, 0 \right)$$

and the endemic equilibrium of the system (2.1) is

$$E^e = (S^*, V^*, I_1^*, I_2^*, R^*) = \left(\frac{[B(\omega + \delta) + \delta(r_1 I_1^* + r_2 I_2^*)] \, C}{(\omega + \delta)[(\omega + \beta_1 I_1^* + \beta_2 I_2^* + \alpha) \, C - \mu \alpha]}, \frac{[B(\omega + \delta) + \delta(r_1 I_1^* + r_2 I_2^*)] \, \alpha}{(\omega + \delta)[(\omega + \beta_1 I_1 + \beta_2 I_2 + \alpha) \, C - \mu \alpha]}, I_1^*, I_2^*, \frac{r_1 I_1^* + r_2 I_2^*}{\omega + \delta} \right).$$

Here,

$$C = \omega + (1 - \sigma)\beta_1 I_1^* + (1 - \sigma)\beta_2 I_2^* + \mu.$$

2.2. Basic reproduction number

Ross created mathematical models of malaria transmission and identified a threshold value—now referred to as the basic reproduction number—in the second edition of his 1911 book *The Prevention of Malaria* [21]. R_0 represents the basic reproduction number, which is the expected number of secondary cases produced by a single infection in a fully susceptible population. Diekmann and Heesterbeek introduced the next-generation matrix in 1990, which is used to compute the basic reproduction number in compartmental models. To create the next-generation matrix in this study, we followed the methodology of Van den Driessche and Watmough [22]. Let V denote the Jacobian matrix of the remaining transition terms at the disease-free equilibrium, and let F denote the Jacobian matrix of the terms representing the rate of new infections in the infected compartments at the disease-free equilibrium. In this instance, the matrices F and V for model (2.1) are provided below:

$$F = \begin{bmatrix} \beta_1 S_0 + (1 - \sigma)\beta_1 V_0 & 0 \\ 0 & \beta_2 S_0 + (1 - \sigma)\beta_2 V_0 \end{bmatrix}, V = \begin{bmatrix} \omega + \omega_1 + m + r_1 & 0 \\ -m & \omega + \omega_2 + r_2 \end{bmatrix}.$$

For the system (2.1), the next-generation matrix is

$$K = FV^{-1} = \begin{bmatrix} \frac{\beta_1 S_0 + (1 - \sigma)\beta_1 V_0}{\omega + \omega_1 + m + r_1} & 0 \\ \frac{m(\beta_2 S_0 + (1 - \sigma)\beta_2 V_0)}{(\omega + \omega_1 + m + r_1)(\omega + \omega_2 + r_2)} & \frac{\beta_2 S_0 + (1 - \sigma)\beta_2 V_0}{(\omega + \omega_2 + r_2)} \end{bmatrix}.$$

The eigenvalues of this matrix are

$$\lambda_1 = \frac{\beta_1 S_0 + (1 - \sigma)\beta_1 V_0}{\omega + \omega_1 + m + r_1} = \frac{\beta_1 B(\mu + \omega) + (1 - \sigma)\beta_1 \alpha B}{(\omega + \omega_1 + m + r_1) \omega (\mu + \omega + \alpha)},$$

$$\lambda_2 = \frac{\beta_2 S_0 + (1-\sigma)\beta_2 V_0}{(\omega + \omega_2 + r_2)} = \frac{\beta_2 B(\mu + \omega) + (1-\sigma)\beta_2 \alpha B}{(\omega + \omega_2 + r_2)\,\omega\,(\mu + \omega + \alpha)}.$$

If we denote the basic reproduction number for individuals infected with the original virus by $\mathscr{R}_{01}$ and the basic reproduction number for individuals infected with the mutant virus by $\mathscr{R}_{02}$, then we can write:

$$\mathscr{R}_{01} = \frac{\beta_1 B(\mu + \omega) + (1-\sigma)\beta_1 \alpha B}{(\omega + \omega_1 + m + r_1)\,\omega\,(\mu + \omega + \alpha)}, \quad \mathscr{R}_{02} = \frac{\beta_2 B(\mu + \omega) + (1-\sigma)\beta_2 \alpha B}{(\omega + \omega_2 + r_2)\,\omega\,(\mu + \omega + \alpha)}.$$

3. Local Stability Analysis

In this section, we examined the local stability analysis of the disease-free equilibrium and endemic equilibrium points of the differential equation system representing the mathematical model.

3.1. Local asymptotic stability of the disease-free equilibrium

Theorem 3.1. *The disease-free equilibrium point of (2.1) is locally asymptotically stable when $\mathscr{R}_{01} < 1$ and $\mathscr{R}_{02} < 1$.*

Proof. The local stability analysis of a mathematical model is conducted using the Jacobian matrix. The sign of the eigenvalues, which are the roots of the characteristic polynomial formed by the Jacobian matrix, provides information about the stability of the nonlinear dynamic system. Considering the Jacobian matrix of the mathematical model (2.1) developed for COVID-19 at the disease-free equilibrium point E_0:

$$J_0 = \begin{bmatrix} f_{11} & f_{12} & f_{13} & f_{14} & f_{15} \\ f_{21} & f_{22} & f_{23} & f_{24} & 0 \\ 0 & 0 & f_{33} & 0 & 0 \\ 0 & 0 & f_{43} & f_{44} & 0 \\ 0 & 0 & f_{53} & f_{54} & f_{55} \end{bmatrix}$$

where,

$$\begin{aligned} f_{11} &= -\omega - \alpha, \quad f_{12} = \mu, \quad f_{13} = -\frac{\beta_1 B\,(\mu + \omega)}{\omega\,(\mu + \omega + \alpha)}, \quad f_{14} = -\frac{\beta_2 B\,(\mu + \omega)}{\omega\,(\mu + \omega + \alpha)}, \quad f_{15} = \delta, \\ f_{21} &= \alpha, \quad f_{22} = -\omega - \mu, \quad f_{23} = -\frac{(1-\sigma)\beta_1 \alpha B}{\omega\,(\mu + \omega + \alpha)}, \quad f_{24} = -\frac{(1-\sigma)\beta_2 \alpha B}{\omega\,(\mu + \omega + \alpha)}, \\ f_{25} &= 0, \quad f_{31} = 0, \quad f_{32} = 0, \quad f_{33} = -\omega - \omega_1 - m - r_1 + \frac{\beta_1\,(B\,(\mu + \omega) + \alpha B\,(1-\sigma))}{\omega\,(\mu + \omega + \alpha)}, \\ f_{34} &= 0, \quad f_{35} = 0, \quad f_{43} = m, \quad f_{44} = -\omega - \omega_2 - r_2 + \frac{\beta_2\,(B\,(\mu + \omega) + \alpha B\,(1-\sigma))}{\omega\,(\mu + \omega + \alpha)}, \\ f_{53} &= r_1, \quad f_{54} = r_2, \quad f_{55} = -\omega - \delta. \end{aligned}$$

The eigenvalues, which are the roots of the characteristic polynomial of this matrix, are

$$\tau_1 = -\omega, \quad \tau_2 = -(\omega + \alpha + \mu), \quad \tau_3 = (1 - \mathscr{R}_{01})(-\omega - \omega_1 - m - r_1), \quad \tau_4 = (1 - \mathscr{R}_{02})(-\omega - \omega_2 - r_2), \quad \tau_5 = -\omega - \delta.$$

The eigenvalues $\tau_{1,2,5}$ have negative real parts. Additionally, under the conditions

$$\mathscr{R}_{01} < 1, \quad \mathscr{R}_{02} < 1,$$

the eigenvalues $\tau_{3,4}$ also have negative real parts. Thus, the disease-free equilibrium point is locally asymptotically stable. $\qquad\square$

3.2. Local asymptotic stability of the endemic equilibrium

Theorem 3.2. *The endemic equilibrium point of (2.1) is locally asymptotically stable when $\mathscr{R}_{01} > 1$ and $\mathscr{R}_{02} > 1$.*

Proof. Considering the Jacobian matrix of the mathematical model (2.1) developed for COVID-19 at the endemic equilibrium point E^e:

$$J_e = \begin{bmatrix} d_{11} & d_{12} & d_{13} & d_{14} & d_{15} \\ d_{21} & d_{22} & d_{23} & d_{24} & 0 \\ d_{31} & d_{32} & d_{33} & 0 & 0 \\ d_{41} & d_{42} & d_{43} & d_{44} & 0 \\ 0 & 0 & d_{53} & d_{54} & d_{55} \end{bmatrix}$$

where,

$$
\begin{aligned}
d_{11} &= -\omega - \beta_1 I_1^* - \beta_2 I_2^* - \alpha, d_{12} = \mu, \\
d_{13} &= -\beta_1 S^* = -\beta_1 \frac{\left[B(\omega+\delta) + \delta\left(r_1 I_1^* + r_2 I_2^*\right)\right] C}{(\omega+\delta)\left[(\omega+\beta_1 I_1{}^* + \beta_2 I_2{}^* + \alpha) C - \mu\alpha\right]} \\
d_{14} &= -\beta_2 S^* = -\beta_2 \frac{\left[B(\omega+\delta) + \delta\left(r_1 I_1^* + r_2 I_2^*\right)\right] C}{(\omega+\delta)\left[(\omega+\beta_1 I_1{}^* + \beta_2 I_2{}^* + \alpha) C - \mu\alpha\right]}, \\
d_{15} &= \delta, d_{21} = \alpha, d_{22} = -\omega - (1-\sigma)\beta_1 I_1^* - (1-\sigma)\beta_2 I_2^* - \mu, \\
d_{23} &= -(1-\sigma)\beta_1 V^* = -(1-\sigma)\beta_1 \frac{\left[B(\omega+\delta) + \delta\left(r_1 I_1^* + r_2 I_2^*\right)\right] \alpha}{(\omega+\delta)\left[(\omega+\beta_1 I_1{}^* + \beta_2 I_2{}^* + \alpha) C - \mu\alpha\right]} \\
d_{24} &= -(1-\sigma)\beta_2 V^* = -(1-\sigma)\beta_2 \frac{\left[B(\omega+\delta) + \delta\left(r_1 I_1^* + r_2 I_2^*\right)\right] \alpha}{(\omega+\delta)\left[(\omega+\beta_1 I_1{}^* + \beta_2 I_2{}^* + \alpha) C - \mu\alpha\right]}, d_{25} = 0, \\
d_{31} &= \beta_1 I_1^*, d_{32} = (1-\sigma)\beta_1 I_1^*, d_{33} - \omega - \omega_1 - m - r_1 + \beta_1 \frac{\left[B(\omega+\delta) + \delta\left(r_1 I_1^* + r_2 I_2^*\right)\right]}{(\omega+\delta)\left[(\omega+\beta_1 I_1 + \beta_2 I_2 + \alpha) C - \mu\alpha\right]} [C + (1-\sigma)\,\alpha], \\
d_{34} &= 0, d_{35} = 0, d_{41} = \beta_2 I_2^*, d_{42} = (1-\sigma)\beta_2 I_2^*, d_{43} = m, \\
d_{44} &= -\omega - \omega_2 - r_2 + \beta_2 \frac{\left[B(\omega+\delta) + \delta\left(r_1 I_1^* + r_2 I_2^*\right)\right]}{(\omega+\delta)\left[(\omega+\beta_1 I_1 + \beta_2 I_2 + \alpha) C - \mu\alpha\right]} [C + (1-\sigma)\,\alpha], \\
d_{45} &= 0, d_{51} = 0, d_{52} = 0, d_{53} = r_1, d_{54} = r_2, d_{55} = -\omega - \delta.
\end{aligned}
$$

We can then construct the characteristic polynomial using this matrix:

$$det(J_e - \tau\,\mathrm{I}) = \tau^5 + k_1\tau^4 + k_2\tau^3 + k_3\tau^2 + k_4\tau + k_5 \tag{3.1}$$

Here, τ denotes the eigenvalues, and k_i, $i = 1, \ldots 5$, represents the coefficients. The coefficients k_i are provided in Appendix A. Thus, if the polynomial (3.1) satisfies the Routh-Hurwitz criteria given by:

$$k_1 > 0\,,\ \ k_2 > 0\,,\ \ k_3 > 0\,,\ \ k_4 > 0\,,\ \ k_5 > 0,$$

$$k_1 k_2 k_3 > k_3^2 + k_1^2 k_4,$$

$$(k_1 k_4 - k_5)\left(k_1 k_2 k_3 - k_3^2 - k_1^2 k_4\right) > k_5 (k_1 k_2 - k_3)^2 + k_1 k_5^2.$$

Then the endemic equilibrium point is locally asymptotically stable. □

4. Global Stability

In this section, we initially analyzed the global asymptotic stability of the disease-free equilibrium of model (2.1) by applying the Lyapunov-Krasovskii-LaSalle Stability Theorem. Then, we extended our investigation to the global stability of the endemic equilibrium using the same theorem.

4.1. Global asymptotic stability of the disease-free equilibrium

Theorem 4.1. *The disease-free equilibrium of model (2.1) is globally asymptotically stable when $\mathscr{R}_{01} < 1$ and $\mathscr{R}_{02} < 1$.*

Proof. To show that the disease-free equilibrium is globally asymptotically stable, we first define a linear Lyapunov function as follows:

$$L_0(t,\,S,V,I_1,I_2,R) = C_1 I_1 + C_2 I_2.$$

By taking the derivative of this function and substituting the expressions for $I_1{}'$ and $I_2{}'$ from the system (2.1), we obtain

$$
\begin{aligned}
\frac{dL_0}{dt} &= C_1 I_1{}' + C_2 I_2{}' \\
&= C_1\left(-\omega I_1 - \omega_1 I_1 - m I_1 - r_1 I_1 + \beta_1 S I_1 + (1-\sigma)\beta_1 V I_1\right) \\
&\quad + C_2\left(-\omega I_2 - \omega_2 I_2 + m I_1 - r_2 I_2 + \beta_2 S I_2 + (1-\sigma)\beta_2 V I_2\right) \\
&= (\mathscr{R}_{01} - 1) I_1 + (\mathscr{R}_{02} - 1) I_2 \leq 0
\end{aligned}
$$

where,

$$
\begin{aligned}
C_1 &= \frac{1}{\omega + \omega_1 + m + r_1} - \frac{m\omega(\mu + \omega + \alpha)}{(\omega + \omega_2 + r_2)\left[-(\omega + \omega_1 + m + r_1)\omega(\mu + \omega + \alpha) + \beta_1 B(\mu + \omega) + (1-\sigma)\beta_1 \alpha B\right]}, \\
C_2 &= \frac{1}{\omega + \omega_2 + r_2}.
\end{aligned}
$$

Thus, according to the Lyapunov Theorem, the disease-free equilibrium E_0 is globally asymptotically stable when $\mathscr{R}_{01} < 1$ and $\mathscr{R}_{02} < 1$. □

4.2. Global asymptotic stability of the endemic equilibrium

Theorem 4.2. *The endemic equilibrium of model (2.1) is globally asymptotically stable when $\mathscr{R}_{01} > 1$ and $\mathscr{R}_{02} > 1$.*

Proof. To determine the global stability of the endemic equilibrium, we introduce the following Lyapunov function:

$$L(t, S, V, I_1, I_2, R) = \kappa_1 \left(S - S^* - S^* \ln \frac{S}{S^*} \right) + \kappa_2 \left(V - V^* - V^* \ln \frac{V}{V^*} \right) + \kappa_3 \left(I_1 - I_1^* - I_1^* \ln \frac{I_1}{I_1^*} \right) + \kappa_4 \left(I_2 - I_2^* - I_2^* \ln \frac{I_2}{I_2^*} \right)$$

$$+ \kappa_5 \left(R - R^* - R^* \ln \frac{R}{R^*} \right).$$

Here, $\kappa_1 > 0$, $\kappa_2 > 0$, $\kappa_3 > 0$, $\kappa_4 > 0$ and $\kappa_5 > 0$. When $(S, V, I_1, I_2, R) = (S^*, V^*, I_1^*, I_2^*, R^*)$, $L = 0$, and otherwise $L > 0$. Additionally, L is radially unbounded and

$$L'(x) = \frac{d}{dt} L(x(t)) = \frac{\partial L}{\partial x} \frac{dx}{dt}.$$

Let's show that the derivative of L with respect to t is negative. The derivative of the Lyapunov function is given by

$$\frac{dL}{dt} = \kappa_1 \left(1 - \frac{S^*}{S} \right) S' + \kappa_2 \left(1 - \frac{V^*}{V} \right) V' + \kappa_3 \left(1 - \frac{I_1^*}{I_1} \right) I_1' + \kappa_4 \left(1 - \frac{I_2^*}{I_2} \right) I_2' + \kappa_5 \left(1 - \frac{R^*}{R} \right) R'.$$

Thus, by substituting the derivatives S', V', I_1', I_2', and R' from the system (2.1) and performing some simplifications, we obtain

$$\frac{dL}{dt} = -(\omega + \alpha) \kappa_1 \left(1 - \frac{1}{x_1} \right)^2 S + \kappa_1 \left(1 - \frac{1}{x_1} - x_3 x_1 + x_3 \right) \beta_1 S^* I_1^* + \kappa_1 \left(1 - \frac{1}{x_1} - x_4 x_1 + x_4 \right) \beta_2 S^* I_2^* + \kappa_1 \left(x_5 - \frac{x_5}{x_1} - 1 + \frac{1}{x_1} \right) \delta R^*$$

$$+ \kappa_1 \left(x_2 - \frac{x_2}{x_1} - 1 + \frac{1}{x_1} \right) \mu V^* + \left(-x_2 x_3 + x_3 + 1 - \frac{1}{x_2} \right) \beta_1 V^* I_1^* (1 - \sigma) \kappa_2 + \left(-x_2 x_4 + x_4 + 1 - \frac{1}{x_2} \right) \beta_2 V^* I_2^* (1 - \sigma) \kappa_2$$

$$+ \left(-1 + \frac{1}{x_3} + x_1 x_3 - x_1 \right) \beta_1 S^* I_1^* \kappa_3 + \left(-1 + \frac{1}{x_3} + x_2 x_3 - x_2 \right) \beta_1 V^* I_1^* (1 - \sigma) \kappa_3 + \left(-1 + \frac{1}{x_4} + x_1 x_4 - x_1 \right) \beta_2 S^* I_2^* \kappa_4$$

$$+ \left(-1 + \frac{1}{x_4} + x_2 x_4 - x_2 \right) \beta_2 V^* I_2^* (1 - \sigma) \kappa_4 + \left(-1 + \frac{1}{x_5} + x_3 - \frac{x_3}{x_5} \right) r_1 I_1^* \kappa_5 + \left(-1 + \frac{1}{x_5} + x_4 - \frac{x_4}{x_5} \right) r_2 I_2^* \kappa_5,$$

where

$$x_1 = \frac{S}{S^*}, \quad x_2 = \frac{V}{V^*}, x_3 = \frac{I_1}{I_1^*}, \quad x_4 = \frac{I_2}{I_2^*}, \quad x_5 = \frac{R}{R^*}.$$

If we take

$$T = \kappa_1 \beta_1 S^* I_1^* + \kappa_1 \beta_2 S^* I_2^* - \kappa_1 \delta R^* - \kappa_1 \mu V^* + \beta_1 V^* I_1^* (1 - \sigma) \kappa_2 + \beta_2 V^* I_2^* (1 - \sigma) \kappa_2 - \beta_1 S^* I_1^* \kappa_3 - \beta_1 V^* I_1^* (1 - \sigma) \kappa_3 - \beta_2 S^* I_2^* \kappa_4$$

$$- \beta_2 V^* I_2^* (1 - \sigma) \kappa_4 - r_1 I_1^* \kappa_5 - r_2 I_2^* \kappa_5 + (-\kappa_1 \beta_1 S^* I_1^* - \kappa_1 \beta_2 S^* I_2^* + \kappa_1 \delta R^* + \kappa_1 \mu V^*) \frac{1}{x_1} + (-\beta_1 S^* I_1^* \kappa_3 - \beta_2 S^* I_2^* \kappa_4) x_1$$

$$+ (-\beta_1 V^* I_1^* (1 - \sigma) \kappa_2 - \beta_2 V^* I_2^* (1 - \sigma) \kappa_2) \frac{1}{x_2} + (\kappa_1 \mu V^* - \beta_1 V^* I_1^* (1 - \sigma) \kappa_3 - \beta_2 V^* I_2^* (1 - \sigma) \kappa_4) x_2$$

$$+ (\beta_1 S^* I_1^* \kappa_3 + \beta_1 V^* I_1^* (1 - \sigma) \kappa_3) \frac{1}{x_3} + (\kappa_1 \beta_1 S^* I_1^* + \beta_1 V^* I_1^* (1 - \sigma) \kappa_2 + r_1 I_1^* \kappa_5) x_3 + (\beta_2 S^* I_2^* \kappa_4 + \beta_2 V^* I_2^* (1 - \sigma) \kappa_4) \frac{1}{x_4}$$

$$+ (\kappa_1 \beta_2 S^* I_2^* + \beta_2 V^* I_2^* (1 - \sigma) \kappa_2 + r_2 I_2^* \kappa_5) x_4 + (r_1 I_1^* \kappa_5 + r_2 I_2^* \kappa_5) \frac{1}{x_5} + (\kappa_1 \delta R^*) x_5 + (-\kappa_1 \beta_2 S^* I_2^* + \beta_2 S^* I_2^* \kappa_4) x_4 x_1$$

$$+ (-\beta_1 V^* I_1^* (1 - \sigma) \kappa_2 + \beta_1 V^* I_1^* (1 - \sigma) \kappa_3) x_2 x_3 + (-\beta_2 V^* I_2^* (1 - \sigma) \kappa_2 + \beta_2 V^* I_2^* (1 - \sigma) \kappa_4) x_2 x_4$$

$$+ (-\kappa_1 \beta_1 S^* I_1^* + \beta_1 S^* I_1^* \kappa_3) x_1 x_3 - \kappa_1 \delta R^* \frac{x_5}{x_1} - \kappa_1 \mu V^* \frac{x_2}{x_1} - r_1 I_1^* \kappa_5 \frac{x_3}{x_5} - r_2 I_2^* \kappa_5 \frac{x_4}{x_5},$$

then

$$\frac{dL}{dt} = -(\omega + \alpha) \kappa_1 \left(1 - \frac{1}{x_1} \right)^2 S + T(x_1, x_2, x_3, x_4, x_5).$$

Here

$$\kappa_1 = \kappa_2 = \kappa_3 = \kappa_4 = 1$$

implies that all the coefficients $x_4 x_1$, $x_2 x_3$, $x_2 x_4$, $x_1 x_3$ are zero. In this case, we can write T as follows:

$$T = -\left(-\frac{1}{x_3} + x_1 + \frac{1}{x_1} - x_3 \right) \beta_1 S^* I_1^* - \left(-\frac{1}{x_4} + x_1 + \frac{1}{x_1} - x_4 \right) \beta_2 S^* I_2^* - \left(-x_5 + \frac{x_5}{x_1} + 1 - \frac{1}{x_1} \right) \delta R^* - \left(-x_2 + \frac{x_2}{x_1} + 1 - \frac{1}{x_1} \right) \mu V^*$$

$$- \left(-\frac{1}{x_3} + x_2 - x_3 + \frac{1}{x_2} \right) \beta_1 V^* I_1^* (1 - \sigma) - \left(-\frac{1}{x_4} + x_2 - x_4 + \frac{1}{x_2} \right) \beta_2 V^* I_2^* (1 - \sigma) - \left(1 - \frac{1}{x_5} - x_3 + \frac{x_3}{x_5} \right) r_1 I_1^* \kappa_5$$

$$- \left(1 - \frac{1}{x_5} - x_4 + \frac{x_4}{x_5} \right) r_2 I_2^* \kappa_5.$$

If we take $x_1 = 1$, $x_2 = 1$, $x_3 = 1$, $x_4 = 1$ and $x_5 = 1$, then $T \leq 0$. Thus, we obtain

$$\frac{dL}{dt} = -(\omega + \alpha)\kappa_1\left(1 - \frac{1}{x_1}\right)^2 S + T(x_1, x_2, x_3, x_4, x_5) \leq 0.$$

According to LaSalle's Theorem, the invariant set is defined by

$$\Omega = \{x \in \mathbb{R}^n : L'(x) = 0\}.$$

Since the invariant set contains only the endemic equilibrium $(S^*, V^*, I_1^*, I_2^*, R^*)$, we conclude that the endemic equilibrium is globally asymptotically stable. □

5. Backward Bifurcation

The basic reproduction number, or $\mathscr{R}_0$, is a threshold value that determines the qualitative dynamics of epidemiological models. By altering the bifurcation parameter, which is known as the fundamental reproduction number, backward bifurcation is investigated. Note that $\mathscr{R}_0$ is a sum of the model's parameters. Generally speaking, the illness will eventually go away if $\mathscr{R}_0 < 1$. An infected person can convey the disease to multiple people if $\mathscr{R}_0 > 1$, which permits the sickness to spread across the population. However, the disease may continue to spread in some situations even though $\mathscr{R}_0 < 1$. Backward bifurcation is a phenomena that occurs in these situations [23]. We used the Castillo-Chavez and Song Bifurcation Theorem to do a bifurcation analysis in this study.
Initially, we demonstrated the presence of backward bifurcation for the original virus. For this purpose, we selected β_1 as the bifurcation parameter and determined β_1 by setting $R_{01} = 1$. In this case, we get

$$\beta_1 = \beta_1^* = \frac{\omega(\omega + \omega_1 + m + r_1)(\mu + \omega + \alpha)}{B(\mu + \omega) + (1 - \sigma)\alpha B}.$$

By substituting this parameter value into the Jacobian matrix J_0, given in (3.1), we obtain

$$J_{(E_0, \beta_1^*)} = \begin{bmatrix} g_{11} & g_{12} & g_{13} & g_{14} & g_{15} \\ g_{21} & g_{22} & g_{23} & g_{24} & 0 \\ 0 & 0 & 0 & 0 & 0 \\ 0 & 0 & g_{43} & g_{44} & 0 \\ 0 & 0 & g_{53} & g_{54} & g_{55} \end{bmatrix}.$$

Here,

$$g_{11} = -\omega - \alpha, \quad g_{12} = \mu, \quad g_{13} = -\frac{(\omega + \omega_1 + m + r_1)(\mu + \omega)}{(\mu + \omega) + (1 - \sigma)\alpha}, \quad g_{14} = -\frac{\beta_2 B(\mu + \omega)}{\omega(\mu + \omega + \alpha)}, \quad g_{15} = \delta,$$

$$g_{21} = \alpha, \quad g_{22} = -\omega - \mu, \quad g_{23} = -\frac{(\omega + \omega_1 + m + r_1)(1 - \sigma)\alpha}{(\mu + \omega) + (1 - \sigma)\alpha}, \quad g_{24} = -\frac{(1 - \sigma)\beta_2\alpha B}{\omega(\mu + \omega + \alpha)}, \quad g_{33} = 0, \quad g_{43} = m,$$

$$g_{44} = -\omega - \omega_2 - r_2 + \frac{\beta_2(B(\mu + \omega) + \alpha B(1 - \sigma))}{\omega(\mu + \omega + \alpha)}, \quad g_{53} = r_1, \quad g_{54} = r_2, \quad g_{55} = -\omega - \delta.$$

The characteristic polynomial and eigenvalues of the matrix $J_{(E_0, \beta_1^*)}$ are as follows:

$$\begin{aligned} \left| J_{(E_0, \beta_1^*)} - \tau I \right| &= [(g_{11} - \tau)(g_{22} - \tau) - g_{21} g_{12}][(-\tau)(g_{44} - \tau)(g_{55} - \tau)] \\ &= \left[\tau^2 + (2\omega + \alpha + \mu)\tau + (\omega^2 + \omega\mu + \alpha\omega)\right](-\tau)\left(-\omega - \omega_2 - r_2 + \frac{\beta_2(B(\mu + \omega) + \alpha B(1 - \sigma))}{\omega(\mu + \omega + \alpha)} - \tau\right)(-\omega - \delta - \tau), \end{aligned}$$

$$\tau_1 = -\omega, \quad \tau_2 = -(\omega + \alpha + \mu), \quad \tau_3 = 0, \tau_4 = -\omega - \omega_2 - r_2 + \frac{\beta_2(B(\mu + \omega) + \alpha B(1 - \sigma))}{\omega(\mu + \omega + \alpha)}, \quad \tau_5 = -\omega - \delta.$$

The matrix $J_{(E_0, \beta_1^*)}$ has a simple zero eigenvalue, while the remaining eigenvalues are negative. Now let's find the right eigenvector $w = (w_1, w_2, w_3, w_4, w_5)$ and the left eigenvector $v = (v_1, v_2, v_3, v_4, v_5)$ corresponding to the zero eigenvalue. For this, we must first find the solution of the equation.

$$J_{(E_0, \beta_1^*)} w = 0.$$

When we solve this equation, we obtain the components of the right eigenvector as follows: $w = (w_1, w_2, w_3, w_4, w_5)$,

$$w_1 = \frac{(\omega + \mu)X + \mu(\omega + \delta)Y}{m(\omega + \delta)[(\mu + \omega) + (1 - \sigma)\alpha][-\omega(\omega + \mu + \alpha)]},$$

$$w_2 = \frac{\alpha X + (\omega + \alpha)(\omega + \delta)Y}{m(\omega + \delta)[(\mu + \omega) + (1 - \sigma)\alpha][-\omega(\omega + \mu + \alpha)]},$$

$$w_3 = \frac{(1 - R_{02})}{m}A_1,$$

$$w_4 = \omega(\mu + \omega + \alpha),$$

$$w_5 = \frac{r_1(1 - R_{02})A_1 + r_2 m\omega(\mu + \omega + \alpha)}{m(\omega + \delta)},$$

where,

$$A_1 = \omega\,(\mu + \omega + \alpha)\,(\omega + \omega_2 + r_2),$$

$$
\begin{aligned}
X = {}& (\omega + \omega_1 + m + r_1)\,(\mu + \omega)\,(\omega + \delta)\,(1 - R_{02})A_1 + \beta_2 B\,(\mu + \omega)\,m\,(\omega + \delta)\,[(\mu + \omega) + (1 - \sigma)\,\alpha] \\
& - \delta\,[r_1\,(1 - R_{02})A_1 + r_2 m \omega\,(\mu + \omega + \alpha)]\,[(\mu + \omega) + (1 - \sigma)\,\alpha],
\end{aligned}
$$

$$Y = (\omega + \omega_1 + m + r_1)\,(1 - \sigma)\,\alpha\,(1 - R_{02})A_1 + (1 - \sigma)\,\beta_2 \alpha B m\,[(\mu + \omega) + (1 - \sigma)\,\alpha].$$

Similarly, if we solve the system v $J_{(E_0, \beta_1^*)} = 0$, the components of the left eigenvector are obtained as follows: $v_1 = 0$, $v_2 = 0$, $v_3 = 1$, $v_4 = 0$, $v_5 = 0$. Now, let us calculate the bifurcation constants a and b as given in [13]:

$$a = \sum_{k,\,i,\,j=1}^{n} v_k\,w_i\,w_j\,\frac{\partial^2 f_k}{\partial x_i \partial x_j}\,(0,0) \tag{5.1}$$

$$b = \sum_{k,\,i=1}^{n} v_k\,w_i\,\frac{\partial^2 f_k}{\partial x_i \partial \phi}\,(0,0). \tag{5.2}$$

Let's rewrite the system (2.1) as follows:

$$
\begin{aligned}
\frac{dx_1}{dt} &= \mathrm{B} - \omega x_1 - \beta_1 x_1 x_3 - \beta_2 x_1 x_4 - \alpha x_1 + \mu x_2 + \delta x_5 = f_1 \\
\frac{dx_2}{dt} &= -\omega x_2 - (1 - \sigma)\beta_1 x_2 x_3 - (1 - \sigma)\beta_2 x_2 x_4 + \alpha x_1 - \mu x_2 = f_2 \\
\frac{dx_3}{dt} &= -\omega x_3 - \omega_1 x_3 - m x_3 - r_1 x_3 + \beta_1 x_1 x_3 + (1 - \sigma)\beta_1 x_2 x_3 = f_3 \\
\frac{dx_4}{dt} &= -\omega x_4 - \omega_2 x_4 + m x_3 - r_2 x_4 + \beta_2 x_1 x_4 + (1 - \sigma)\beta_2 x_2 x_4 = f_4 \\
\frac{dx_5}{dt} &= -\omega x_5 + r_1 x_3 + r_2 x_4 - \delta x_5 = f_5.
\end{aligned}
$$

By calculating the required partial derivatives in (5.1) and (5.2) and writing those that are non-zero, we obtain

$$
\begin{aligned}
a = {}& -\frac{(1 - R_{02})^2 A_1{}^2 (\omega + \omega_1 + m + r_1)^2\,(\mu + \omega)}{m^2 B\,[(\mu + \omega) + (1 - \sigma)\,\alpha]} - (1 - R_{02})A_1\,(\omega + \omega_1 + m + r_1)\,(\mu + \omega)\,\beta_2 \\
& -\frac{[\mu + (1 - \sigma)(\omega + \alpha)]\,(\omega + \omega_1 + m + r_1)^2\,(1 - \sigma)\,\alpha(1 - R_{02})^2 A_1{}^2}{m^2 B[(\mu + \omega) + (1 - \sigma)\,\alpha]^2} - \frac{[\mu + (1 - \sigma)(\omega + \alpha)]\,(1 - \sigma)\,\beta_2 \alpha\,(1 - R_{02})A_1\,(\omega + \omega_1 + m + r_1)}{m\,[(\mu + \omega) + (1 - \sigma)\,\alpha]} \\
& +\delta\,\frac{(1 - R_{02})A_1\,(\omega + \omega_1 + m + r_1)\,w_5}{mB}
\end{aligned}
$$

and

$$b = \frac{(1 - R_{02})}{m}A_1\,[S_0 + (1 - \sigma)\,V_0].$$

Since $R_{02} > 0$, $S_0 > 0$, $V_0 > 0$ and $1 - \sigma > 0$, it follows that $b > 0$. To ensure that the condition $a > 0$ is met, the parameter δ must

$$
\begin{aligned}
\delta > \delta^* = {}& \frac{1}{w_5}\frac{(1 - R_{02})A_1\,(\omega + \omega_1 + m + r_1)\,(\mu + \omega)}{m\,[(\mu + \omega) + (1 - \sigma)\,\alpha]} + (\mu + \omega)\,\beta_2 B + \frac{[\mu + (1 - \sigma)(\omega + \alpha)]\,(\omega + \omega_1 + m + r_1)\,(1 - \sigma)\,\alpha\,(1 - R_{02})A_1}{m\,[(\mu + \omega) + (1 - \sigma)\,\alpha]^2} \\
& +\frac{[\mu + (1 - \sigma)(\omega + \alpha)]\,(1 - \sigma)\,\beta_2 \alpha B}{[(\mu + \omega) + (1 - \sigma)\,\alpha]}
\end{aligned} \tag{5.3}
$$

satisfy the condition. Therefore, according to the Castillo-Chavez and Song Bifurcation Theorem, backward bifurcation will occur for β_1 if the condition given in equation (5.3) is satisfied. Taking $\mathscr{R}_{02} = 1$, we obtain the bifurcation parameter β_2 as follows:

$$\beta_2 = \beta_2^* = \frac{\omega\,(\omega + \omega_2 + r_2)\,(\mu + \omega + \alpha)}{B(\mu + \omega) + (1 - \sigma)\,\alpha B}.$$

By substituting β_2^* into the Jacobian matrix J_0 at the disease-free equilibrium, we obtain

$$
J_{(E_0, \beta_2^*)} =
\begin{bmatrix}
k_{11} & k_{12} & k_{13} & k_{14} & k_{15} \\
k_{21} & k_{22} & k_{23} & k_{24} & 0 \\
0 & 0 & k_{33} & 0 & 0 \\
0 & 0 & k_{43} & 0 & 0 \\
0 & 0 & k_{53} & k_{54} & k_{55}
\end{bmatrix},
$$

where,

$$k_{11} = -\omega - \alpha, k_{12} = \mu, \quad k_{13} = -\frac{\beta_1 B\,(\mu + \omega)}{\omega\,(\mu + \omega + \alpha)}, \quad k_{14} = -\frac{(\omega + \omega_2 + r_2)\,(\mu + \omega)}{(\mu + \omega) + (1 - \sigma)\,\alpha},$$

$$k_{15} = \delta, k_{21} = \alpha, k_{22} = -\omega - \mu, \quad k_{23} = -\frac{(1 - \sigma)\,\beta_1\,\alpha B}{\omega\,(\mu + \omega + \alpha)},$$

$$k_{24} = -\frac{(\omega + \omega_2 + r_2)\,(1 - \sigma)\,\alpha}{(\mu + \omega) + (1 - \sigma)\,\alpha}, \quad k_{33} = -\omega - \omega_1 - m - r_1 + \frac{\beta_1\,(B\,(\mu + \omega) + \alpha B\,(1 - \sigma))}{\omega\,(\mu + \omega + \alpha)},$$

$$k_{43} = m, \quad k_{44} = 0, \quad k_{53} = r_1, \quad k_{54} = r_2, \quad k_{55} = -\omega - \delta$$

The characteristic polynomial and eigenvalues of the matrix $J_{(E_0, \beta_2^*)}$ are

$$\left| J_{(E_0, \beta_2^*)} - \tau I \right| = \left[(k_{11} - \tau)\,(k_{22} - \tau) - k_{21}\,k_{12} \right] \left[(k_{33} - \tau)\,(-\tau)\,(k_{55} - \tau) \right]$$

$$= \left[\tau^2 + (2\omega + \alpha + \mu)\,\tau + \left(\omega^2 + \omega\mu + \alpha\omega \right) \right] (k_{33} - \tau)\,(-\tau)\,(-\omega - \delta - \tau),$$

$$\tau_1 = -\omega, \quad \tau_2 = -(\omega + \alpha + \mu), \quad \tau_3 = -\omega - \omega_1 - m - r_1 + \frac{\beta_1\,(B\,(\mu + \omega) + \alpha B\,(1 - \sigma))}{\omega\,(\mu + \omega + \alpha)}, \quad \tau_4 = 0, \quad \tau_5 = -\omega - \delta.$$

It is observed that the matrix $J_{(E_0, \beta_2^*)}$ has a simple zero eigenvalue at E_0 and $\beta_2 = \beta_2^*$, while the remaining eigenvalues are negative. If the procedures performed for β_1 are repeated for β_2,

$$w_{33} = 0, \quad w_{44} = 1, \quad w_{55} = \frac{r_2}{\omega + \delta},$$

$$w_{22} = \frac{\alpha\,(\omega + \omega_2 + r_2)\,(\mu + \omega)\,(\omega + \delta) - \alpha\delta r_2\,[(\mu + \omega) + (1 - \sigma)\,\alpha] + (\omega + \alpha)\,(\omega + \omega_2 + r_2)\,(1 - \sigma)\,\alpha\,(\omega + \delta)}{[-\omega\,(\omega + \mu + \alpha)]\,[(\mu + \omega) + (1 - \sigma)\,\alpha]\,(\omega + \delta)}$$

$$w_{11} = \frac{(\omega + \omega_2 + r_2)\,(\mu + \omega)^2\,(\omega + \delta) - (\omega + \mu)\,\delta r_2\,[(\mu + \omega) + (1 - \sigma)\,\alpha] + \mu\,(\omega + \omega_2 + r_2)\,(1 - \sigma)\,\alpha\,(\omega + \delta)}{[-\omega\,(\omega + \mu + \alpha)]\,[(\mu + \omega) + (1 - \sigma)\,\alpha]\,(\omega + \delta)}$$

resulting in the right eigenvector $w_1 = (w_{11}, w_{22}, w_{33}, w_{44}, w_{55})$ and

$$v_{11} = 0, \quad v_{22} = 0, \quad v_{55} = 0, \quad v_{44} = 1, \quad v_{33} = \frac{-m\omega\,(\mu + \omega + \alpha)}{-(\omega + \omega_1 + m + r_1)\,\omega\,(\mu + \omega + \alpha) + \beta_1 B\,[(\mu + \omega) + \alpha\,(1 - \sigma)]}$$

resulting in the left eigenvector $v_1 = (v_{11}, v_{22}, v_{33}, v_{44}, v_{55})$. In this case, the bifurcation constants a and b are

$$a = -(\omega + \omega_2 + r_2)\frac{(\omega + \omega_2 + r_2)\,(\mu + \omega)\,[(\mu + \omega) + (1 - \sigma)\,\alpha] + (\omega + \omega_2 + r_2)\,(1 - \sigma)\,\alpha\,[\mu + (\omega + \alpha)\,(1 - \sigma)]}{B[(\mu + \omega) + (1 - \sigma)\,\alpha]^2}$$

$$+ \delta\,w_{55}\frac{(\omega + \omega_2 + r_2)}{B}$$

and

$$b = S_0 + (1 - \sigma)\,V_0.$$

It can be easily seen that $b > 0$. If the condition

$$\delta > \delta^* = \frac{1}{w_{55}}\frac{(\omega + \omega_2 + r_2)\,(\mu + \omega)\,[(\mu + \omega) + (1 - \sigma)\,\alpha] + (\omega + \omega_2 + r_2)\,(1 - \sigma)\,\alpha\,[\mu + (\omega + \alpha)\,(1 - \sigma)]}{[(\mu + \omega) + (1 - \sigma)\,\alpha]^2}, \tag{5.4}$$

then the constant a will be positive. Since the constant b is also positive, a backward bifurcation occurs at the point $\beta_2 = \beta_2^*$ due to the Castillo-Chavez and Song Bifurcation Theorem.

Theorem 5.1. *Consider the system (2.1). A backward bifurcation occurs in system (2.1) if inequalities (5.3) and (5.4) hold at $\mathscr{R}_{01} = 1$ and $\mathscr{R}_{02} = 1$.*

6. Parameter Estimation

Certain parameters, such as birth rates, natural mortality rates, and recovery rates, can be directly inferred from population and epidemiological data. However, other parameters may not be as straightforward to estimate from direct observations. For more complex models or for the estimation of multiple parameters simultaneously, a systematic approach is essential [24]. Consequently, parameter estimation methodologies should be employed to accurately determine these parameters.

In this section, our goal is to estimate the model parameters by fitting the nonlinear ordinary differential equation system we developed to the disease data in order to study the dynamics of COVID-19 infection. In our study, we conducted a model analysis using the data of COVID-19 cases reported in Turkey between December 20, 2021, and January 31, 2022. We solved the system using Python's ***odeint*** function and then estimated the parameters of the $SVI_1 I_2 R$ model by calculating the error between the model's predictions and the actual data with the help of the ***fit_model*** function. Using this function, we optimized the model parameters β_1, β_2, m. Subsequently, we employed the ***minimize*** function to minimize the error function. Finally, we visualized the solutions in comparison with the data.

In the model we developed for the COVID-19 pandemic, there are 13 different parameter values. The initial values of these parameters are provided in Table 6.1. We estimated the transmissibility rate of the original virus (β_1), the transmissibility rate of the mutant virus (β_2), and the mutation rate (m). For the initial values of these parameters, we used $\beta_1 = 0.000000004$, $\beta_2 = 0.0000000085$ and $m = 0.01$. The optimal values for these parameters were found to be $\beta_1 = 0.000000001167817614$, $\beta_2 = 0.000000007368542050$, and $m = 0.009308731535398908$.

Parameters	Description	Initial value	Source
B	Natural birth rate	2993	[25]
ω	Natural death rate	0.00003535	[26]
β_1	Transmission rate of the original virus	0.000000001167817614	Estimated
β_2	Transmission rate of the mutant virus	0.000000007368542050	Estimated
α	Vaccination rate of susceptible individuals	0.012	Assumed
μ	Rate of decline in vaccine-induced immunity	0.005 day	Assumed
δ	Rate of decline in immunity gained through infection	0.0027 day	[27], [28]
σ	Vaccine efficacy	0.9	Assumed
ω_1	Additional mortality rate caused by the original virus	0.005579	[29]
ω_2	Additional mortality rate caused by the mutant virus	0.002286	[29]
m	Mutation rate	0.009308731535398908	Estimated
r_1	Recovery rate for the original virus	0.0833	[24]
r_2	Recovery rate for the mutant virus	0.1	[24]

Table 6.1: Initial values of parameters

7. Sensitivity Analysis

Sensitivity analysis investigates how uncertainty in the outputs of a model can be attributed to uncertainties in its input parameters [30]. In epidemiological modeling, crucial static quantities, such as the basic reproduction number, equilibrium prevalence, and equilibrium incidence, are directly influenced by parameters within differential equation models. Understanding the response of these key quantities to parameter variations is essential. The effect of changing a parameter p on an output quantity Q is quantified by the derivative of Q with respect to p. Consequently, sensitivity analysis is typically considered a local measure that evaluates the influence of individual inputs on specific outputs [23]. This type of analysis, termed local sensitivity analysis, involves calculating partial derivatives of the output function with respect to input parameters, assuming the input parameters have minimal uncertainty [31]. The sensitivity index, representing the change in the output Q with respect to a parameter p, is calculated as follows:

$$\mathscr{Z}_p^Q = \frac{p}{Q}\frac{\partial Q}{\partial p}$$

The sensitivity index for each model parameter associated with the basic reproductive number was determined in this section. We gave these index values of the model parameters in Table 7.1. This index shows how important each model parameter is in relation to how it affects the spread of COVID-19. The basic reproductive number is the aim of interventions, and the index is used to determine which parameter has the biggest impact on it. In order to effectively manage the COVID-19 outbreak, parameters that significantly affect the fundamental reproductive number are essential [32]. We calculated the sensitivity indices of $\mathscr{R}_{01}$ and $\mathscr{R}_{02}$ for all model parameters in our mathematical model using the following formulas:

$$\mathscr{Z}_p^{\mathscr{R}_{01}} = \frac{p}{\mathscr{R}_{01}}\frac{\partial \mathscr{R}_{01}}{\partial p}, \qquad \mathscr{Z}_p^{\mathscr{R}_{02}} = \frac{p}{\mathscr{R}_{02}}\frac{\partial \mathscr{R}_{02}}{\partial p}.$$

The parameters B, β_1, μ have positive sensitivity indices for $\mathscr{R}_{01}$, while the parameters B, β_2, μ have positive sensitivity indices for $\mathscr{R}_{02}$. We have given the visual representation of the sensitivity indices in Figure 7.1 and Figure 7.2. Positive sensitivity indices indicate that an increase in the basic reproduction number is significant. In other words, increasing (or decreasing) the value of these parameters, while keeping other parameters constant, will lead to increases (or decreases) in the basic reproduction number. Conversely, the parameters ω, α, σ, ω_1, m, r_1 have negative sensitivity indices for $\mathscr{R}_{01}$ and the parameters ω, α, $\acute{o}$, ω_2, r_2 have negative sensitivity indices for $\mathscr{R}_{02}$. Negative sensitivity indices indicate that an increase in the basic reproduction number is of negative significance. In other words, increasing (or decreasing) the value of these parameters, while keeping other parameters constant, will result in decreases (or increases) in the basic reproduction number.

Parameter	Value	Sensitivity index value ($\mathscr{R}_{01}$)	Analysis	Sensitivity index value ($\mathscr{R}_{02}$)	Analysis
B	2993	1	Positive	1	Positive
ω	0.00003535	-0.9971	Negative	-0.99635	Negative
β_1	0.000000001167817614	1	Positive	0	Neutral
β_2	0.000000007368542050	0	Neutral	1	Positive
α	0.01795	-0.5116	Negative	-0.297	Negative
μ	0.005	0.5084	Positive	0.5084	Positive
δ	0.0027	0	Neutral	0	Neutral
σ	0.9	-1.7320	Negative	-1.7320	Negative
ω_1	0.005579	-0.0568	Negative	0	Neutral
ω_2	0.002286	0	Neutral	-0.02234	Negative
m	0.009308731535398908	-0.0948	Negative	0	Neutral
r_1	0.0833	-0.8481	Negative	0	Neutral
r_2	0.1	0	Neutral	-0.9773	Negative

Table 7.1: Sensitivity indices of $\mathscr{R}_{01}$ and $\mathscr{R}_{02}$ with respect to all model parameters
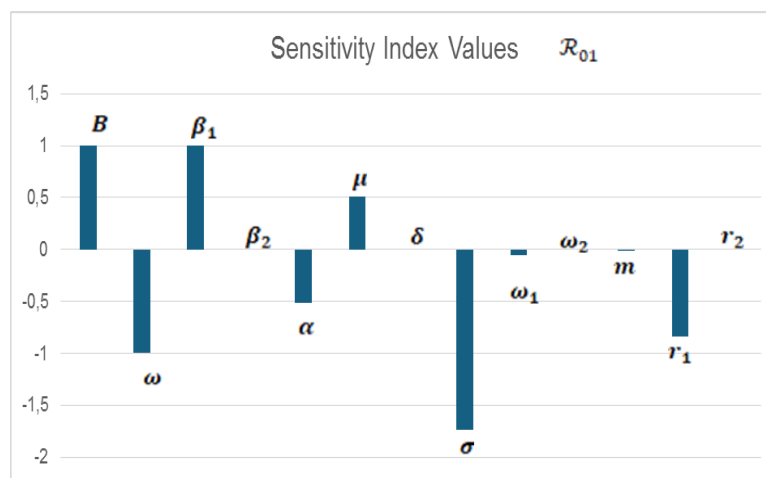
Figure 7.1: Basic reproduction number $\mathscr{R}_{01}$ and sensitivity index values of the parameters
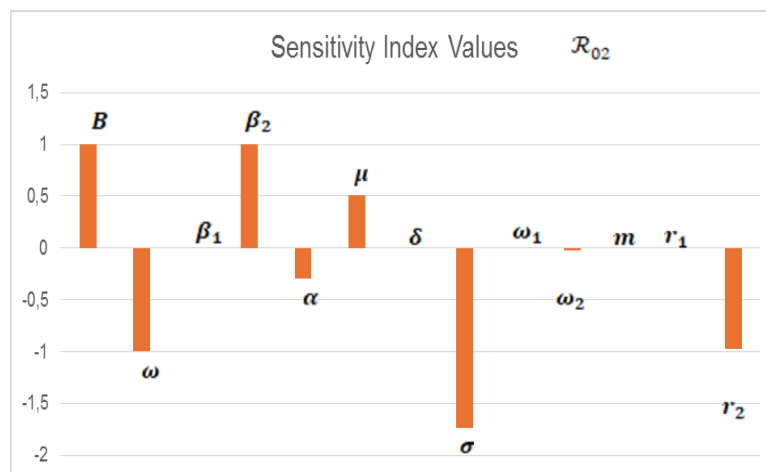
Figure 7.2: Basic reproduction number $\mathscr{R}_{02}$ and sensitivity index values of the parameters

In conclusion, the average number of secondary cases generated by a primary case in a fully susceptible population will increase if the values of the parameters B, β_1 and μ for $\mathscr{R}_{01}$ and B, β_2 and μ for $\mathscr{R}_{02}$ are increased. The average number of secondary cases generated by a primary case in a fully susceptible population will also increase if the values of the parameters ω, α, σ, ω_1, m, and r_1 for $\mathscr{R}_{01}$ and ω, α, σ, ω_2 and r_2 for $\mathscr{R}_{02}$ are decreased.

σ (vaccine efficacy) is the parameter to which the basic reproduction numbers $\mathscr{R}_{01}$ and $\mathscr{R}_{02}$ are most sensitive. The average number of secondary cases spread by an infected person in a community that is totally susceptible will rise if the value of this parameter decreases. This implies that a sick person may convey the disease to several people as vaccine efficacy declines, causing the disease to gradually spread

across the population. Because of this negative sensitivity connection with the fundamental reproduction number, our model emphasizes the significance of vaccine efficacy in epidemic control efforts.

8. Simulations

In this section, we present several graphical representations of the dynamic behavior of the model system to illustrate the basic principles of the dynamics of our model and to support the analytical results. We consider the following initial conditions:

$$S(0) = 26195740, \ V = 51202223, \ I_1(0) = 269725, \ I_2(0) = 2724, \ R(0) = 7009861$$

Simulation 1. Here, we discuss the graphical representations of the behavior of the compartments infected with the original virus (I_1) and those infected with the mutant virus (I_2) for different values of the vaccine efficacy parameter (σ), along with an analysis of their impact on the epidemic.

In Figure 8.1, we examined the temporal variation of I_1 for different values of the vaccine efficacy parameter σ. The figure illustrates how the dynamics of individuals infected with the original virus evolve as the vaccine efficacy takes on different values. This analysis is crucial for understanding the role of vaccine efficacy in controlling the outbreak of the original virus and its impacts on the population.

All curves start from the same point on day 0, indicating a large number of infected individuals in the population who were either unvaccinated or unaffected by the vaccine at the outset. This reveals that the virus spread rapidly at the beginning of the outbreak, leading to a swift increase in the number of infected individuals. $\sigma = 0$ represents the case where vaccine efficacy is zero, depicting a scenario in which the population is completely unvaccinated. The infection persists actively within the community for approximately 50 days before it starts to decline, although its complete eradication takes a longer period. This scenario demonstrates that in the absence of a vaccine, the virus continues to affect the population for an extended duration. In this case, the number of infected individuals reaches its peak and declines more slowly. This indicates that the outbreak will last longer and infect more individuals compared to scenarios where vaccines are present. At $\sigma = 0.7$, although there is a reduction in the number of infected individuals, this decrease occurs more gradually, and the outbreak persists for a longer duration within the population. Around day 40, the number of infected individuals approaches zero. At $\sigma = 0.8$, as vaccine efficacy increases, the reduction in the number of infected individuals accelerates further. With this value, the infection is observed to extinguish in a shorter period. Approximately 30 days later, the number of infected individuals approaches zero. This scenario underscores the significance of implementing a highly effective vaccine in controlling the spread of the virus within the community. At $\sigma = 0.9$, there is a rapid decrease in the number of infected individuals, and the outbreak is controlled in a shorter time frame, reaching near zero in approximately 25 days. In this scenario, the vaccination program provides protection to a significant portion of the community, leading to a swift eradication of the virus. The rate of infection spread has nearly come to a standstill.
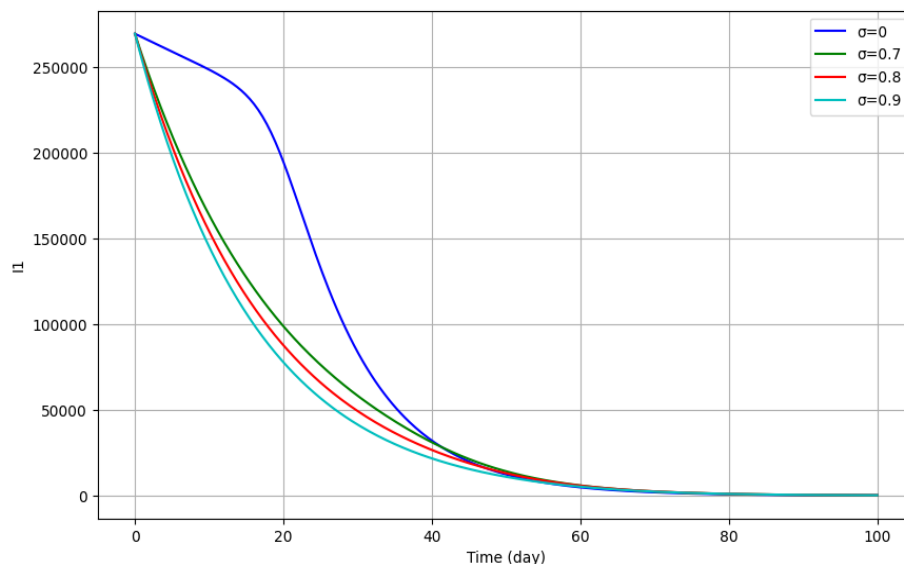
Figure 8.1: The spread dynamics of the original virus for different values of σ (vaccine efficacy).

The graph serves as a clear demonstrator of the relationship between vaccine efficacy and the number of infected individuals, highlighting the critical importance of widespread vaccine use and efficacy for the future of epidemics. High vaccine efficacy (high values of σ) will lead to a rapid decrease in the number of infected individuals within the community, resulting in a shorter duration of the outbreak. This is significant for alleviating the burden on hospitals, minimizing economic impacts, and protecting overall public health. Such an effective vaccine also plays a crucial role in preventing new waves of outbreaks. Conversely, low vaccine efficacy (low values of σ) indicates that the number of infected individuals declines more slowly, leading to a longer duration for the outbreak to be controlled. This can result in prolonged infection and a greater number of affected individuals. Scenarios with low vaccine efficacy may also signal the emergence of new variants and the risk of resurgence of the outbreak.

Figure 8.2: The spread dynamics of the mutant virus for different values of σ (vaccine efficacy).

In conclusion, there is a strong relationship between vaccine efficacy and the course of the outbreak. A more effective vaccination strategy plays a vital role in both shortening the duration of the outbreak and protecting public health. When vaccine efficacy is low, the likelihood of infected individuals remaining under the influence of the outbreak for an extended period increases, and the risk of long-term effects from the outbreak in the future grows.

The trend in the number of people infected with the mutant virus is depicted in Figure 8.2. When immunization is not administered, I_2 peaks on day 23 with about 4×10^7 people infected with the mutant virus. The peak of I_2 in the case of vaccination ($\sigma = 0.7$) happens on day 47, with roughly 1.9×10^7 people infected. It is evident that immunization lowers and delays the I_2 peak. Consequently, I_2's peak is delayed by 24 days. Even with a $\sigma = 0.7$ vaccination efficacy, the outbreak's impact on medical resources will be greatly lessened, enabling more people to obtain prompt medical care and lowering death rates.
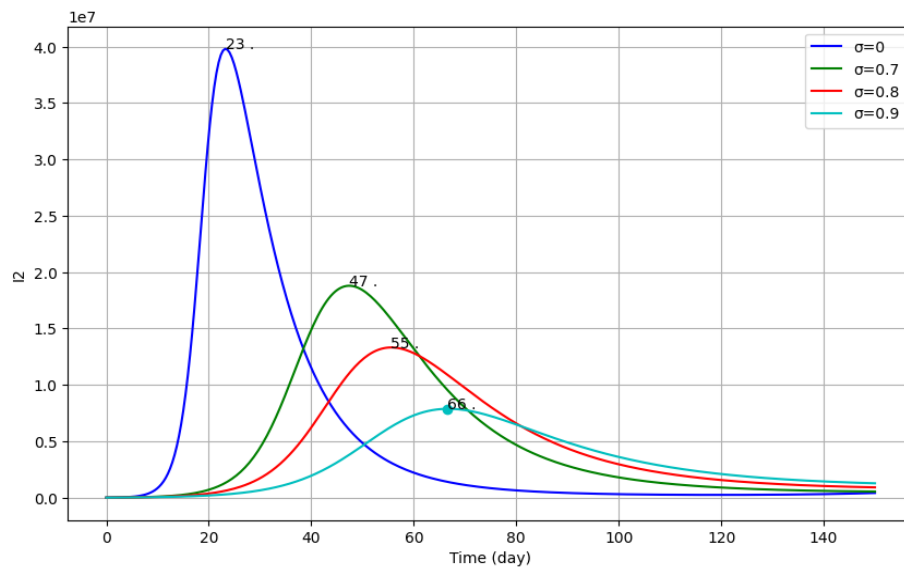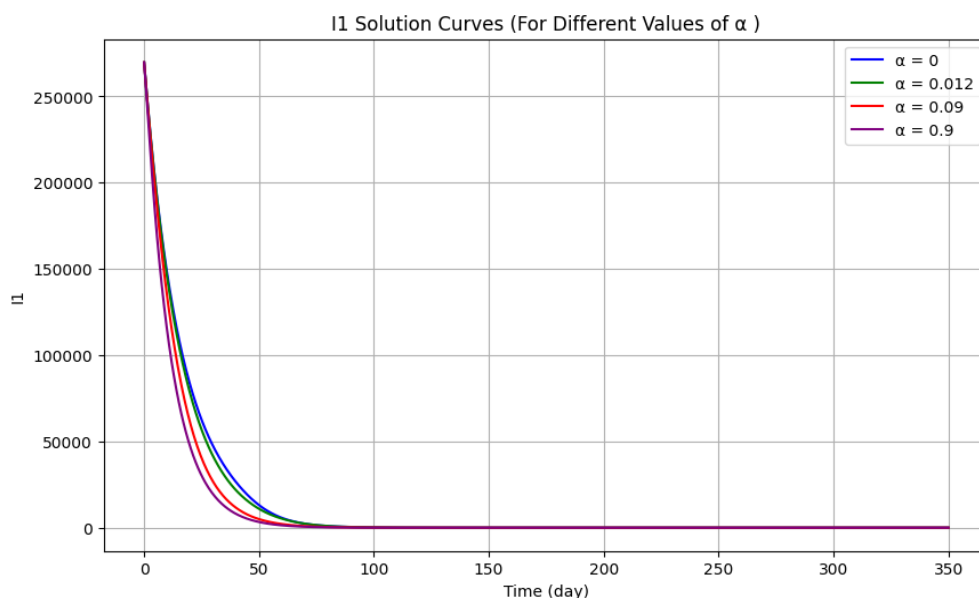

Figure 8.3: The spread dynamics of the original virus for different values of α (vaccination rate of susceptible individuals)

Simulation 2. Here, we discuss the graphical representations of the behavior of the compartments infected with the original virus I_1 and those infected with the mutant virus I_2 for different values of the vaccination rate parameter (α), along with an analysis of their impact on the epidemic.

Figure 8.3 illustrates the temporal variation of I_1 for different values of the vaccination rate parameter α. This graph clearly demonstrates the impact of vaccination on the reduction of individuals infected with the original virus over time. The higher the vaccination rate, the more rapidly individuals infected with the original virus are removed from the system. This highlights the significant role of vaccination in public health and its effectiveness in controlling the infection. All curves in the graph start with a high number of infected individuals and decrease

over time. In each case, the number of infected individuals approaches zero around day 100. This indicates that the infected individuals are either recovering or dying, thereby no longer remaining in the system.
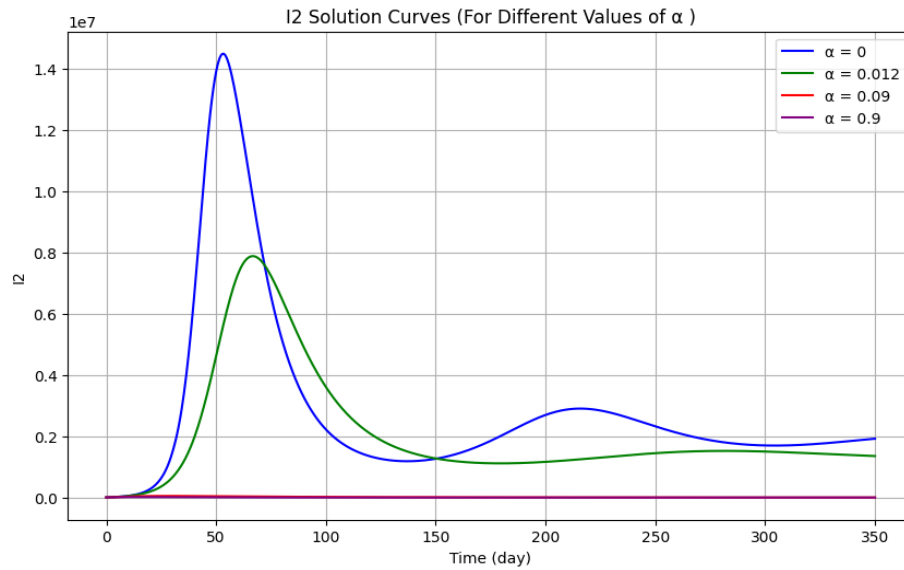
Figure 8.4: The spread dynamics of the mutant virus for different values of α (vaccination rate of susceptible individuals).

At $\alpha = 0$, the number of individuals infected with the original virus shows a slower decline without vaccination and diverges somewhat from the other curves in the graph. This indicates that, in the scenario where vaccination is not implemented, individuals infected with the original virus remain in the system for a longer period. At $\alpha = 0.012$, á $= 0.09$ and $\alpha = 0.9$, the three curves remain closely aligned, indicating that as the vaccination rate increases, the number of individuals infected with the original virus declines more rapidly. High vaccination rates, such as $\alpha = 0.9$, lead to the fastest removal of individuals infected with the original virus from the system. However, even low and moderate vaccination rates contribute effectively to the reduction in the number of infected individuals.
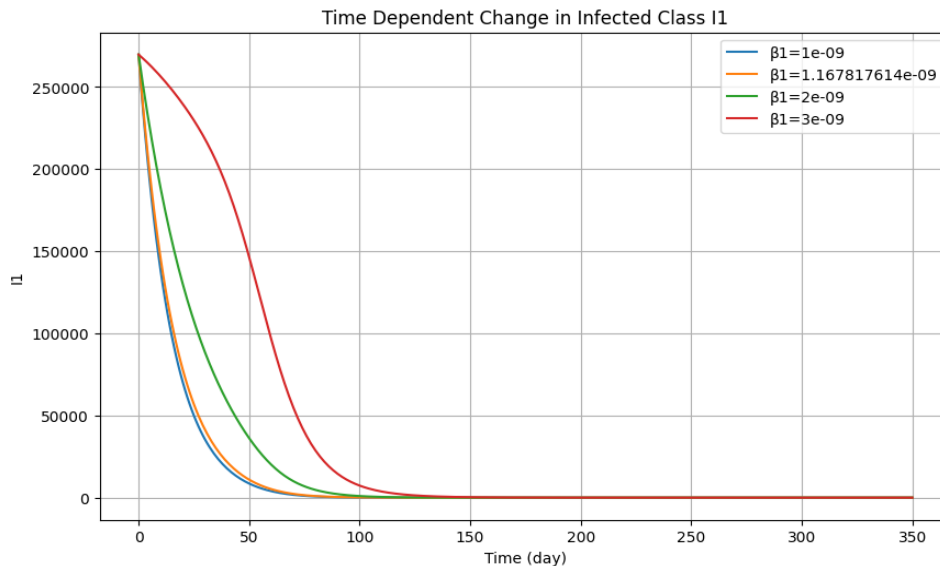
Figure 8.5: The spread dynamics of the original virus for different values of β_1 (transmission rate of the original virus)

The Figure 8.4 illustrates the temporal variation of the I_2 solution curves for different values of α. The horizontal axis represents time (in days), while the vertical axis represents the values of I_2. For $\alpha = 0$, there is an initial rapid increase that peaks around day 50, reaching a peak value of approximately 1.4×10^7. After this peak, there is a rapid decline; however, as time progresses, the decline slows down, and a steady state is observed around day 150. After day 150, a slight increase occurs again, and this fluctuation continues until the end of the graph. For $\alpha = 0.012$, there is an initial rapid increase, but the peak value is lower (around 0.6×10^7) and occurs slightly earlier (around day 50). After the peak, the decline is less steep. Additionally, the fluctuations are less pronounced and have a lower amplitude. For $\alpha = 0.09$,

the curve remains significantly lower compared to the other two curves and continues almost horizontally. This indicates that as the value of α increases, the temporal variation of I_2 decreases substantially, leading to a more stable system. For $\alpha = 0.9$, the curve remains almost at zero and shows no significant increase or decrease over time. This indicates that the system has reached complete equilibrium or remains within a very low range of variation.

In conclusion, the graph illustrates that as the value of α increases, there is a reduction in the temporal variation of I_2 and the system becomes more stable. Low α values (especially $\alpha = 0$) lead to larger amplitude and more fluctuating changes, whereas higher α values enhance the stability of the system and keep the variation at a minimum level.

Simulation 3. In this section, we explored the graphical representations and commentary on the behavior of the compartments infected with the original virus I_1 and the mutant virus I_2 for different values of the transmission rate of the original virus (β_1) and the transmission rate of the mutant virus (β_2), as well as their impact on the epidemic.

In Figure 8.5, the numerical variation of individuals infected with the original virus I_1 over time is examined under different values of the transmission rate β_1. The horizontal axis represents time (in days), while the vertical axis represents I_1, i.e., the number of infected individuals. The graph shows that the number of individuals infected with the original virus will decrease over time, ultimately leading to the end of the outbreak. However, increases in the transmission rate significantly affect the duration and severity of the outbreak. At low transmission rates, the outbreak can be controlled more rapidly, while at high transmission rates, the effects of the outbreak persist longer and affect more individuals.

In the case of $\beta_1 = 0.000000001$, the transmission rate of the virus is extremely low. This results in a rapid initial decline in the number of infected individuals, reaching almost zero in approximately 75 days. This indicates that the outbreak can be quickly controlled at low transmission rates. In the case of $\beta_1 = 0.000000001167817614$, the transmission rate is slightly higher, and the reduction in the number of infected individuals occurs more slowly. By approximately day 100, the number of infected individuals approaches zero. It is observed that as the transmission rate increases, the speed of virus spread also increases. Consequently, controlling the outbreak will take a bit longer in this scenario.

With a value of $\beta_1 = 0.000000002$, the transmission rate leads to a wider spread of the outbreak and causes infected individuals to remain in the system for a longer period. The number of infected individuals continues beyond day 100, and the rate of decrease occurs relatively slowly. In this scenario, the higher transmission rate of the virus indicates that the outbreak will persist longer and affect more individuals. In the scenario with $\beta_1 = 0.000000003$, which has the highest transmission rate, the decline in the number of infected individuals occurs the slowest. The number of infected individuals remains relatively high initially and does not approach zero until approximately day 150. This indicates that in a scenario with a high transmission rate, the outbreak will persist longer, resulting in more individuals remaining infected and making control of the outbreak more challenging.
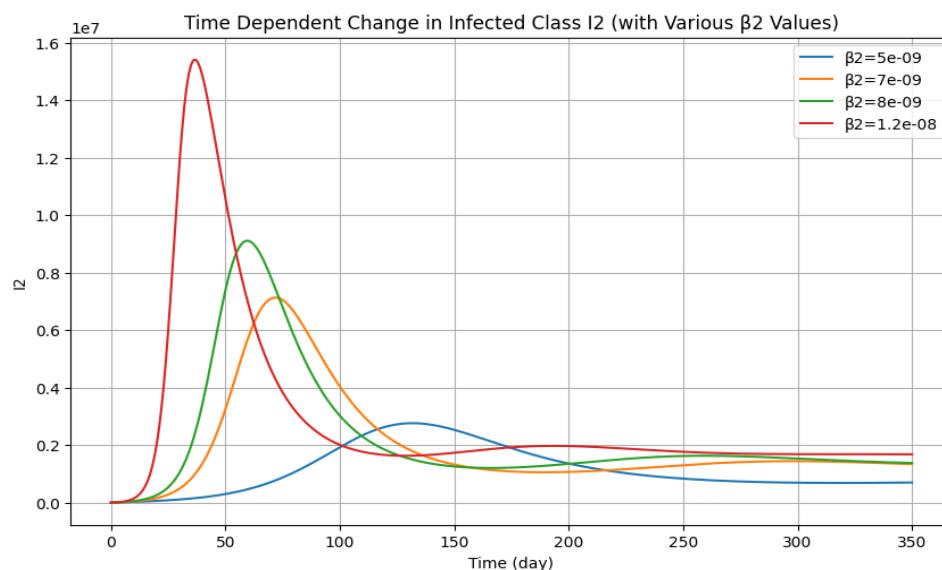
Figure 8.6: The spread dynamics of the mutant virus for different values of β_2 (transmission rate of the mutant virus)

In Figure 8.6, we examined the numerical variation of individuals infected with the mutant virus (I_2) over time under different values of the transmission rate β_2. The horizontal axis represents time (in days), while the vertical axis expresses the number of infected individuals (I_2) on a logarithmic scale. This graph illustrates the spread dynamics of the mutant virus and how variations in the transmission rate affect the course of the outbreak. The graph clearly demonstrates that the increase in the transmission rate of the mutant virus is one of the most critical factors determining the peak, duration, and severity of the outbreak. At lower transmission rates, the outbreak progresses more mildly and lasts longer. However, as the transmission rate increases, the outbreak spreads much more rapidly, the number of infected individuals reaches a higher peak, and there is significant potential to impact a large portion of the population in a short period, thereby placing a heavy burden on healthcare systems.

In the scenario with $\beta_2 = 0.000000005$, the lowest transmission rate, the number of infected individuals shows a very limited increase. It peaks at approximately day 75, with around 0.2×10^7 individuals infected. This transmission rate indicates that the spread of the mutant virus will be milder, resulting in fewer individuals becoming infected. Additionally, the duration of the outbreak is longer compared to other scenarios, as the lower transmission rate spreads the infected individuals over an extended period. At a value of $\beta_2 = 0.000000007$, the

number of infected individuals rises more rapidly, reaching its peak around day 60, with approximately 0.8×10^7 (8 million) individuals infected. This increase in β_2 leads to a more severe wave of the outbreak. The higher number of infected individuals and their shorter duration in the system indicate that the virus will spread quickly, potentially affecting more individuals in a short period. At a value of $\beta_2 = 0.000000008$, the peak number of infected individuals occurs around day 50. In this scenario, the peak value is approximately 1×10^7 (10 million) individuals, further increasing the severity of the outbreak. With this increase, it is observed that infected individuals multiply more rapidly, and the outbreak reaches its peak in a shorter time. The speed of the outbreak's spread, driven by the increase in the transmission rate, results in more individuals becoming infected and places greater strain on healthcare systems.

At a value of $\beta_2 = 0.000000012$, the highest transmission rate, the number of infected individuals increases most rapidly, reaching its peak around day 45. At this transmission rate, it is evident that the mutant virus spreads quickly and affects a large number of individuals. However, after peaking, the decrease in the number of infected individuals is also quite rapid. This indicates that while the virus is highly contagious, a significant portion of the population becomes infected in a short time, leading to a quicker decline of the outbreak.

The following conclusions can be drawn from the simulations: There is a strong relationship between vaccine efficacy and the course of the epidemic. By increasing vaccine efficacy, the likelihood of infected individuals remaining under the impact of the epidemic for a shorter period of time can be increased, and the risk of being exposed to the long-term effects of the epidemic can be reduced. In addition, as the vaccination rate increases, the spread of the mutant virus decreases. This highlights the importance of vaccination at the highest possible level.

9. Conclusion

In this study, the deterministic compartmental model we developed to understand the dynamics of COVID-19 infection provides a comprehensive framework for epidemiological analyses. Our model consists of compartments for S (susceptible), V (vaccinated), I_1 (infected with the original virus), I_2 (infected with the mutant virus), and R (recovered), allowing us to examine the spread of the virus in detail. In addition, the model's inclusion of additional parameters of mutation and leaky vaccine gives the model the ability to analyze disease spread in more detail.

The basic reproduction numbers obtained, R_{01} and R_{02}, play a critical role in determining the potential spread of the original and mutant viruses within the population. When R_{01} and R_{02} are less than one, the global asymptotic stability of the disease-free equilibrium indicates that the viruses can be controlled, whereas values greater than one signify the stability of the endemic equilibrium. This suggests that the viruses can sustain their transmission within the community, highlighting the urgent need for public health policy reassessment.

Bifurcation analysis demonstrates the presence of backward bifurcation for the original virus, shedding light on the complexity of epidemiological dynamics and the impact of parameter changes. In particular, increases in transmission rates due to the incomplete protection provided by the vaccine used lead to rapid increases in the number of infected individuals in compartments I_1 and I_2. This increases the risk of more individuals becoming infected as the viruses spread through the community, significantly elevating the burden on health systems. High transmissibility rates not only affect the number of infected individuals but also the speed and duration of disease spread, posing a critical threat to public health.

Furthermore, the results from the sensitivity analysis of the vaccine efficacy (σ) parameter emphasize the importance of vaccination in public health policies. When vaccine efficacy is high, a notable decrease in the number of infected individuals is observed, enabling better control of the outbreak. Conversely, low vaccine efficacy results in infected individuals remaining in the system for longer periods, leading to wider community impact. This highlights the necessity for optimizing vaccination strategies and increasing vaccination rates across the population.

Our study provides a detailed analysis of various parameters (such as vaccine efficacy and transmissibility rates) that affect the course of the COVID-19 pandemic in Turkey. Validation of the model with real data from COVID-19 cases in Türkiye increases the validity of the findings and provides a solid basis for future epidemiological studies.

In conclusion, this work contributes to a better understanding of the dynamics of COVID-19 through the developed model and aids in optimizing public health strategies. Future research should comprehensively investigate the effects of mutant viruses and vaccines, contributing to the development of more effective public health measures. Additionally, testing and updating the model under different scenarios will be a significant step in preparing for future pandemics. Thus, the findings provide critical information for decision-makers in the fight against COVID-19 and illuminate efforts to protect public health.

Appendix A

$$
\begin{aligned}
k_1 &= -d_{11} - d_{22} - d_{33} - d_{44} - d_{55}, \\
k_2 &= d_{11}d_{22} - d_{12}d_{21} - d_{31}d_{13} - d_{14}d_{41} - d_{23}d_{32} - d_{24}d_{42} + d_{44}(d_{11} + d_{22} + d_{33}) - d_{33}(-d_{11} - d_{22}) - d_{55}(-d_{11} - d_{22} - d_{33} - d_{44}), \\
k_3 &= -d_{15}d_{53}d_{31} - d_{15}d_{54}d_{41} - d_{31}(d_{11}d_{13} + d_{12}d_{23}) - d_{32}(d_{21}d_{13} + d_{22}d_{23}) - d_{41}(d_{11}d_{14} + d_{12}d_{24}) - d_{42}(d_{21}d_{14} + d_{22}d_{24}) \\
&\quad - d_{43}(d_{31}d_{14} + d_{32}d_{24}) + (d_{11} + d_{22} + d_{33})(d_{14}d_{41} + d_{24}d_{42}) - d_{33}(d_{11}d_{22} - d_{12}d_{21}) - (d_{13}d_{31} + d_{23}d_{32})(-d_{11} - d_{22}) \\
&\quad + d_{44}(-d_{11}d_{22} + d_{12}d_{21} + d_{13}d_{31} + d_{23}d_{32} + d_{33}(-d_{11} - d_{22})) \\
&\quad - d_{55}(d_{11}d_{22} - d_{12}d_{21} - d_{13}d_{31} - d_{14}d_{41} - d_{23}d_{32} - d_{24}d_{42} + d_{44}(+d_{11} + d_{22} + d_{33}) - d_{33}(-d_{11} - d_{22})),
\end{aligned}
$$

$$
\begin{aligned}
k_4 \;=\; & -d_{53}\left(d_{11}d_{31}d_{15}+d_{21}d_{32}d_{15}+d_{31}d_{15}d_{33}\right)-d_{54}\left(d_{11}d_{41}d_{15}+d_{21}d_{15}d_{42}+d_{31}d_{15}d_{43}-d_{41}d_{15}d_{44}\right)\\
& -d_{41}\left(d_{11}\left(d_{11}d_{14}+d_{12}d_{24}\right)+d_{12}\left(d_{21}d_{14}+d_{22}d_{24}\right)+d_{13}\left(d_{31}d_{14}+d_{32}d_{24}\right)\right)\\
& -d_{42}\left(d_{21}\left(d_{11}d_{14}+d_{12}d_{24}\right)+d_{22}\left(d_{21}d_{14}+d_{22}d_{24}\right)+d_{23}\left(d_{31}d_{14}+d_{32}d_{24}\right)\right)\\
& -d_{43}\left(d_{31}\left(d_{11}d_{14}+d_{12}d_{24}\right)+d_{32}\left(d_{21}d_{14}+d_{22}d_{24}\right)+d_{33}\left(d_{31}d_{14}+d_{32}d_{24}\right)\right)\\
& +\left(d_{11}+d_{22}+d_{33}\right)\left(d_{41}\left(d_{11}d_{14}+d_{12}d_{24}\right)+d_{42}\left(d_{21}d_{14}+d_{22}d_{24}\right)+d_{43}\left(d_{31}d_{14}+d_{32}d_{24}\right)\right)\\
& +\left(d_{14}d_{41}+d_{24}d_{42}\right)\left(-d_{11}d_{22}+d_{12}d_{21}+d_{13}d_{31}+d_{23}d_{32}+d_{33}\left(-d_{11}-d_{22}\right)\right)\\
& +d_{44}\left(d_{31}\left(d_{11}d_{13}+d_{12}d_{23}\right)+d_{32}\left(d_{21}d_{13}+d_{22}d_{23}\right)+d_{33}\left(d_{11}d_{22}-d_{12}d_{21}\right)+\left(d_{13}d_{31}+d_{23}d_{32}\right)\left(-d_{11}-d_{22}\right)\right)\\
& -\left(d_{31}d_{15}d_{53}+d_{41}d_{15}d_{54}\right)\left(-d_{11}-d_{22}-d_{33}-d_{44}\right)\\
& -d_{55}\left(-d_{31}\left(d_{11}d_{13}+d_{12}d_{23}\right)-d_{32}\left(d_{21}d_{13}+d_{22}d_{23}\right)-d_{41}\left(d_{11}d_{14}+d_{12}d_{24}\right)-d_{42}\left(d_{21}d_{14}+d_{22}d_{24}\right)\right.\\
& \left.-d_{43}\left(d_{31}d_{14}+d_{32}d_{24}\right)+\left(d_{11}+d_{22}+d_{33}\right)\left(d_{14}d_{41}+d_{24}d_{42}\right)-d_{33}\left(d_{11}d_{22}-d_{12}d_{21}\right)-\left(d_{13}d_{31}+d_{23}d_{32}\right)\left(-d_{11}-d_{22}\right)\right.\\
& \left.+d_{44}\left(-d_{11}d_{22}+d_{12}d_{21}+d_{13}d_{31}+d_{23}d_{32}+d_{33}\left(-d_{11}-d_{22}\right)\right)\right)
\end{aligned}
$$

Article Information

Author's contributions: The first author developed the mathematical formulation of the model, established the basic differential equation system, and analyzed the dynamic structure of the model in detail. He also conducted studies on determining the model parameters and literature review, and played an active role in designing simulations and interpreting the results. The second author performed stability and bifurcation analyses in the mathematical analysis of the model, provided calculations of the basic reproduction number, and local and global stability analyses. He also contributed to the optimization and sensitivity analyses within the scope of the study and took significant responsibility in the writing and editing processes of the article. Both authors collaborated in the interpretation of the results, comparison with the literature, and preparation of the article in accordance with academic standards.

Artificial intelligence statement: No artificial intelligence tools were used in writing the article.

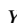**Conflict of Interest Disclosure:** No potential conflict of interest was declared by authors.

Plagiarism Statement: This article was scanned by the plagiarism program.

References

[1] A. B. Gumel, E. A. Iboi, C. N. Ngonghala, et al., *A primer on using mathematics to understand COVID-19 dynamics: Modeling, analysis and simulations*, Infect. Dis. Model., **6** (2021), 148-168. https://doi.org/10.1016/j.idm.2020.11.005

[2] W. O. Kermack, A. G. McKendrick, *A contribution to the mathematical theory of epidemics*, Proc. R. Soc. Lond. A, **115**(772) (1927), 700-721. https://doi.org/10.1098/rspa.1927.0118

[3] T. D. Frank, *COVID-19 interventions in some European countries induced bifurcations stabilizing low death states against high death states: An eigenvalue analysis based on the order parameter concept of synergetics*, Chaos Solitons Fractals, **140** (2020), Article ID 110194. https://doi.org/10.1016/j.chaos.2020.110194

[4] N. Piovella, *Analytical solution of SEIR model describing the free spread of the COVID-19 pandemic*, Chaos Solitons Fractals, **140** (2020), Article ID 110243, 6 pages. https://doi.org/10.1016/j.chaos.2020.110243

[5] A. Din, Y. Li, T. Khan, et al., *Mathematical analysis of spread and control of the novel corona virus (COVID-19) in China*, Chaos Solitons Fractals, **141** (2020), Article ID 110286. https://doi.org/10.1016/j.chaos.2020.110286

[6] A. E. Matouk, *Complex dynamics in susceptible-infected models for COVID-19 with multi-drug resistance*, Chaos Solitons Fractals, **140** (2020), Article ID 110257, 13 pages. https://doi.org/10.1016/j.chaos.2020.110257

[7] H. Bulut, M. Gölgeli, F. M. Atay, *Modelling personal cautiousness during the COVID-19 pandemic: A case study for Turkey and Italy*, Nonlinear Dyn., **105** (2021), 957-969. https://doi.org/10.1007/s11071-021-06320-7

[8] Ö. F. Gözükızıl, N. Köker, *Application of an epidemic model to Turkey data and stability analysis for the COVID-19 pandemic*, Sakarya Univ. J. Sci., **25**(6) (2021), 1438-1445. https://doi.org/10.16984/saufenbilder.980797

[9] S. Boulaaras, R. Ramalingam, A. J. Gnanaprakasam, *SEIR model for COVID-19: Stability of the standard coronavirus factor and control mechanism*, Eur. Phys. J. Spec. Top., **232** (2023), 2485-2495. https://doi.org/10.1140/epjs/s11734-023-00915-4

[10] C. Xu, M. Farman, A. Hasan, et al., *Lyapunov stability and wave analysis of Covid-19 omicron variant of real data with fractional operator*, Alex. Eng. J., **61**(12) (2022), 11787-11802. https://doi.org/10.1016/j.aej.2022.05.025

[11] S. Jamil, M. Farman, A, Akgül, et al., *Fractional order age dependent Covid-19 model: An equilibria and quantitative analysis with modeling*, Results Phys., **53** (2023) Article ID 106928, 17 pages. https://doi.org/10.1016/j.rinp.2023.106928

[12] U. A. P. de León, E. Avila-Vales, K. L. Huang, *Modeling COVID-19 dynamic using a two-strain model with vaccination*, Chaos Solitons Fractals, **157** (2022), Article ID 111927, 17 pages. https://doi.org/10.1016/j.chaos.2022.111927

[13] S. Bugalia, J. P. Tripathi, H. Wang, *Mutations make pandemics worse or better: Modeling SARS-CoV-2 variants and imperfect vaccination*, J. Math. Biol., **88** (2024), Article ID 45, 50 pages. https://doi.org/10.1007/s00285-024-02068-x

[14] Z. Yaagoub, A. Karam, *Global stability of multi-strain SEIR epidemic model with vaccination strategy*, Math. Comput. Appl., **28**(1) (2023), 18 pages. https://doi.org/10.3390/mca28010009

[15] Y. R. Kim, Y. Min, J. N. Okogun-Odompley, *A mathematical model of COVID-19 with multiple variants of the virus under optimal control in Ghana*, Plos One, **19**(7) (2024), Article ID e0303791, 30 pages. https://doi.org/10.1371/journal.pone.0303791

[16] K. Chen, F. Wei, X. Zhang, et al., *Dynamics of an SVEIR transmission model with protection awareness and two strains*, Infect. Dis. Model., **10**(1) (2025), 207-228. https://doi.org/10.1016/j.idm.2024.10.001

[17] A. B. Gumel, *Causes of backward bifurcations in some epidemiological models*, J. Math. Anal. Appl., **395**(1) (2012), 355-365. https://doi.org/10.1016/j.jmaa.2012.04.077

[18] S. I. Rwat, A. A. A. Noor, *Backward bifurcation and hysteresis in a mathematical model of COVID19 with imperfect vaccine*, Matematika, **39**(1) (2023), 87-99. https://doi.org/10.11113/matematika.v39.n1.1458

[19] B. I. Omede, S. A. Jose, J. Anuwat, et al., *Mathematical analysis on the transmission dynamics of delta and omicron variants of COVID-19 in the United States*, Model. Earth Syst. Environ., **10** (2024), 7383-7420. https://doi.org/10.1007/s40808-024-02101-4

[20] H. A. Fatahillah, A. Dipo, *Forward and backward bifurcation analysis from an imperfect vaccine efficacy model with saturated treatment and saturated infection*, Jambura J. Biomathematics, **5**(2) (2024), 132-143. https://doi.org/10.37905/jjbm.v5i2.28810

[21] I. M. Foppa, *A Historical Introduction to Mathematical Modeling of Infectious Diseases: Seminal Papers in Epidemiology*, Academic Press, Amsterdam, 2017.

[22] O. Diekmann, J. A. P. Heesterbeek, J. A. J. Metz, *On the definition and the computation of the basic reproduction ratio R_0 in models for infectious diseases in heterogeneous populations*, J. Math. Biol., **28** (1990), 365-382. https://doi.org/10.1007/BF00178324

[23] M. Martcheva, *An Introduction to Mathematical Epidemiology*, Springer, New York, 2015.

[24] M. Y. Li, *An Introduction to Mathematical Modeling of Infectious Diseases*, Springer Cham, 2018. https://doi.org/10.1007/978-3-319-72122-4

[25] Turkish Statistical Institute, Address-based population registration system results database, (2022). Available at: https://data.tuik.gov.tr/Bulten/Index?p=The-Results-of-Address-Based-Population-Registration-System-2022-49685&dil=2. Accessed September 10, 2024.

[26] Turkish Statistical Institute, Life tables, (2023). Available at: https://data.tuik.gov.tr/Bulten/Index?p=Hayat-Tablolari-2020-2022-49726. Accessed September 2, 2024.

[27] S. Dayan, *COVID-19 ve aşı*, Dicle Med. J., **48**(1) (2021), 98-113. https://doi.org/10.5798/dicletip.1005040

[28] Z. Wang, F. Muecksch, D. Schaefer-Babajew, et al., *Naturally enhanced neutralizing breadth against SARS-CoV-2 one year after infection*, Nature, **595** (2021), 426-431. https://doi.org/10.1038/s41586-021-03696-9

[29] Republic of Türkiye Ministry of Health, COVID-19 information platform database. Available at: https://covid19.saglik.gov.tr/TR-66935/genel-koronavirus-tablosu.html. Accessed August 4, 2024.

[30] A. Saltelli, M. Ratto, T. Andres, et al., *Global Sensitivity Analysis: The Primer*, Wiley, West Sussex, 2008. https://doi.org/10.1002/9780470725184

[31] S. Marino, I. B. Hogue, C. J. Ray, et al., *A methodology for performing global uncertainty and sensitivity analysis in systems biology*, J. Theor. Biol., **254**(1) (2008), 178-196. https://doi.org/10.1016/j.jtbi.2008.04.011

[32] Y. M. Rangkuti, A. L. Firmansyah, *Sensitivity analysis of SEIR epidemic model of COVID-19 spread in Indonesia*, J. Phys. Conf. Ser., **2193** (2022), Article ID 012092, 6 pages. https://doi.org/10.1088/1742-6596/2193/1/012092

Research Article

Geometric Brownian Motion Based on Stochastic Differential Equation Modeling Considering the Change Point Estimation for the Fluctuation of the Turkish Lira Against the US Dollar

Sevda Özdemir Çalıkuşu[1]* , **Fevzi Erdoğan**[2] **and Nihal İnce**[3]

[1]*Department of Accounting and Tax, Ozalp Vocational School, Van Yuzuncu Yil University, Van, Türkiye* ʀᴏʀ
[2]*Department of Econometrics , Faculty of Economics and Administrative Sciences, Van Yuzuncu Yil University, Van, Türkiye* ʀᴏʀ
[3]*Department of Statistics, Faculty of Science, Eskisehir Technical University, Eskisehir, Türkiye* ʀᴏʀ
*Corresponding author

Article Info

Abstract

In this study, the data showing the fluctuation of the Turkish Lira (TL) against the US Dollar (USD) between 19.06.2017 and 19.06.2022 were examined with Geometric Brownian Motion Stochastic Differential Equation Modeling (GBM SDEM). The study aims to get the GBM stochastic differential equation that best fits USD/TL data by considering the change point estimation (CP). Considering CP when working with abruptly changing datasets has a positive effect on the performance of the constructed model. In addition, there may be more than one CP in the dataset, and as the number of CP increases, more suitable models can be obtained for the dataset. The results are supported by graphs that show the proposed SDE model fits the dataset.

1. Introduction

Ordinary differential equations (ODEs) do not account for stochastic influences when modeling dynamic systems. Differential equations become "stochastic differential equations (SDEs)" when random components are added to them, and the stochastic part is referred as "noise". SDEs make it possible to connect probability theory with the older and more complex domains of ordinary and partial differential equations [1]. As a result, stochastic calculus uses concepts from probability theory extensively. An SDE is a differential equation in which one or more elements are stochastic processes, and the solution is a stochastic process as well [2].

Let $\{X_t, t \geq 0\}$ be a one-dimensional diffusion process defined by the Itô SDE

$$dX_t = f(t, X_t, \theta) dt + g(t, X_t, \theta) dW_t \tag{1.1}$$

where W_t is a Brownian Motion (BM). For a solution of (1.1) to exist, in addition to the initial condition X_0, it is anticipated that sufficient regularity conditions are valid for the drift function $f(\cdot)$ and the diffusion coefficient $g(\cdot)$. The functions $f(\cdot)$ and $g(\cdot)$ may or may not depend on t or a statistical parameter $\theta \in \theta \subset \mathbb{R}^d, d \geq 1$ [3].

In modeling the financial market, especially the stock market, the BM is often used to describe the movement of time series variables, and the movement of asset prices in corporate finance plays a vital role in constructing a statistical model [4, 5].

Particularly, one of the most significant concepts in constructing a financial model is the Geometric Brownian Motion (GBM), a special case of the BM process [4]. Considering the definitions above the GBM has the following SDE:

$$dX_t = \theta_1 X_t dt + \theta_2 X_t dW_t, \quad X_0 = x_0 \tag{1.2}$$

and $\theta_2 > 0$. Since solving (1.2) with the initial condition $X_0 = x_0$, where X_t, by applying Itô's lemma the exact solution of (1.2) yields

$$X_t = x_0 e^{\left(\theta_1 - \frac{1}{2}\theta_2^2\right)t + \theta_2 W_t}$$

Here, θ_1 denotes the return that the stock would earn over a brief period and is known as the percentage drift. θ_2 denotes the percentage volatility, which is a stochastic process [3]. Therefore, when taking into account a BM trajectory that represents this differential equation, the right-hand side term $\theta_1 X_t dt$ checks the "trend" of this trajectory whereas the term $\theta_2 X_t dW_t$ checks the "random noise" effect in the trajectory [4, 5]. GBM is a widely used mathematical model for predicting the future price of financial assets, including stocks [6]. So, to help investors in forecasting share prices for a brief period of investment time, a mathematical model as basic as GBM is necessary [7].In this work, instead of models such as Ornstein-Uhlenbeck SDE, Cox-Ingersoll-Ross SDE, and Vasicek SDE used in the literature, the GBM SDE model was preferred. Because, unlike other models, transition probabilities and the exact solution of the GBM SDE can be calculated more easily, so that parameter estimation of the established model can be done with the MLE method [3]. While mean-reverting or stochastic volatility models such as OU, CIR, or Vasicek SDE can capture more complex dynamics, they typically require more intricate calibration procedures and do not offer the same closed-form likelihood expressions [3, 8, 9]. This is important for shorter and easier computer coding.

Furthermore, this study draws methodological inspiration from the YUIMA Project [3], a well-established R framework developed by Iacus, Yoshida, and collaborators, offering validated tools for SDE modeling, including change point analysis [10, 11]. YUIMA provides a reliable foundation for implementing the estimation techniques used in this paper. GBM remains a cornerstone model in modern quantitative finance, supported by extensive literature and robust integration into modeling frameworks such as the YUIMA Project, which we also utilize in this work. Its mathematical simplicity and empirical adaptability further justify its selection in modeling volatile exchange rate contexts.

In recent years, the USD/TRY exchange rate has experienced abrupt fluctuations due to economic and political instabilities. Modeling such stochastic behaviors necessitates techniques that can accommodate sudden structural changes, motivating the use of GBM SDE models with CP.In this study, we consider a change point problem for the fluctuation of a process solution to an SDE when the observations are collected at separate times, where SDE is the equation covering the GBM process.Building on this framework, the study incorporates recent advances in change point detection and estimation. The statistical study of change point detection and estimation has garnered a lot of attention recently. In response to the need for updated and relevant literature on SDE and change point analysis in financial contexts, this study incorporates several recent academic contributions published between 2020 and 2025.Notably, Sun et al. [12] propose a novel interval-based approach for detecting structural shifts and estimating change-points in time series, particularly suited for high-frequency financial data. Their interdisciplinary method integrates elements of signal processing and econometrics, offering strong theoretical support for the CP framework employed in this study. Malinowski [13] focuses on the mathematical well-posedness of symmetric set-valued SDEs under relaxed Lipschitz conditions. This contribution provides foundational backing to the choice of GBM as a tractable and robust model, ensuring analytical consistency in stochastic environments.These works highlight the practical relevance of CP methodologies in volatile markets and validate their use in currency exchange rate modeling, such as the USD/TRY dynamics examined in this paper. Together, these works reinforce the theoretical grounding and methodological relevance of the current study, aligning it with recent advancements in the intersection of stochastic modeling and empirical finance.With this theoretical foundation and updated literature in place, the broader relevance of change point issues across disciplines becomes evident. Basically, change point issues arise in a variety of disciplines, including literature, geology, health, finance, and even everyday life. A change point is a location or a point in time when observations follow one distribution up to that point and a different distribution moving forward in terms of statistics [14].

Chen et al. [15] formed a theory for counting the change points in conditional variance (volatility) of a nonparametric model where the regression and conditional variance functions are unknown. Lee et al. [16] assessed the problem of testing for a parameter change using the CUSUM test based on one-step estimators in diffusion processes. Gregorio and Iacus [17] dealt with a change-point problem for the volatility of a diffusion process observed at discrete times. Iacus and Yoshida [11] dealt with a change-point problem for the volatility of a process solution to a SDE in which observations were gathered at discrete times. They determined the moment the volatility regime changed with the MLE approach that using the approximated likelihood, retroactively. They took into account the CP issue for the drift for continuous time observations of diffusion processes. Oliveira et al. [18] aimed to accomplish three purposes in their article. These include, firstly, identifying change points (regime-switching) in the Brazilian energy spot price time series; secondly, selecting the most appropriate SDE to model Brazilian energy spot prices; and finally, pricing five distinct types of options used to manage electricity price risk in Brazil. In this way, they modeled the Brazilian energy spot prices with the SDE model they obtained by considering the change point. Tonaki et al. [19] treated the change point problem in ergodic diffusion processes from discrete observations. They proposed a technique to predict the change point of the parameter in two cases: one in which the diffusion parameter changes, and the other in which the diffusion parameter does not change but the drift parameter does. They also presented rates of convergence and distributional results of the change point estimators.

Emerging market economies such as Türkiye are those that have not yet completed their capital accumulation. Such economies have structural current account deficits. This situation may cause the upward movements in exchange rates to turn into a systematic risk for the economies of such countries. Therefore, modeling such sharp movements in exchange rates is important for the implementation of effective monetary and financial policies in such countries' economies. So, considering the studies mentioned above, in this study, the data showing the fluctuation of the Turkish Lira (TL) against the US Dollar (USD) between 19.06.2017 and 19.06.2022 were examined by GBM SDE modeling. As a matter of fact, the application of stochastic models to the USD/TL exchange rate in the national literature [20–22] is an interesting subject. However, in this study, unlike other studies, sudden changes in the USD/TL exchange rate were modeled with SDE, considering the CP. For this reason, the study aims to get the GBM SDE that best fits USD/TL data by considering the CP. In this research, Iacus and Yoshida's method, which they conducted in 2012 for CP, was applied [11]. For this purpose, the study was conducted in four steps. In the first step, the GBM SDE model was established without taking into account the CP using the available dataset. Then, the change point estimators of the data were calculated for GBM SDE. Here, only a single CP was accounted for first, and then double CPs were accounted for according to the CP values. The dataset was divided into two and then three regions, respectively, and GBM SDE was re-established for the new regions. In other words, three different GBM SDEs were obtained. In the second step, the parameters of each GBM SDE model were estimated using the MLE method based on the data. In the third step, by applying the Euler-Maruyama (EM) approximation method, the approximate trajectories of the stochastic process, which is the solution of the mentioned SDEs, were acquired for each GBM SDE. Two solutions obtained by taking the mean and median of these trajectories are presented as optimum solutions. In the fourth step, RMSE and MAPE values were calculated for each GBM SDE model. The results were supported by graphs that the proposed SDE model fitted the dataset.

The remainder of this paper is organized as follows: Section 2 describes the material and methodology, including the theoretical background and estimation techniques. Section 3 presents the empirical findings and model results. Section 4 concludes the study with key insights and

implications.

2. Material Method

It is advantageous for the researcher to be able to approximate the solution because it is typically challenging to acquire the exact solution of an SDE. The Euler-Maruyama approximation method (EM), which is based on discretizing the SDE with provided (1.1) on a regular grid of times $t_i = i \cdot \Delta, i = 0, \ldots, n$ where Δ is a given time lag, is a straightforward numerical method that has been utilized in the literature for this purpose. When applied to (1.1), the EM scheme has the form

$$X_{t_{i+1}} = X_{t_i} + f(t_i, X_{t_i}, \theta)\Delta + g(t_i, X_{t_i}, \theta)\Delta W_i, i = 1, \ldots, n-1$$

where $\Delta W_i = W_{t_{i+1}} - W_{t_i} \sim \sqrt{\Delta}N(0,1)$ is the sequence of independent increments of the Wiener process [3]. By using an EM technique, the extreme values of approximation trajectories $X_{t_{1+1}}$ are attained in this study.

When a physical problem is aimed to be modeled with SDE, first of all, it is decided which SDE model to use. Then, before proceeding to solve the proposed SDE, the θ vector of the parameters in equation (1.1) needs to be estimated with the help of the real $N+1$ data points. For this, there are several available methods in the literature such as the maximum likelihood estimation method (MLE), the quasi-maximum likelihood estimation (QMLE) method, the pseudo-maximum likelihood estimation method, the generalized moments method, the Bayesian estimation method, the nonparametric estimation method and so on [3, 9]. In this study, the MLE method has been used to estimate the parameters of the proposed SDE models for the available data, and the QMLE method was used to estimate the change point. For this reason, these two estimation methods were discussed in this section from the real data.

Consider the (1.1) Itô SDE. Given that the observation data of X(t), which is the solution of equation (1.1) is $x_0, x_1, x_2, \ldots, x_N$. Given the $N+1$ observation data in question, the issue at hand is how to estimate the θ vector of the parameters in equation (1.1). For this reason, for a given vector θ, starting from (t_{k-1}, x_{k-1}) the transition probability density function of the point (t_k, x_k) is assumed as $p(t_k, x_k \mid t_{k-1}, x_{k-1}; \theta)$. Suppose the initial probability density is $p_0(x_0 \mid \theta)$. Then, the joint probability density function in the MLE of the vector θ is expressed as

$$D(\theta) = p_0(x_0 \mid \theta) \prod_{k=1}^{N} p(t_k, x_k \mid t_{k-1}, x_{k-1}; \theta). \tag{2.1}$$

In order to estimate the vector θ, it is necessary to maximize the equation (2.1) for θ or avoid small numbers in computer calculations minimize the function $L(\theta) = \ln(D(\theta))$ which is the logarithmic expression of the equation (2.1). In other words, it is necessary to minimize the equation (2.2)

$$L(\theta) = -\ln(p_0(x_0 \mid \theta)) - \sum_{k=1}^{N} \ln(p(t_k, x_k \mid t_{k-1}, x_{k-1}; \theta)). \tag{2.2}$$

Let θ^* be the value θ which minimizes $L(\theta)$ [9]. It is quite difficult to find the optimal θ^* value since equation (2.2) contains a transition probability density function and these transition densities are not generally known for diffusion processes. To eliminate this problem, these transition probabilities must be estimated. For this, when the Euler approach is applied to (2.2), if it is taken into account that the observed values of the X_t process at the time $t = t_{k-1}$ are $X_{t_{k-1}} = x_{k-1}$,

$$X_{t_k} \approx x_{k-1} + f(t_{k-1}, x_{k-1}; \theta)\Delta t + g(t_{k-1}, x_{k-1}; \theta)\sqrt{\Delta t}\eta_k$$

is reached, where $\eta_k \sim N(0,1)$. With $X_{t_i} \sim N(\mu_i, \sigma_i^2)$, the transition probability density function is obtained as

$$p(t_k, x_k \mid t_{k-1}, x_{k-1}; \theta) \approx \frac{1}{\sqrt{2\pi\sigma_k^2}} \exp\left(\frac{-(x_k - \mu_k)^2}{2\sigma_k^2}\right)$$

where $\mu_k = x_{k-1} + f(t_{k-1}, x_{k-1}; \theta)\Delta t$ and $\sigma_k = g(t_{k-1}, x_{k-1}; \theta)\sqrt{\Delta t}$. In this procedure, it is assumed that the transition probability densities approximate the normal distribution using the Euler formula. From here, the θ^* estimator is obtained by minimizing the equation (2.2). In other words, θ^* provides the equality (2.3) [23, 24].

$$\theta^* = \underset{\theta}{\operatorname{argmin}} L(\theta). \tag{2.3}$$

However, it is mostly unknown what the transition probabilities are for the diffusion term in an SDE model. Therefore, developing an estimation technique for equation parameters that does not require previous knowledge of the transition probabilities of the diffusion term is crucial. So, the QMLE method introduced below is designed to accomplish this purpose [25].

Take into account a multidimensional diffusion process

$$dX_t = f(t, X_t; \theta_2)dt + g(t, X_t; \theta_1)dW_t, \quad X_0 = x_0 \tag{2.4}$$

where W is an r-dimensional standard Wiener process independent of the initial variable x_0. Furthermore, $\theta_1 \in \theta_1 \subset \mathbb{R}^p$, $\theta_2 \in \theta_2 \subset \mathbb{R}^q$, $f : \mathbb{R}^d \times \theta_2 \to \mathbb{R}^d$ and $g : \mathbb{R}^d \times \theta_1 \to \mathbb{R}^d \otimes \mathbb{R}^r$. As shown below, given the optimal convergence rates of the estimators for these parameters, the entitling of θ_2 and θ_1 is natural in theory. Given sampled data $X_n = (X_{t_1})_{i=0,\ldots,n}$ with $t_i = i\Delta_n, \Delta_n \to 0$ as $n \to \infty$, for multidimensional diffusions, the QMLE estimator utilizes the following approach of the genuine log-likelihood

$$\ln(X_n; \theta) = -\frac{1}{2}\sum_{i=1}^{n}\left\{\log\det(S_{i-1}(\theta_1)) + \frac{1}{\Delta_n}S_{i-1}^{-1}(\theta_1)\left[(\Delta X_i - \Delta_n f_{i-1}(\theta_2))^{\otimes 2}\right]\right\}$$

where $\theta = (\theta_1, \theta_2), A^{-1}$ the inverse of $A, S = g^{\otimes 2}, A^{\otimes 2} = AA^T, A[B] = \text{tr}(AB)$ and $\Delta X_i = X_{t_{i-1}} - X_{t_i}, S_i(\theta_1) = S(\theta_1; X_{t_i}), f_i(\theta_2) = f(X_{t_1}; \theta_2)$. In this situation, the QMLE of θ is an estimator that provides

$$\hat{\theta} = \underset{\theta}{\text{argmax}} \ln(X_n; \theta)$$

exactly or approximately [3].

When considering the changes in the markets it should be paid attention to the change point analysis. This includes determining the date when stochastic model parameters vary owing to exogenous factors. In this environment, the most significant parameter is the changes in the volatility process in (2.4), i.e., the spread maturity, as in the financial markets in general. In fact, the term drift is typically treated as an ambiguous or offensive term in the statistical model. However, it is probable to estimate consistently if $T \to \infty$ [10, 18, 26]. Take into account a multidimensional SDE of the form

$$dY_t = f(X_t) dt + g(X_t, \theta) dW_t, \quad t \in [0, T]$$

where $\theta \in \theta \subset \mathbb{R}^p, f$ and X_t are multidimensional processes, $g : \mathbb{R}^d \times \theta \to \mathbb{R}^d \otimes \mathbb{R}^r$ is the diffusion coefficient (volatility) matrix and W_t is an r-dimensional Wiener process [3]. Let $\tau^* \in [0, T]$ be the change point in question is not known. Now, it will be determined retrospectively whether, and if so, when a change in the value of the parameter θ has happened, and the parameter θ will be consistently estimated before and after the change point. The following equation formalizes the change point problem for the volatility:

$$Y_t = \begin{cases} Y_0 + \int_0^t f_s ds + \int_0^t g(X_s, \theta_0^*) dW_s & \text{for } t \in [0, \tau^*) \\ Y_{\tau^*} + \int_{\tau^*}^t f_s ds + \int_{\tau^*}^t g(X_s, \theta_1^*) dW_s & \text{for } t \in [\tau^*, T]. \end{cases}$$

Unknown instant change point τ^*, along with θ_0^* and θ_1^*, must be inferred from the observations drawn along the trajectory of (X, Y) [3]. The next expression by Iacus and Yoshida implements how the QMLE technique is used in this work [11]. Let $\Delta_i Y = Y_{t_i} - Y_{t_{i-1}}$ and define

$$\Phi_n(t; \theta_0, \theta_1) = \sum_{i=1}^{\lfloor nt/T \rfloor} G_i(\theta_0) + \sum_{i=[nt/T]+1}^{n} G_i(\theta_1)$$

with

$$G_i(\theta) = \log \det S(X_{t_{i-1}}, \theta) + \Delta_n^{-1}(\Delta_i Y)' S(X_{t_{i-1}}, \theta)^{-1} (\Delta_i Y)$$

and $S = g^{\otimes 2}$. Given that an estimator $\hat{\theta}_k$ is available for each $\theta_k, k = 0, 1$. The definition of $\hat{\theta}_k$ is the same as $\hat{\theta}_k = \theta_k^*$, if θ_k^* are known. The change point estimator of τ^* is [3]

$$\hat{\tau} = \arg \min_{t \in [0, T]} \Phi_n(t; \hat{\theta}_0, \hat{\theta}_1)$$

Choosing the best model among the proposed SDE models for the available data is a result that researchers want to achieve. There are various criteria for this in statistical sciences. Each criterion has its advantages and disadvantages. For this reason, the two most used criteria in the literature are included in this study. These are Mean Absolute Percent Error (MAPE) and Root Mean Square Error (RMSE). For different models or at different times, the MAPE is used to gauge how accurate an estimation is and is calculated with the following formula

$$\text{MAPE} = \frac{1}{n} \left(\sum_{i=1}^{n} \frac{|X_i - Y_i|}{X_i} \right) \cdot 100$$

where n is the number of observations, X_i is the observed values, and Y_i is the predicted values from the model [27]. In numerous statistical research, the RMSE has been employed as a common metric to assess the performance of models. The RMSE is calculated with the following equation

$$\text{RMSE} = \sqrt{\frac{1}{n} \sum_{i=1}^{n} (X_i - Y_i)^2}$$

where n is the number of observations, X_i is the observed values, and Y_i is the predicted values from the model like the MAPE [27].
All stages of model implementation, including the simulation of GBM SDE trajectories, parameter estimation via MLE and QMLE, and change point detection, were carried out in RStudio using version 4.0.5 and the validated functions provided in the 'yuima' package [3, 9].

3. The Research Findings and Discussion

In this study, the data showing the fluctuation of the TL against the USD between 19.06.2017 and 19.06.2022 (see Figure 3.1) were examined by GBM SDEM. This specific time window was selected to capture significant exchange rate instability and potential regime shifts, especially during the Turkish currency crises of 2018 and 2021. The volatility pattern observed in this period strongly motivated the application of change point detection methods within an SDE framework. In contrast, the post-2022 period is characterized by high but stable volatility, which is generally considered suitable for modeling with standard SDEs without explicitly accounting for structural breaks. This period also includes the introduction of financial instruments such as the foreign exchange–linked deposit protection scheme ('KKM') and monetary policy adjustments made amid ongoing macroeconomic pressures. These dynamics influenced exchange rate movements and investor behavior, further justifying the use of structural break detection.The historical exchange rate data used in this study were retrieved from Yahoo Finance [28]. Daily closing prices were used to ensure consistency and alignment with standard financial modeling practices.
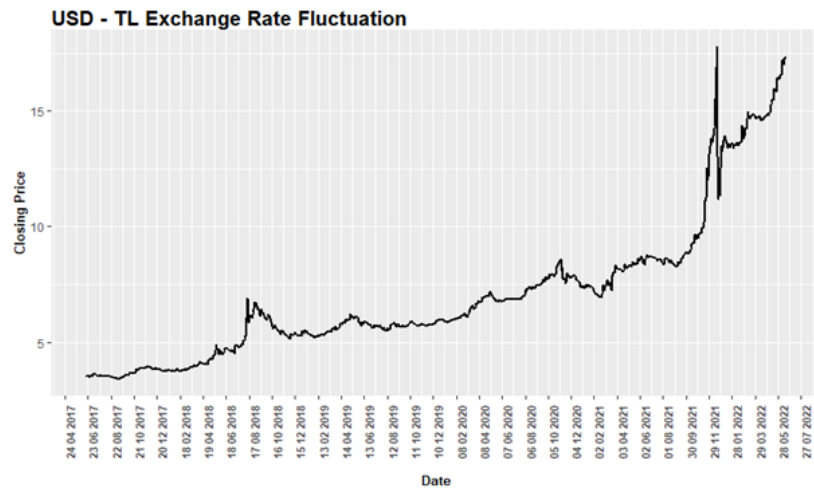
Figure 3.1: The exchange rate fluctuation of USD/TL between 19.06.2017 and 19.06.2022

The study aims to get the GBM SDE that best fits USD/TL data by considering the CP. Before proceeding to the modeling, change point estimators for the GBM SDE of the mentioned data were calculated. The purpose of calculating the change point is to identify the points where the data suddenly changes and find the GBM SDE that best models the data by considering these points. Here, only a single change point was estimated first, and then two change points were estimated. Accordingly, the first CP is $\hat{\tau}_1 = 14.11.2021$, the second CP is $\hat{\tau}_2 = 30.12.2021$. Afterward, according to the determined CP, the dataset was divided into two and then three regions, respectively. The data before and after these CP values were modeled separately with GBM SDE and RMSE and MAPE values were calculated for each model. Among these models, the model that best explained the data was selected according to both criteria. These results were also supported by graphical representation.

First of all, with the help of the USD/TL data, the parameters of the GBM SDE model given by equation (1.2) were estimated as $\tilde{\theta}_1 = 1.5932, \tilde{\theta}_2 = 0.5524$ using the MLE method without considering CP. Accordingly, if the parameters are put in (1.2),

$$dX_t = 1.5932X_tdt + 0.5524X_tdW_t, \quad X_0 = x_0, t \in [0, T] \tag{3.1}$$

was obtained, where $0 = t_0 = 19.06.2017$ and $T = 19.06.2022$. Then, with the number of data $N = 1827$; when the EM schema was applied using N steps, 1000 trajectories of the stochastic process, which is the solution of (3.1) GBM SDE, were obtained as in Figure 3.2. Because the solutions sought for SDEs are random, it is difficult to find a model that directly fits the data. So, the more simulations are performed when searching for EM solutions, the closer the solution will be to the existing dataset. For this reason, in this study, 1000 simulations were made. In order to obtain the optimum solution that fits the dataset, the mean and median of 1000 trajectories mentioned here were taken and these two solutions were presented as possible solutions for (3.1) GBM SDE. The results were given in Figure 3.3; in which the black line represents the dataset, the red line is the mean of the EM trajectories of (3.1) GBM SDE, and the blue line is the median of the EM trajectories of the (3.1) GBM SDE.
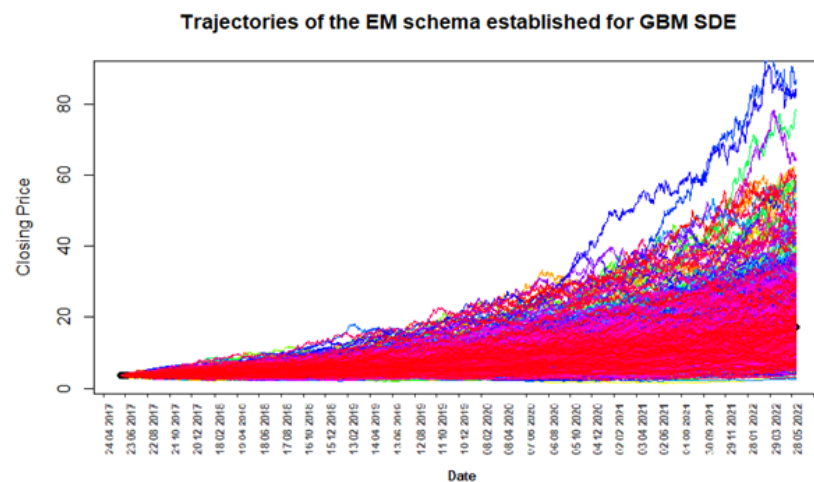
Figure 3.2: Trajectories of the EM schema of (3.1) GBM SDE using N steps

Considering Figure 3.3, the presented optimum solutions cannot reflect the fluctuation in the dataset. Because the dataset contains fluctuations that show sudden changes. For this reason, the change point of the dataset has been estimated according to GBM SDE and this estimate is $\hat{\tau}_1 = 14.11.2021$. Accordingly, this dataset is divided into two regions from the change point $\hat{\tau}_1$. Considering the data before $\hat{\tau}_1$ and after $\hat{\tau}_1$, two different GBM SDE models have been created. For this, the procedures performed in (3.1) GBM SDE modeling have been followed respectively. The MLE of the parameter obtained for GBM SDE, taking into account the $\hat{\tau}_1$ change point, was given in Table 3.1.

Mean and Median of EM Trajectories
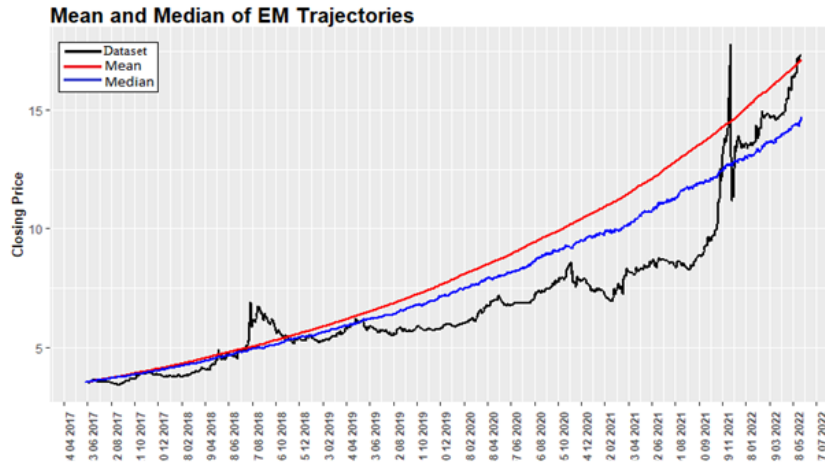
Figure 3.3: Mean and Median of EM Trajectories of (3.1) GBM SDE

	$\tilde{\theta}_1$		$\tilde{\theta}_2$
$t \in [0, \hat{\tau}_1)$	$t \in [\hat{\tau}_1, T]$	$t \in [0, \hat{\tau}_1)$	$t \in [\hat{\tau}_1, T]$
1.0453	0.5499	0.3727	0.4077

Table 3.1: MLE of the parameter obtained for GBM SDE considering the change point $\hat{\tau}_1$

Accordingly, when the initial value at the change point $\hat{\tau}_1$ is considered as the first value at $\hat{\tau}_1$; in other words, since the moment $\widehat{\tau}_1$ corresponds to the 1610th data, the obtained GBM SDE equation is obtained as

$$dX_t = \begin{cases} 1.0453X_t dt + 0.3727X_t dW_t, & X_0 = x_0, & t \in [0, \hat{\tau}_1) \\ 0.5499X_t dt + 0.4077X_t dW_t, & X_0^* = x_{1611}, t \in [\hat{\tau}_1, T] \end{cases} \qquad (3.2)$$

where $0 = t_0 = 19.06.2017$ and $T = 19.06.2022$. Similar to the previous modeling, the number of data in the interval $[0, \hat{\tau}_1)$ is $N_1 = 1610$ and the number of data in the interval $[\hat{\tau}_1, T]$ is $N_2 = 217$ ($N = N_1 + N_2$); using N_1 steps for the interval $[0, \hat{\tau}_1)$ and N_2 steps for the interval $[\hat{\tau}_1, T]$, the 1000 trajectories EM schema of the stochastic process, which is the solution of (3.2) GBM SDE, was obtained as in Figure 3.4 and Figure 3.5, respectively.

Trajectories of the EM schema established for GBM SDE prior to the first CP
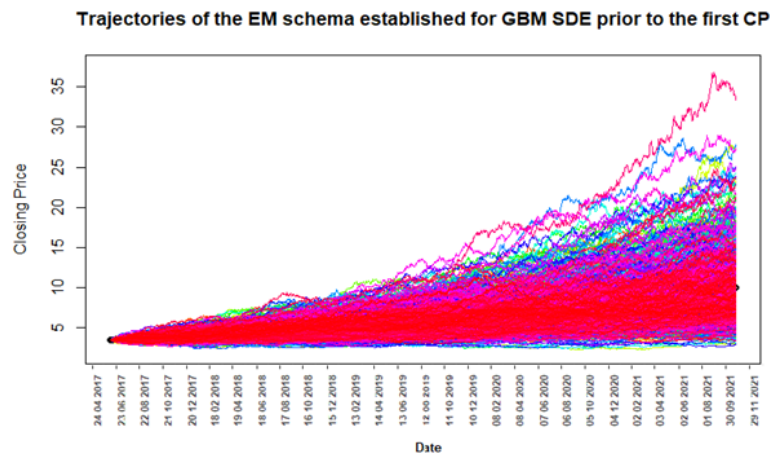
Figure 3.4: Trajectories of the EM schema of (3.2) GBM SDE for $[0, \hat{\tau}_1)$ using N_1 steps

For each interval, the mean and median of the 1000 trajectories specified here were taken by performing similar operations as in finding the optimum solutions of (3.1) GBM SDE, and these two solutions were presented as optimum solutions for (3.2) GBM SDE. The results are given in Figure 3.6 for the interval $[0, \hat{\tau}_1)$ and in Figure 3.7 for the interval $[\hat{\tau}_1, T]$. In each figure, in the regions indicated above, black lines represent the dataset, red lines represent the mean of (3.2) GBM SDE's EM trajectories and blue lines represent the median of (3.2) GBM SDE's EM trajectories. When these solutions are combined, the optimum solution of (3.2) GBM SDE is obtained, which is shown in Figure 3.8; where the black line represents the dataset, the green line the mean of the EM trajectories of (3.1) GBM SDE, the yellow line the median of the EM trajectories of the (3.1) GBM SDE and the pink line the mean of the EM trajectories of (3.2) GBM SDE, the purple line the median of the EM trajectories of the (3.2) GBM SDE. Considering Figure 3.8, it can be said that the optimum solutions proposed for (3.2) GBM SDE are closer to the dataset than the optimum solutions proposed for (3.1) GBM SDE. Thus, with the CP, relatively more suitable GBM SDE EM approximations are obtained for the available dataset. Apart from visually, the closeness of the solutions to the dataset was be given in Table 3.3 by calculating the RMSE and MAPE values.
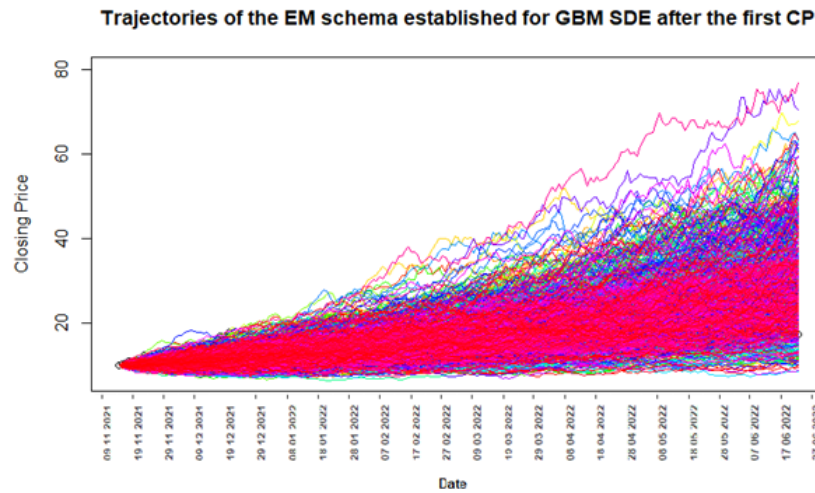
Figure 3.5: Trajectories of the EM schema of (3.2) GBM SDE for $[\hat{\tau}_1, T]$ using N_2 steps
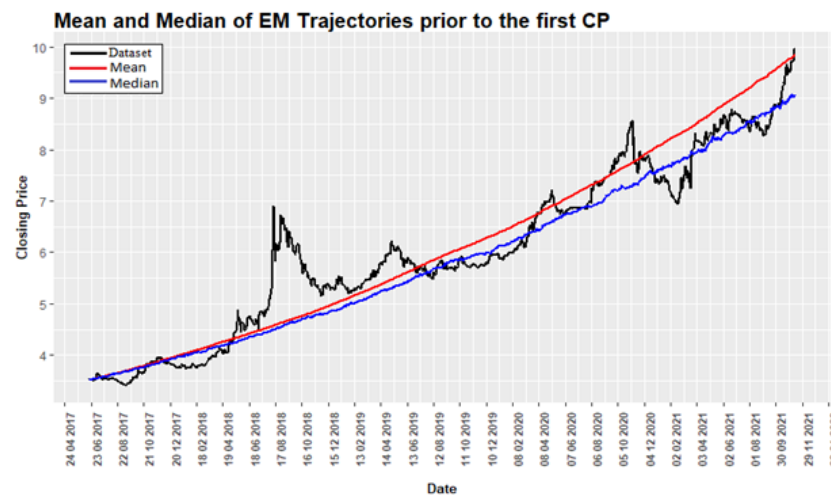
Figure 3.6: Mean and Median of EM Trajectories of (3.2) GBM SDE for $[0, \hat{\tau}_1)$
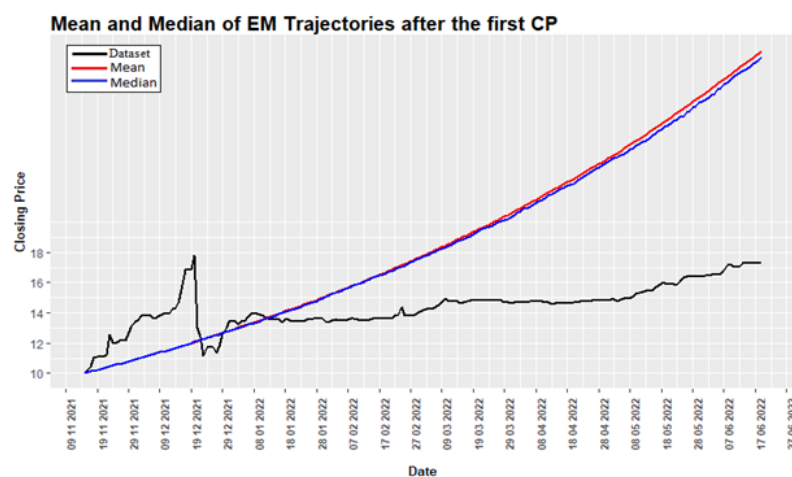
Figure 3.7: Mean and Median of EM Trajectories of (3.2) GBM SDE for $[\hat{\tau}_1, T]$

However, looking at Figure 3.8 it seems that the right tail of the optimum solutions is well above the dataset For this reason, it was deemed appropriate to make one more change point estimation on the dataset in the interval $[\hat{\tau}_1, T]$. Thus, the expression "the first CP (1st CP)" was used for the moment $\hat{\tau}_1$. Therefore, the other change point in the interval $[\hat{\tau}_1, T]$ was expressed as "the second CP (2nd CP)" and denoted by $\hat{\tau}_2$. So, in this interval, the change point of the dataset was estimated according to GBM SDE and this estimate is $\hat{\tau}_2 = 30.12.2021$. Accordingly, the mentioned interval was divided into two regions from the change point $\hat{\tau}_2$. Considering the data from $\hat{\tau}_1$ to $\hat{\tau}_2$ and after $\hat{\tau}_2$, two different GBM SDE models were created. For this, the procedures performed in (3.2) GBM SDE modeling were followed respectively.
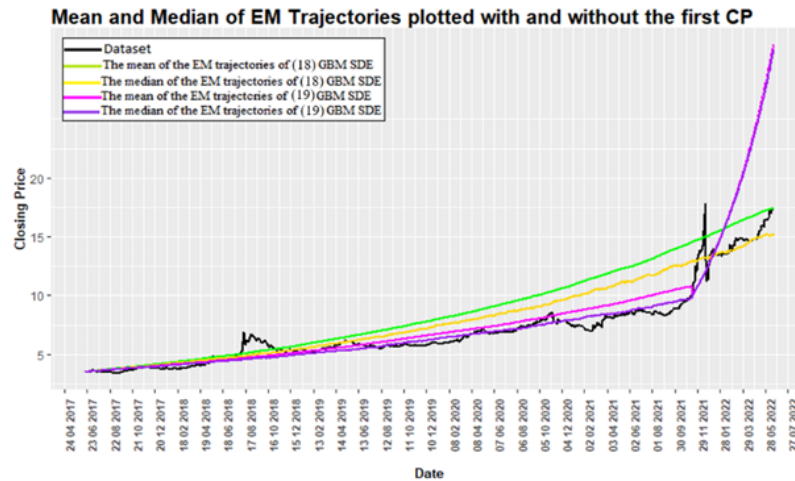
Figure 3.8: Mean and Median of EM Trajectories of (3.2) GBM SDE

The MLE of the parameter obtained for GBM SDE, taking into account the $\hat{\tau}_2$ change point, was given in Table 3.2.

$\tilde{\theta}_1$		$\tilde{\theta}_2$	
$t \in [\hat{\tau}_1, \hat{\tau}_2)$	$t \in [\hat{\tau}_2, T]$	$t \in [\hat{\tau}_1, \hat{\tau}_2)$	$t \in [\hat{\tau}_2, T]$
1.0453	0.2537	0.3727	0.0949

Table 3.2: Estimations of the MLE of the parameter obtained for GBM SDE considering the change point $\hat{\tau}_2$

Accordingly, when the initial value at the change point $\hat{\tau}_2$ is considered as the first value at $\hat{\tau}_2$; in other words, since the moment $\hat{\tau}_2$ corresponds to the 1656th data, the obtained GBM SDE equation is obtained as

$$dX_t = \begin{cases} 1.0453X_t dt + 0.3727X_t dW_t, & X_0 = x_0, \quad t \in [0, \hat{\tau}_1) \\ 1.0453X_t dt + 0.3727X_t dW_t, & X_0{}^* = x_{1611}, t \in [\hat{\tau}_1, \hat{\tau}_2) \\ 0.2537X_t dt + 0.0949X_t dW_t, & X_0{}^{**} = x_{1657}, t \in [\hat{\tau}_2, T] \end{cases} \tag{3.3}$$

where $0 = t_0 = 19.06.2017$ and $T = 19.06.2022$. Here, the number of data in the interval $[\hat{\tau}_1, \hat{\tau}_2]$ is $N_3 = 43$ and the number of data in the interval $[\hat{\tau}_2, T]$ is $N_4 = 171 (N = N_1 + N_3 + N_4)$; using N_3 steps for the interval $[\hat{\tau}_1, \hat{\tau}_2)$ and N_4 steps for the interval $[\hat{\tau}_2, T]$, the 1000 trajectories EM schema of the stochastic process, which is the solution of (3.3) GBM SDE for the interval $[\hat{\tau}_1, T]$, was obtained as in Figure 3.9 and Figure 3.10, respectively. For each interval, the mean and median of the 1000 trajectories specified here were taken by performing similar operations as in finding the optimum solutions of (3.2), and these two solutions are presented as optimum solutions for (3.3) GBM SDE for the interval $[\hat{\tau}_1, T]$. The results were given in Figure 3.11 for the interval $[\hat{\tau}_1, \hat{\tau}_2)$ and in Figure 3.12 for the interval $[\hat{\tau}_2, T]$. In each figure, in the regions indicated above, black lines represent the dataset, red lines represent the mean of (3.3) GBM SDE's EM trajectories and blue lines represent the median of (3.3) GBM SDE's EM trajectories.
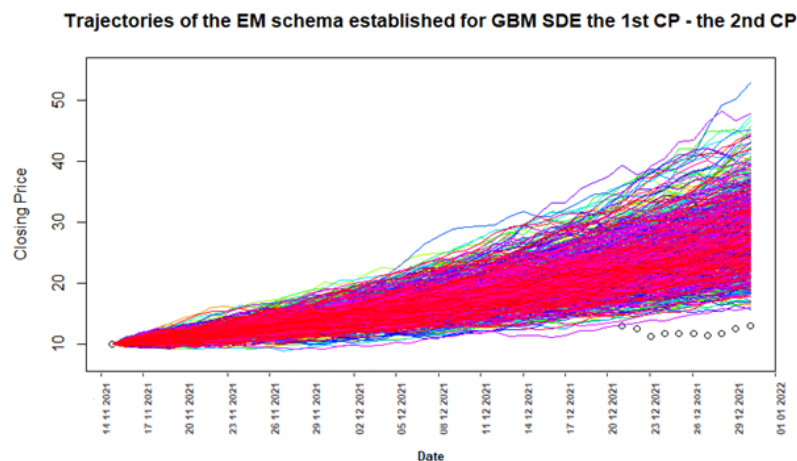
Figure 3.9: Trajectories of the EM schema of (3.3) GBM SDE for t $\in [\hat{\tau}_1, \hat{\tau}_2)$ using N_3 steps

When these solutions and for the interval $[0, \hat{\tau}_1]$ earlier obtained solution are combined, the optimum solution of (3.3) GBM SDE is achieved, which is shown in Figure 3.13; in which the black line represents the dataset, the green line the mean of the EM trajectories of (3.1) GBM SDE, the yellow line the median of the EM trajectories of the (3.1) GBM SDE, the pink line the mean of the EM trajectories of (3.2)

GBM SDE, the purple line the median of the EM trajectories of the (3.2) GBM SDE and the red line the mean of the EM trajectories of (3.3) GBM SDE, the blue line the median of the EM trajectories of the (3.3) GBM SDE. Considering Figure 3.13, it can be said that the optimum solutions proposed for (3.3) GBM SDE are closer to the dataset than the optimum solutions proposed for (3.2) GBM SDE. Thus, GBM SDE EM approaches that are relatively more suitable than others are obtained with double CP for the current dataset. Apart from visually, the closeness of the solutions to the dataset were given in Table 3.3 by calculating the RMSE and MAPE values and the model that best fitted the dataset has been selected accordingly.
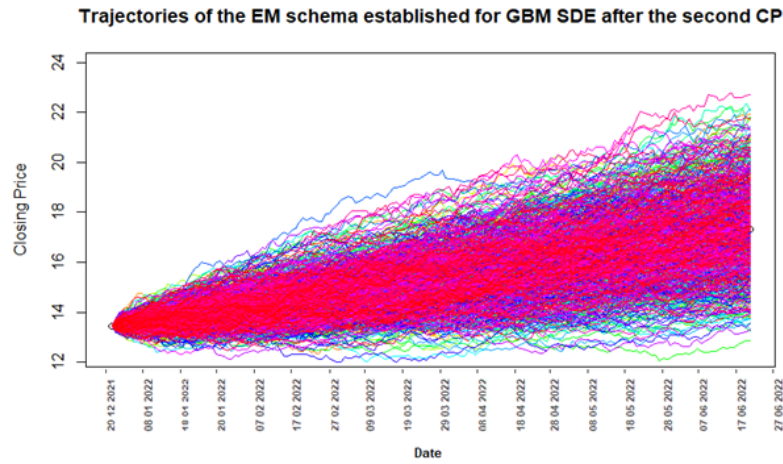
Figure 3.10: Trajectories of the EM schema of (3.3) GBM SDE for $t \in [\hat{\tau}_2, T]$ using N_4 steps
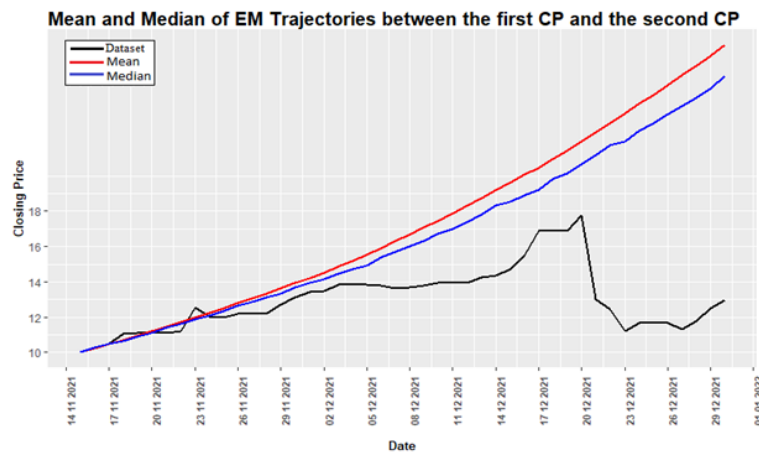
Figure 3.11: Mean and Median of EM Trajectories of (3.3) GBM SDE for $t \in [\hat{\tau}_1, \hat{\tau}_2)$
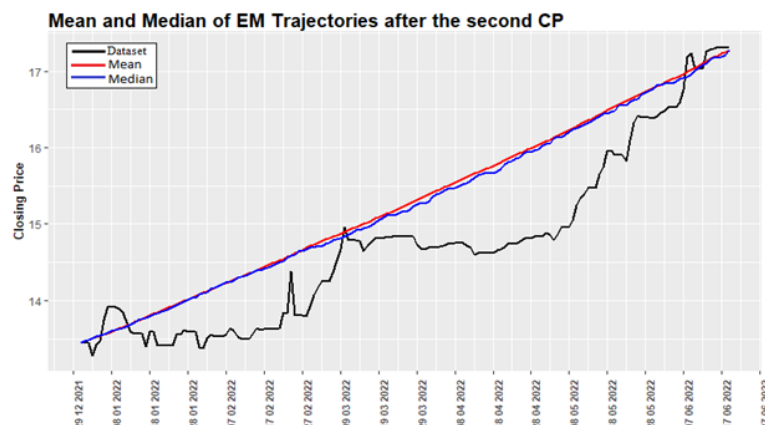
Figure 3.12: Mean and Median of EM Trajectories of (3.3) GBM SDE for $t \in [\hat{\tau}_2, T]$
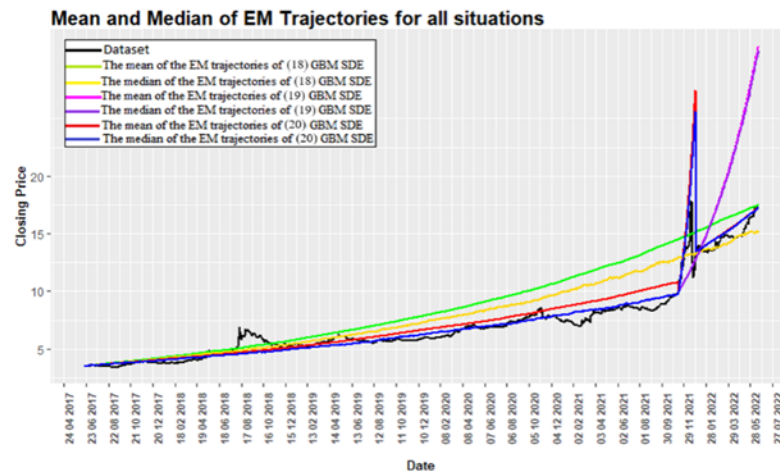
Figure 3.13: Mean and Median of EM Trajectories of (3.3) GBM SDE

Model of GBM SDE	RMSE		MAPE	
	Mean	Median	Mean	Median
(3.1) GBM SDE	2.265709	1.823897	23.42425	15.79356
(3.2) GBM SDE	1.162308	1.560190	8.941137	7.771112
(3.3) GBM SDE	1.598107	**1.018635**	7.066688	**6.129356**

Table 3.3: RMSE and MAPE criteria values of GBM SDE's obtained by considering the CP estimations

Looking at Table 3.3, when each model is evaluated within itself, the models presented by taking the median of the EM approximation solutions among the optimum solutions were chosen as the most appropriate solutions, since they gave smaller values according to both RMSE and MAPE criteria. Among these three models, the median of the EM trajectories of (3.3) GBM SDE with the smallest RMSE value of 1.018635 and the smallest MAPE value of 6.129356 was chosen as the most appropriate model presented for the given dataset. The graph of the proposed model is given in Figure 3.14; where the black line represents the dataset, and the blue line the proposed solution.
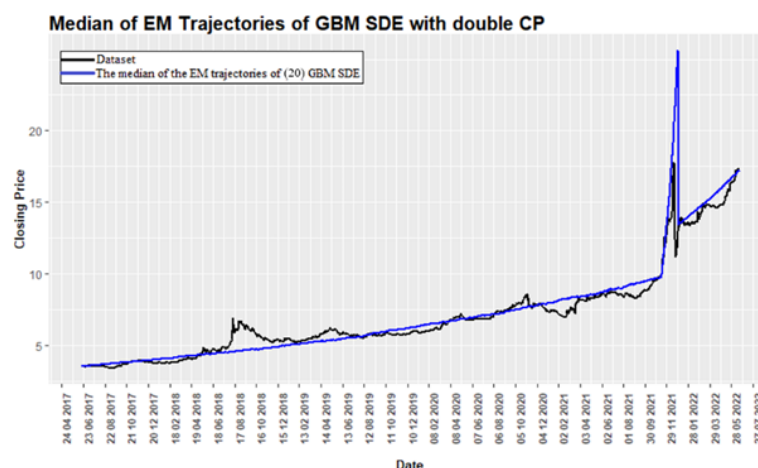
Figure 3.14: The proposed GBM SDE model for USD/TL data

4. Conclusion

In this study, the data showing the fluctuation of the TL against the USD were modeled by GBM SDE by considering the double CP for the first time. With the smallest RMSE and the smallest MAPE values, this solution of SDE has been acquired as the median of the EM trajectories of (3.3) GBM SDE for the given dataset.

Based on these results, when working with abruptly changing datasets, it can be said that considering the CP has a positive effect on the performance of the established model. In other words, the GBM SDE model built with double CP outperforms the GBM SDE model installed without considering the CP. In addition, there may be more than one CP in the dataset, and as the number of CP increases, more suitable models are obtained for the dataset.

Sudden changes in international capital flows can lead to sharp price movements in foreign exchange markets, causing various financial problems in emerging market economies such as Türkiye. For this reason, modeling such sudden changes in exchange rates may have

consequences that may have an impact on market risk management and investment decisions of international investors. The model recommended in this study suggests information that will assist policymakers in implementing effective policies in such areas.

In summary, the main contribution of this research can be outlined as follows:

The primary contribution of this study is the development of a novel modeling approach that integrates GBM with a double CP framework within the SDE setting, implemented using the YUIMA Project. This methodology enables the detection of structural breaks in volatile exchange rate regimes such as USD/TRY, providing a more flexible and accurate alternative to traditional constant-parameter models. The empirical results, based on real market data, demonstrate a significant improvement in model fit and forecasting performance. Furthermore, the use of validated open-source tools ensures transparency, reproducibility, and practical applicability, especially for high-volatility emerging market currencies like the Turkish Lira.

Article Information

Author's Contributions: All authors read and approved the final manuscript. **S.O.C.** developed the main idea of the study, established the methodological framework, introduced the concept of change point estimation, coded the model, performed the analyses, and interpreted the results. **F.E.** contributed to the literature review, supported the selection of the dataset, and assisted in the interpretation of the findings. **N.I.** coded the model, prepared all figures, implemented technical components of the methodology, and provided support in resolving analytical issues during the study.

Artificial Intelligence Statement: Artificial intelligence was used in terms of language proficiency to enhance the quality of the sentences added after the revision.

Conflict of Interest Disclosure: No potential conflict of interest was declared by the authors.

Plagiarism Statement: This article was scanned by the plagiarism program.

References

[1] E. Kostrista, D. Çibuku, *Introduction to stochastic differential equations*, Journal of Natural Sciences and Mathematics of UT, **3**(5-6) (2018), 189-195.

[2] R. Rezaeyan, R. Farnoosh, *Stochastic differential equations and application of the Kalman-Bucy filter in the modeling of RC Circuit*, Appl. Math. Sci., **4**(23) (2010), 1119-1127.

[3] S. M. Iacus, N. Yoshida, *Simulation and Inference for Stochastic Processes with YUIMA: A Comprehensive R Framework for SDEs and Other Stochastic Processes*, Springer, 2018.

[4] Z. Yang, D. Aldous, *Geometric Brownian Motion Model in Financial Market*, University of California, Berkeley, 2015.

[5] K. Reddy, V. Clinton, *Simulating stock prices using geometric Brownian motion: Evidence from Australian companies*, Australas. Account. Bus. Finance J., **10**(3) (2016), 23-47. http://dx.doi.org/10.14453/aabfj.v10i3.3

[6] C. Lausberg, F. Brandt, *Forecasting risk and return of listed real estate: A simulation approach with geometric Brownian motion for the German stock market*, Zeitschrift für Immobilienökonomie, **10** (2024), 1–38. https://doi.org/10.1365/s41056-024-00070-4

[7] S. N. Z. Abidin, M. M. Jaffar, *A review on geometric Brownian motion in forecasting the share prices in Bursa Malaysia*, World Appl. Sci. J., **17**(1) (2012), 82-93.

[8] S. E. Shreve, *Stochastic Calculus for Finance II: Continuous-Time Models*, Springer, 2004.

[9] Y. Aït-Sahalia, *Maximum likelihood estimation of discretely sampled diffusions: A closed-form approximation approach*, Econometrica, **70**(1) (2002), 223–262. https://doi.org/10.1111/1468-0262.00274

[10] S. M. Iacus, *Simulation and Inference for Stochastic Differential Equations: With R Examples*, Springer, New York, 2008. http://dx.doi.org/10.1007/978-0-387-75839-8

[11] S. M. Iacus, N. Yoshida, *Estimation for the change point of volatility in a stochastic differential equation*, Stochastic Process. Appl., **122**(3) (2012), 1068-1092. https://doi.org/10.1016/j.spa.2011.11.005

[12] L. H. Sun, Z. Y. Huang, C. Y. Chiu, et al., *Detecting structural shifts and estimating single change-points in interval-based time series*, Statist. Comput., **35**(127) (2025), Article ID 127. https://doi.org/10.1007/s11222-025-10666-y

[13] M. T. Malinowski, *Financial models and well-posedness properties for symmetric set-valued stochastic differential equations with relaxed Lipschitz condition*, Nonlinear Anal. Real World Appl., **84** (2025), Article ID 104323. https://doi.org/10.1016/j.nonrwa.2025.104323

[14] J. Chen, A. K. Gupta, *Parametric Statistical Change Point Analysis: With Applications to Genetics, Medicine, and Finance*, Birkhäuser, Boston, 2012. http://dx.doi.org/10.1007/978-0-8176-4801-5

[15] G. Chen, Y. Choi, Y. Zhou, *Nonparametric estimation of structural change points in volatility models for time series*, J. Econometrics, **126**(1) (2005), 79-114. https://doi.org/10.1016/j.jeconom.2004.02.008

[16] S. Lee, Y. Nishiyama, N. Yoshida, *Test for parameter change in diffusion processes by cusum statistics based on one-step estimators*, Ann. Inst. Statist. Math., **58** (2006), 211-222. https://doi.org/10.1007/s10463-006-0037-9

[17] A. D. Gregorio, S. M. Iacus, *Least squares volatility change point estimation for partially observed diffusion processes*, Commun. Statist. Theory Methods, **37**(15) (2008), 2342-2357. https://doi.org/10.1080/03610920801919692

[18] A. M. B. de Oliveira, A. Mandal, G. J. Power, *A primer on the pricing of electric energy options in Brazil via mean-reverting stochastic processes*, Energy Rep., **5** (2019), 594-601. https://doi.org/10.1016/j.egyr.2019.03.010

[19] Y. Tonaki, Y. Kaino, M. Uchida, *Estimation for change point of discretely observed ergodic diffusion processes*, (2021), arXiv:2102.06871 [math.ST].

[20] O. Buberkoku, *An empirical application of an asymmetric stochastic volatility model to ISE100 index*, Igdir Univ. J. Soc. Sci., **18** (2019), 503-525.

[21] O. Buberkoku, *An empirical application of an asymmetric stochastic volatility model under the generalized hyperbolic skew Student's t-distribution assumption to the Turkish exchange rate market*, Conference: The Journal of Accounting and Finance, **89** (2021), 185-202.

[22] O. Buberkoku, *Modeling Interest Rates, and Forecasting the Yield Curve with Stochastic Interest Rate Models (CIR and Vasicek)*, Izmir J. Econ., **36**(4) (2021), 893-911. https://doi.org/10.24988/ije.807286

[23] E. Allen, *Modeling with Itô Stochastic Differential Equations*, Springer, 2007. https://doi.org/10.1007/978-1-4020-5953-7

[24] N. Ince, *Generalized entropy optimization methods in stochastic differential equation modeling*, Ph.D. Thesis, Eskisehir Technical University, 2021.

[25] F. Su, K. S. Chan, *Quasi-likelihood estimation of a threshold diffusion process*, J. Econom., **189**(2) (2015), 473-484. https://doi.org/10.1016/j.jeconom.2015.03.038

[26] S. M. Iacus, *Option Pricing and Estimation of Financial Models with R*, John Wiley and Sons, 2011. http://dx.doi.org/10.1002/9781119990079

[27] S. Karamolegkos, D. E. Koulouriotis, *Advancing short-term load forecasting with decomposed Fourier ARIMA: A case study on the Greek energy market*, Energy, **325** (2025), Article ID 135854. https://doi.org/10.1016/j.energy.2025.135854

[28] Yahoo Finance, USD/TRY historical exchange rates (June 19, 2017 – June 19, 2022), Available at: https://finance.yahoo.com. Accessed May 18, 2025.

Journal of Mathematical Sciences and Modelling

Research Article

Tumor–Immune Dynamics: A Spatial-Spectral Perspective

Serpil Yılmaz

Department of Computer Engineering, Faculty of Engineering and Architecture, İzmir Katip Çelebi University, İzmir, Türkiye ʀᴏʀ

Abstract

Mathematical modeling of tumor–immune interactions provides valuable insights into the nonlinear dynamics that govern tumor progression and response to treatment. In this study, a deterministic model of the tumor–immune system under chemotherapy is investigated with a focus on spectral entropy and basin of attraction analyses. Spectral entropy is applied to quantify the temporal complexity of system dynamics and to detect transitions between qualitatively distinct behavioral regimes, such as steady states, oscillatory patterns, and potentially chaotic trajectories. Basin of attraction analysis investigates how variations in the initial populations of tumor and immune cells determine the long-term behavior of the system, including tumor elimination, persistent oscillations, or uncontrolled tumor growth. By combining spectral entropy with basin mapping, the framework captures both the temporal irregularity and the sensitivity to initial conditions inherent in tumor–immune dynamics, which may help guide the design and timing of more effective therapeutic interventions.

1. Introduction

The use of mathematical models has become an essential interdisciplinary tool in cancer research, bridging mathematics, biology, and medicine to enhance understanding of cancer initiation, progression, and treatment. These models provide a structured framework for simulating complex biological processes, such as immune system activation and suppression. They also help identify the key factors of tumor behavior, whether it is eliminated, remains dormant, or grows uncontrollably. By adjusting model parameters, researchers can evaluate how treatment timing, dosage, and immune status influence therapeutic outcomes.

A wide range of models has been developed to study tumor–immune interactions. One foundational contribution by Kuznetsov et al. [1] introduced a nonlinear tumor–immune model, using parameter estimation and bifurcation analysis to determine the conditions for tumor elimination or persistence. Subsequent studies expanded these deterministic models [2–6]. Bifurcation analysis has also been used to explore the effects of immune system strength and pulsed therapy on tumor dynamics [7]. To capture the nonlinear and often unpredictable behavior of tumor growth, discrete and chaotic models have been proposed. A discrete map-based model demonstrated that tumor growth can transition between exponential, periodic, and chaotic patterns depending on parameter values [8]. A chaotic differential equation model demonstrated that variations in nutrient levels, such as glucose and oxygen, significantly influence tumor proliferation [9].

Time-delay effects have also been systematically investigated in mathematical oncology [10–13]. These models revealed oscillatory and chaotic behaviors that offer further insights into tumor relapse and immune regulation.

Mathematical modeling has also played a key role in the development of therapeutic strategies involving immunotherapy, chemotherapy, and their combinations [14–16]. Optimal control frameworks have been employed to develop effective treatment strategies, including immunotherapy and dendritic cell vaccination [17–19]. The efficiency of various combined treatments involving chemotherapy and radiotherapy has also been explored through mathematical modeling. These studies have examined how treatment intensity influences tumor dynamics and transitions to chaotic behavior [20–22]. Additionally, models that incorporate immunotherapy have been developed to investigate tumor oscillations and the potential for long-term relapse [23].

Recent advances in tumor–immune modeling include the integration of stochastic effects, spatial heterogeneity, and advanced control techniques. Stochastic models have demonstrated that random environmental fluctuations can significantly influence tumor progression and treatment efficacy [24]. The incorporation of the Allee effect in both deterministic and stochastic frameworks has provided valuable insights

into tumor extinction dynamics [25, 26]. Spatiotemporal models, which capture the spatial distribution and interaction of tumor and immune cells, have provided important insights into glioma control through immunotherapy [27, 28].

Additional efforts have focused on stabilizing chaotic tumor dynamics. A non-feedback control method has been proposed to regulate chaotic tumor behavior [29], while suboptimal dosing strategies have been shown to sustain chaos and delay tumor elimination [30]. Stochastic modeling has revealed that small perturbations can dramatically impact tumor outcomes [31–34]. Additionally, external interventions such as ultrasound and oncotripsy have been explored as potential tools to modulate chaos and enhance treatment effectiveness [35, 36].

The complex interplay between tumor dynamics and the immune response during chemotherapy is inherently nonlinear and highly sensitive to both initial biological conditions and treatment parameters. Accurately characterizing these dynamics is essential for evaluating treatment efficacy and developing optimized therapeutic strategies.

In this study, spectral entropy (SE) is proposed as a diagnostic tool to analyze tumor–immune dynamics from both temporal and spatial perspectives. Spectral entropy quantifies the unpredictability of a time-series signal and is computed as the Shannon entropy of its normalized power spectral density (PSD) [37]. As a measure of temporal complexity, SE values indicate the degree of disorder in the system. Low SE reflects stable, predictable behavior, while high SE indicates irregular or oscillatory dynamics, potentially corresponding to unstable tumor–immune interactions or treatment resistance.

SE has been widely applied across various scientific domains. In biomedical signal processing, it has been used to detect state transitions and anomalies in EEG signals [38]. In speech processing, SE has applications in speaker identification and speech recognition [39–41], while in mechanical systems, it enables early fault detection by identifying subtle changes in vibration patterns [42]. These diverse applications highlight spectral entropy's capability to analyze complex and unpredictable behaviors; however, its application to tumor–immune modeling remains relatively unexplored.

To advance the analysis of tumor–immune interactions, spectral entropy is integrated with basin of attraction analysis to develop a spatial–spectral framework for exploring tumor–immune responses under varying chemotherapy intensities and initial conditions. Basin of attraction analysis reveals the system's long-term behavior by identifying how different initial conditions converge to distinct outcomes, such as tumor elimination, persistent oscillations characterized by recurring tumor growth and immune response, or uncontrolled growth.

Numerical simulations are conducted to assess the sensitivity of spectral entropy to variations in system parameters and initial states. This integrated spatial–spectral approach provides novel insights into the interplay between temporal and spatial dynamics in tumor–immune systems and highlights the potential of spectral entropy as a tool for optimizing chemotherapy strategies.

2. Tumor-Immune Model

In this study, we consider a deterministic model proposed in [20], which extends the model developed in [1] by incorporating an additional term to represent the effects of chemotherapy. This model describes the interactions between immune effector cells and tumor cells.

The system is formulated as the following set of ordinary differential equations:

$$
\begin{aligned}
\dot{x} &= \sigma + \rho \frac{xz}{\eta + z} - \mu xz - \delta x \\
\dot{z} &= \alpha z(1 - \beta z) - xz - \frac{bz}{1 + z}
\end{aligned}
\tag{2.1}
$$

where x represents the population density of immune effector cells, and z denotes the population density of tumor cells. The term $-\frac{bz}{1+z^2}$ describes the effects of chemotherapy, where b represents the maximum efficacy of the drug. The parameter σ represents the natural rate of effector cell production in the tumor environment. The nonlinear term $\rho \frac{xz}{\eta+z}$ models immune stimulation due to tumor antigens, where ρ and η are parameters associated with tumor-specific antigens. The parameter μ characterizes the rate at which tumor cells inactivate effector cells, and δ is the natural death rate of effector cells.

To better illustrate the important characteristics of the quantitative dynamics of tumor cell density, a rescaling $z = y^4$ is applied to the system (2.1), as previously introduced in [31]. In terms of the variables x and y, the system (2.1) can be reformulated as:

$$
\begin{aligned}
\dot{x} &= \sigma + \rho \frac{xy^4}{\eta + y^4} - \mu xy^4 - \delta x \\
\dot{y} &= 0.25 \left(\alpha y(1 - \beta y^4) - xy - \frac{by}{1 + y^4} \right).
\end{aligned}
\tag{2.2}
$$

The parameter values used in this study are based on experimental data and previous modeling efforts presented in [1]:

$$
\sigma = 0.1181, \quad \rho = 1.131, \quad \eta = 20.19, \quad \mu = 0.001, \quad \delta = 0.374 \quad \alpha = 1.636, \quad \beta = 0.002.
\tag{2.3}
$$

The tumor-free equilibrium of the system corresponds to the point $(\bar{x}, \bar{y}) = \left(\frac{\sigma}{\delta}, 0 \right)$. Linearization about this point yields the Jacobian matrix, whose eigenvalues are given by:

$$
\lambda_1 = -\delta, \qquad \lambda_2 = 0.25 \left(\alpha - \frac{\sigma}{\delta} - b \right).
$$

The first eigenvalue λ_1 is always negative, indicating stability in the x-direction. The second eigenvalue λ_2 governs stability in the tumor cell population. In the absence of chemotherapy ($b = 0$), the tumor-free state is stable if the tumor growth rate satisfies $\alpha < \frac{\sigma}{\delta}$. However, when $\alpha > \frac{\sigma}{\delta}$, stability requires a sufficiently large treatment intensity. Specifically, the tumor-free equilibrium is locally asymptotically stable if:

$$
b > b_* = \alpha - \frac{\sigma}{\delta}
\tag{2.4}
$$

where b_* denotes the minimum chemotherapy threshold required to stabilize the tumor-free equilibrium.

As noted in [31], the condition in (2.4) does not guarantee global tumor elimination. Nonlinear systems can exhibit multiple attractors, such as tumor persistence and tumor-free states, with basins of attraction that depend strongly on initial conditions. In such cases, a treatment strategy that is effective for one set of initial conditions may prove ineffective for another.

3. Spectral Entropy

The spectral entropy (SE) of a time series $x(n)$, where $n = 0, 1, 2, \ldots, N-1$, is computed as follows [37]:
The signal is first mean-centered:

$$\tilde{x}(n) = x(n) - \frac{1}{N}\sum_{n=0}^{N-1} x(n)$$

where $\tilde{x}(n)$ denotes the mean-centered signal. The discrete Fourier transform (DFT) of $\tilde{x}(n)$ is computed as

$$X(k) = \sum_{n=0}^{N-1} x(n)e^{-j2\pi nk/N}, \quad k = 0, 1, 2, \ldots, N-1.$$

where $j = \sqrt{-1}$ is the imaginary unit.
The one-sided power spectrum is then obtained by:

$$S(k) = \frac{|X(k)|^2}{N}, \quad k = 0, 1, 2, 3, \ldots, \frac{N}{2} - 1.$$

The total spectral power is defined as

$$S_{\text{total}} = \sum_{k=0}^{\frac{N}{2}-1} S(k)$$

which is used to normalize the power spectrum and form a probability distribution p_k as:

$$p_k = \frac{S(k)}{S_{\text{total}}} = \frac{|X(k)|^2}{\sum_{k=0}^{\frac{N}{2}-1}|X(k)|^2}.$$

The spectral entropy is then computed using Shannon's entropy formula:

$$SE = -\sum_{k=0}^{\frac{N}{2}-1} p_k \ln p_k$$

and normalized spectral entropy is given by:

$$SE(N) = \frac{SE}{\ln\left(\frac{N}{2}\right)}. \tag{3.1}$$

4. Simulation Results

In this section, the dynamical behavior of the tumor–immune model described by Equation (2.2) is investigated using the parameter values specified in Equation (2.3). The influence of the chemotherapy efficacy parameter b on the long-term dynamics is analyzed through the construction of a bifurcation diagram and phase portraits. The impact of initial conditions on the system's long-term behavior is examined using phase portraits, basins of attraction analysis, and spectral entropy (SE).

To construct the bifurcation diagram, the system governed by Equation (2.2) was numerically integrated using the initial conditions $x(0) = 0.5$ and $y(0) = 0.5$. For each value of the chemotherapy efficacy parameter b, the maximum values of the tumor population variable y were recorded and plotted, as shown in Figure 4.1. A total of 50,000 time series data points were used in the computation, with the first 10,000 points discarded to remove the transients.

As the chemotherapy efficacy parameter b is varied, the system exhibits three distinct dynamical regimes, as shown in Figure 4.1:

- For $0 < b < 0.9$, the system settles into a stable equilibrium characterized by a high tumor burden. In this range, the chemotherapy intensity is insufficient to significantly reduce tumor growth, and the immune response fails to control the tumor population effectively.
- For $0.9 < b < b_*$, where $b_* = 1.329$, a pitchfork bifurcation occurs near $b = 0.9$. The system transitions from a steady state to periodic behavior in tumor dynamics, characterized by alternating phases of tumor reduction and regrowth. Such patterns may arise during treatment cycles that provide only temporary control over tumor progression without achieving long-term elimination.
- For $b > b_*$, the tumor population collapses to zero, and the system stabilizes at the tumor-free equilibrium $\left(\frac{\sigma}{\delta}, 0\right)$. In this case, the combined effects of chemotherapy and immune response are sufficient to eliminate the tumor from the system.

Phase portraits of system (2.2) were generated for various values of the chemotherapy efficacy parameter b, using fixed initial conditions $x(0) = 0.5$ and $y(0) = 0.5$, as shown in Figure 4.2. For small values of b, particularly when $b < 0.9$, trajectories converged to a high-tumor steady state. As b approached 0.9, the system transitioned to a limit cycle, indicating periodic oscillations in both tumor and immune cell populations. Biologically, the emergence of such periodic behavior reflects a recurrent pattern of tumor remission and relapse, where the immune system intermittently suppresses tumor progression, followed by tumor regrowth.

To further investigate the role of initial conditions, the system was analyzed at the critical value $b = 0.9$. Four distinct initial conditions were considered, and the corresponding phase trajectories are presented in Figure 4.3. The outcomes showed that the system could evolve toward either a high-tumor steady state or a limit cycle, depending on the initial state. This indicates the presence of multistability in the tumor–immune dynamics, where different long-term behaviors coexist under the same parameter value.
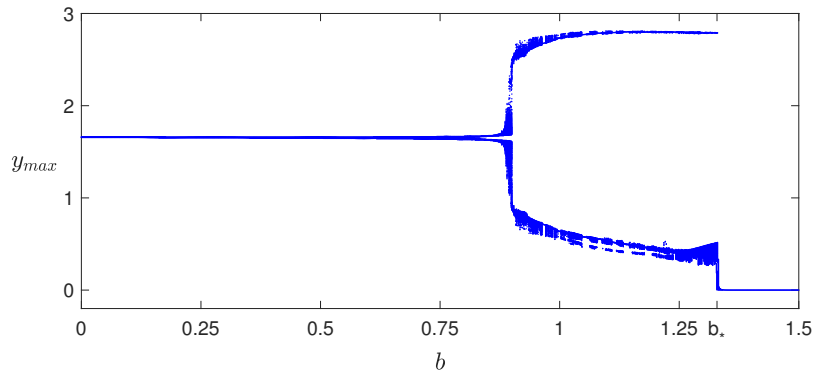
Figure 4.1: Bifurcation diagram of the tumor–immune system with respect to the chemotherapy efficacy parameter b, which represents the maximum effectiveness of the drug. The diagram shows the maximum values of the tumor population variable y as b increases, illustrating changes in the system's behavior. These changes highlight the sensitive dependence of tumor–immune interactions on the value of b.
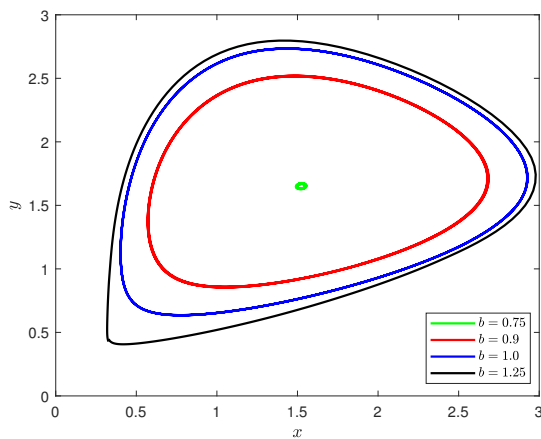
Figure 4.2: Phase portraits of system (2.2) for different values of the chemotherapy parameter b, with initial conditions $x(0) = 0.5$ and $y(0) = 0.5$. The trajectories illustrate the system's response to as b increases from 0.75 to 1.25. Increasing b affects the behavior of tumor–immune oscillations.
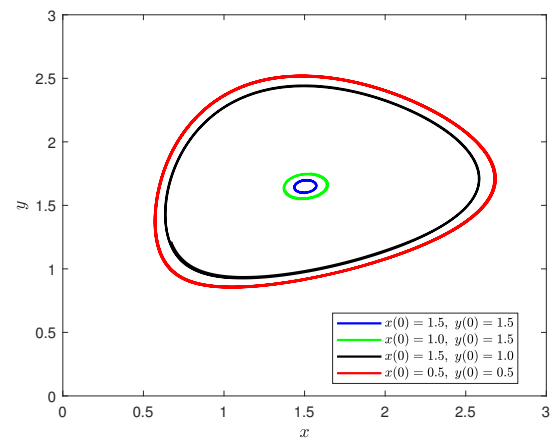
Figure 4.3: Phase portraits of system (2.2) at $b = 0.9$, showing how different initial conditions affect long-term behavior. Each trajectory represents a different initial condition.

The spectral entropy (SE) of the system (2.2) was computed using Equation 3.1 as a function of b, for two different initial conditions: $x(0) = 0.5$, $y(0) = 0.5$ (red curve) and $x(0) = 1.5$, $y(0) = 1.5$ (blue curve), as shown in Figure 4.4. In comparison with the bifurcation diagram presented in Figure 4.1, the SE values remain low for $b < 0.9$, indicating steady-state behavior. A sharp increase in SE is observed near $b = 0.9$, indicating a transition to oscillatory or complex dynamics. For $b > b_* = 1.329$, SE values decrease again, reflecting a return to regular, tumor-free dynamics. The divergence between the red and blue curves highlights the system's sensitivity to initial conditions and demonstrates multistability in the tumor–immune interactions.
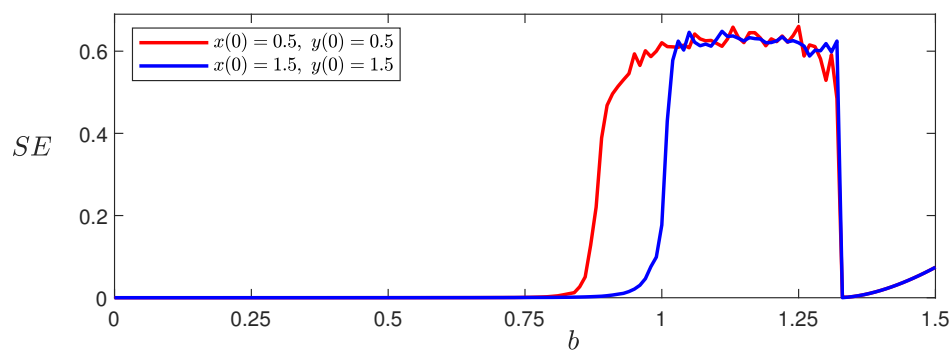
Figure 4.4: Spectral entropy (SE) as a function of the bifurcation parameter b, computed for two initial conditions: $x(0) = 0.5$, $y(0) = 0.5$ (red) and $x(0) = 1.5$, $y(0) = 1.5$ (blue). The SE quantifies the complexity of system dynamics as b varies. A sharp increase in SE indicates a transition to oscillatory or complex behavior. The figure highlights how this transition occurs at different values of b depending on initial conditions, demonstrating multistability in the system.

To examine the sensitivity of long-term dynamics to initial conditions, basins of attraction were computed over the domain $x(0), y(0) \in [0,3]$, using a 400×400 grid with evenly spaced values along each axis. This grid was utilized to explore a wide range of initial conditions and to capture the system's behavior across different regions of its phase space. The analysis was performed at a fixed value of the chemotherapy efficacy parameter b, selected to represent the critical transition period associated with bifurcations in system dynamics.

For each initial condition, the corresponding attractor was identified using a recurrence-based automated classification technique, as described in [43]. This method enables efficient classification of attractors without requiring detailed prior knowledge of the system's dynamics. The resulting classification map is shown in Figure 4.5, where each point represents an initial condition and is colored according to the type of attractor reached over time.

Two primary regions were identified within the state space:

- *Purple Region:* This region corresponds to a stable, steady state characterized by a high tumor burden. Initial conditions within this region lead to tumor persistence with minimal or no reduction. This indicates that chemotherapy is ineffective or the immune response is insufficient.
- *Gray Region:* This region is associated with oscillatory dynamics, where the system exhibits periodic limit cycle behavior. Tumor levels fluctuate between high and low states, reflecting a scenario in which the immune system intermittently suppresses tumor growth but fails to achieve complete elimination.
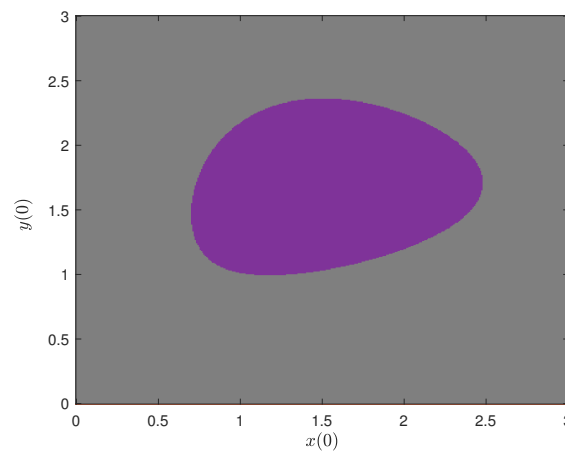
Figure 4.5: Basin of attraction of system (2.2) for initial conditions $x(0), y(0) \in [0,3]$, at a fixed parameter value of b. The purple region corresponds to trajectories converging to a stable steady state with high tumor burden, while the gray region represents initial conditions that lead to oscillatory dynamics associated with a limit cycle. The figure illustrates the coexistence of distinct long-term behaviors and shows that outcomes depend sensitively on initial conditions.

The basins of attraction shown in Figure 4.5 reveal sharply defined boundaries between dynamic regimes. This indicates high sensitivity to initial conditions. Even small changes in the initial tumor–immune states can lead to significantly different long-term behaviors. The presence of distinct attractor regions confirms that the system is multistable, which means that different therapeutic outcomes can occur depending on the initial tumor–immune conditions.

To further investigate the dynamical complexity within these regions, spectral entropy was computed for each trajectory across the grid of initial conditions. SE quantifies the unpredictability and complexity of the system's temporal behavior. Figure 4.6 presents the SE values over the same domain $x(0), y(0) \in [0,3]$, with each point corresponding to the SE value of a specific initial condition.
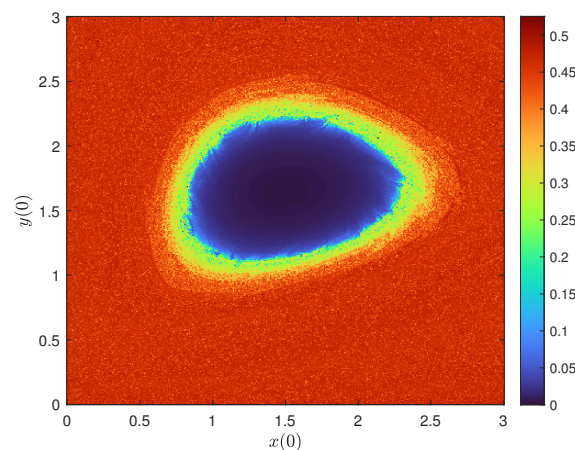
Figure 4.6: Spectral entropy of system (2.2) evaluated over the domain $x(0), y(0) \in [0,3]$ for a fixed value of b. Colors indicate the SE values, with dark blue representing regular (low-complexity) dynamics and red representing complex or chaotic oscillatory behavior. This figure provides a phase space map of dynamical complexity, illustrating how different initial conditions lead to qualitatively distinct temporal patterns in terms of entropy.

Low SE values, shown in dark blue in Figure 4.6, correspond to stable high-tumor states. These points predominantly appear within the purple region of the basin of attraction plot in Figure 4.5, where the system converges to a steady equilibrium with a persistently high tumor burden. Conversely, higher SE values, shown in warmer colors such as yellow and red, indicate more complex or oscillatory behavior. These values occur in the gray region of the basins of attraction in Figure 4.5, associated with limit cycle dynamics where tumor and immune cell populations fluctuate over time.

The SE map complements the basin of attraction diagram by revealing the degree of dynamical complexity in each region. While the basins of attraction illustrate the long-term outcomes, the SE map highlights areas exhibiting chaotic or complex transient dynamics. Notably, near the boundary between the purple and gray regions, small variations in initial conditions lead to significant changes in the final state, reflected by high SE values. This sensitivity suggests the presence of multiple possible therapeutic outcomes, even with slight differences in initial tumor and immune cell densities.

5. Conclusion

This study presented a spatial–spectral framework to analyze tumor–immune dynamics under chemotherapy by integrating basin of attraction mapping with spectral entropy analysis. Basin mapping revealed multistability, which shows that identical treatment parameters can lead to different outcomes depending on the initial tumor-immune conditions. A wider basin corresponding to a desirable state, such as low tumor burden, indicates a more robust therapeutic outcome and improved long-term tumor control. Spectral entropy provided a quantitative measure of temporal complexity and effectively highlighted regime transitions, with high values near bifurcations and along intricate basin boundaries. The combined approach identified regions highly sensitive to both treatment parameters and initial conditions. These findings offer valuable insights to guide the design of more predictable and effective treatment strategies.

Article Information

Acknowledgements: The author would like to express sincere thanks to the editor and the anonymous reviewers for their helpful comments and suggestions.

Artificial Intelligence Statement: No AI tools were used in the preparation of this manuscript.

Conflict of Interest Disclosure: No potential conflict of interest was declared by the author.

Plagiarism Statement: This article was scanned by the plagiarism program.

References

[1] V. A. Kuznetsov, I. A. Makalkin, M. A. Taylor, et al., *Nonlinear dynamics of immunogenic tumors: parameter estimation and global bifurcation analysis*, Bull. Math. Biol., **56**(2) (1994), 295–321. http://dx.doi.org/10.1007/BF02460644

[2] L. G. de Pillis, W. Gu, A. E. Radunskaya, *Mixed immunotherapy and chemotherapy of tumors: Modeling, applications and biological interpretations*, J. Theoret. Biol., **238**(4) (2006), 841–862. https://doi.org/10.1016/j.jtbi.2005.06.037

[3] L. G. De Pillis, A. Radunskaya, *The dynamics of an optimally controlled tumor model: A case study*, Math. Comput. Modelling, **37**(11) (2003), 1221–1244. https://doi.org/10.1016/S0895-7177(03)00133-X

[4] A. d'Onofrio, *A general framework for modeling tumor-immune system competition and immunotherapy: Mathematical analysis and biomedical inferences*, Physica D: Nonlinear Phenom., **208**(3-4) (2005), 220–235. https://doi.org/10.1016/j.physd.2005.06.032

[5] D. Kirschner, J. C. Panetta, *Modeling immunotherapy of the tumor-immune interaction*, J. Math. Biol., **37** (1998), 235–252. https://doi.org/10.1007/s002850050127

[6] V. A. Kuznetsov, G. D. Knott, *Modeling tumor regrowth and immunotherapy*, Math. Comput. Modelling, **33**(12-13) (2001), 1275–1287. https://doi.org/10.1016/S0895-7177(00)00314-9

[7] H. C. Wei, J. T. Lin, *Periodically pulsed immunotherapy in a mathematical model of tumor-immune interaction*, Internat. J. Bifur. Chaos Appl. Sci. Engrg., **23**(04) (2013), Article ID 1350068. https://doi.org/10.1142/S0218127413500685

[8] M. Moghtadaei, M. R. H. Golpayegani, R. Malekzadeh, *Periodic and chaotic dynamics in a map-based model of tumor-immune interaction*, J. Theoret. Biol., **334** (2013), 130–140. https://doi.org/10.1016/j.jtbi.2013.05.031

[9] M. Harney, W. S. Yim, *Chaotic attractors in tumor growth and decay: a differential equation model*, In: P. Vlamos, A. Alexiou (eds) GeNeDis 2014, Adv. Exp. Med. Biol., **820** (2014), Springer, Cham, 193–206. https://doi.org/10.1007/978-3-319-09012-2_13

[10] D. Ghosh, S. Khajanchi, S. Mangiarotti, et al., *How tumor growth can be influenced by delayed interactions between cancer cells and the microenvironment?*, BioSystems, **158** (2017), 17-30. https://doi.org/10.1016/j.biosystems.2017.05.001

[11] X. E. Zhao, B. Hu, *The impact of time delay in a tumor model*, Nonlinear Anal.: Real World Appl., **51** (2020), Article ID 103015. https://doi.org/10.1016/j.nonrwa.2019.103015

[12] S. Khajanchi, M. Perc, D. Ghosh, *The influence of time delay in a chaotic cancer model*, Chaos, **28**(10) (2018), Article ID 103101. https://doi.org/10.1063/1.5052496

[13] M. Sardar, S. Khajanchi, S. Biswas, et al., *A mathematical model for tumor-immune competitive system with multiple time delays*, Chaos Solitons Fractals, **179** (2024), Article ID 114397. https://doi.org/10.1016/j.chaos.2023.114397

[14] J. Yang, S. Tang, R. A. Cheke, *Modelling pulsed immunotherapy of tumour-immune interaction*, Math. Comput. Simulation, **109** (2015), 92–112. https://doi.org/10.1016/j.matcom.2014.09.001

[15] P. Das, S. Das, P. Das, et al., *Optimal control strategy for cancer remission using combinatorial therapy: A mathematical model-based approach*, Chaos Solitons Fractals, **145** (2021), Article ID 110789. https://doi.org/10.1016/j.chaos.2021.110789

[16] C. Letellier, S. K. Sasmal, C. Draghi, et al., *A chemotherapy combined with an anti-angiogenic drug applied to a cancer model including angiogenesis*, Chaos Solitons Fractals, **99** (2017), 297-311. https://doi.org/10.1016/j.chaos.2017.04.013

[17] M. Sardar, S. Biswas, S. Khajanchi, *Modeling the dynamics of mixed immunotherapy and chemotherapy for the treatment of immunogenic tumor*, Eur. Phys. J. Plus, **139**(3) (2024), 1-26, Article ID 228. https://doi.org/10.1140/epjp/s13360-024-05004-6

[18] M. Sardar, S. Khajanchi, B. Ahmad, *A tumor–immune interaction model with the effect of impulse therapy*, Commun. Nonlinear Sci. Numer. Simul., **126** (2023), Article ID 107430. https://doi.org/10.1016/j.cnsns.2023.107430

[19] S. Khajanchi, J. Mondal, P. K. Tiwari, *Optimal treatment strategies using dendritic cell vaccination for a tumor model with parameter identifiability*, J. Biol. Syst., **31**(02) (2023), 487-516. https://doi.org/10.1142/S0218339023500171

[20] I. Bashkirtseva, A. Chukhareva, L. Ryashko, *Modeling and analysis of nonlinear tumor-immune interaction under chemotherapy and radiotherapy*, Math. Methods Appl. Sci., **45**(13) (2022), 7983–7991. https://doi.org/10.1002/mma.7706

[21] I. Bashkirtseva, L. Ryashko, A. G. López, et al., *The effect of time ordering and concurrency in a mathematical model of chemoradiotherapy*, Commun. Nonlinear Sci. Numer. Simul., **96** (2021), Article ID 105693. https://doi.org/10.1016/j.cnsns.2021.105693

[22] I. Bashkirtseva, L. Ryashko, J. M. Seoane, et al., *Chaotic transitions in a tumor-immune model under chemotherapy treatment*, Commun. Nonlinear Sci. Numer. Simul., **132** (2024), Article ID 107946. https://doi.org/10.1016/j.cnsns.2024.107946

[23] G. Torres Espino, C. Vidal, *Dynamics aspects and bifurcations of a tumor-immune system interaction under stationary immunotherapy*, Math. Biosci., **369** (2024), Article ID 109145. https://doi.org/10.1016/j.mbs.2024.109145

[24] M. Sardar, S. Khajanchi, S. Biswas, *Stochastic dynamics of a nonlinear tumor-immune competitive system*, Nonlinear Dyn., **113** (2025), 4395-4423. https://doi.org/10.1007/s11071-024-09768-5

[25] S. Khajanchi, M. Sardar, J. J. Nieto, *Application of non-singular kernel in a tumor model with strong Allee effect*, Differ. Equ. Dyn. Syst., **31**(3) (2023), 687-692. https://doi.org/10.1007/s12591-022-00622-x

[26] M. Sardar, S. Khajanchi, *Is the Allee effect relevant to stochastic cancer model?*, J. Appl. Math. Comput., **68** (2022), 2293-2315. https://doi.org/10.1007/s12190-021-01618-6

[27] S. Khajanchi, J. J. Nieto, *Spatiotemporal dynamics of a glioma immune interaction model*, Sci. Rep., **11** (2021), Article ID 22385. https://doi.org/10.1038/s41598-021-00985-1

[28] S. Khajanchi, *The impact of immunotherapy on a glioma immune interaction model*, Chaos Solitons Fractals, **152** (2021), Article ID 111346. https://doi.org/10.1016/j.chaos.2021.111346

[29] S. Sabarathinam, K. Thamilmaran, *Controlling of chaos in a tumour growth cancer model: An experimental study*, Electron. Lett., **54**(20) (2018), 1160–1162. https://doi.org/10.1049/el.2018.5126

[30] M. Saleem, M. Y. Baba, A. Raheem, et al., *A caution for oncologists: Chemotherapy can cause chaotic dynamics*, Comput. Methods Programs Biomed., **200** (2021), Article ID 105865. https://doi.org/10.1016/j.cmpb.2020.105865

[31] I. Bashkirtseva, A. Chukhareva, L. Ryashko, *Stochastic dynamics of nonlinear tumor–immune system with chemotherapy*, Phys. A: Stat. Mech. Appl., **622** (2023), Article ID 128835. https://doi.org/10.1016/j.physa.2023.128835

[32] I. Bashkirtseva, L. Ryashko, *Analysis of noise-induced phenomena in the nonlinear tumor–immune system*, Phys. A, **549** (2020), Article ID 123923. https://doi.org/10.1016/j.physa.2019.123923

[33] I. Bashkirtseva, L. Ryashko, J. Duarte, et al., *The role of noise in the tumor dynamics under chemotherapy treatment*, Eur. Phys. J. Plus, **136** (2021), 1–13, Article ID 1123. https://doi.org/10.1140/epjp/s13360-021-02061-z

[34] X. Liu, Q. Li, J. Pan, *A deterministic and stochastic model for the system dynamics of tumor-immune responses to chemotherapy*, Phys. A: Stat. Mech. Appl., **500** (2018), 162–176. https://doi.org/10.1016/j.physa.2018.02.118

[35] S. Abernethy, R. J. Gooding, *The importance of chaotic attractors in modelling tumour growth*, Phys. A: Stat. Mech. Appl., **507** (2018), 268–277. https://doi.org/10.1016/j.physa.2018.05.093

[36] S. Yılmaz, *Stabilization of chaos in a cancer model: The effect of oncotripsy*, Balkan J. Electr. Comput. Eng., **10**(2) (2022), 139–149. https://doi.org/10.17694/bajece.1039384

[37] G. Powell, I. Percival, *A spectral entropy method for distinguishing regular and irregular motion of Hamiltonian systems*, J. Phys. A: Math. Gen., **12**(11) (1979), Article ID 2053. https://doi.org/10.1088/0305-4470/12/11/017

[38] H. Helakari, J. Kananen, N. Huotari, et.al, *Spectral entropy indicates electrophysiological and hemodynamic changes in epilepsy*, NeuroImage Clin., **22** (2019), Article ID 101763. https://doi.org/10.1016/j.nicl.2019.101763

[39] F. Luque-Suárez, A. Camarena-Ibarrola, E. Chávez, *Efficient speaker identification using spectral entropy*, Multimed. Tools Appl., **78** (2019), 16803-16815. https://doi.org/10.1007/s11042-018-7035-9

[40] A. M. Toh, R. Togneri, S. Nordholm, *Spectral entropy as speech features for speech recognition*, Proc. PEECS, **1** (2005), Article ID 92.

[41] H. Misra, S. Ikbal, H. Bourlard, et al., *Spectral entropy based feature for robust ASR*, Proc. IEEE Int. Conf. Acoust. Speech Signal Process., **1** (2004), 1–193. https://doi.org/10.1109/ICASSP.2004.1325955

[42] K. Wang, Z. J. Xu, Y. Gong, et al., *Mechanical fault prognosis through spectral analysis of vibration signals*, Algorithms, **15**(3) (2022), Article ID 94. https://doi.org/10.3390/a15030094

[43] G. Datseris, A. Wagemakers, *Effortless estimation of basins of attraction*, Chaos, **32**(2) (2022), Article ID 023104. https://doi.org/10.1063/5.0076568

Research Article

New Form of Newton-Type Inequalities for Multiplicative Conformable Fractional Integrals

Hüseyin Budak[1*] ⬤ **and Büşra Betül Ergün**[2] ⬤

[1]*Department of Mathematics, Faculty of Science and Arts, Kocaeli University, Kocaeli 41001, Türkiye* ʀᴏʀ
[2]*Department of Mathematics, Faculty of Science and Arts, Düzce University, Düzce 81620, Türkiye* ʀᴏʀ
[*]*Corresponding author*

Article Info

Abstract

In this study, a new Newton-type inequality form for multiplicative convex functions is derived using multiplicative conformable fractional integrals. The developed new form presents an inequality that has not been encountered before in literature. To obtain the main results, an essential identity is first introduced, and this identity is combined with multiplicative conformable fractional integrals to create a new Newton-type inequality. This work not only provides a significant contribution to previous research on multiplicative convex functions but also offers a new perspective on the subject. Future research may aim to explore the application of this form to different fractional integral operators or function types.

1. Introduction

Mathematical analysis constitutes one of the most fundamental and comprehensive branches of mathematics, focusing on an in-depth study of the properties of functions such as limits, continuity, differentiation, integration, and convergence. The foundations of this field were laid in the 17th century through the works of Isaac Newton [1] and Gottfried Wilhelm Leibniz [2] on differential and integral calculus. Over time, with contributions from renowned mathematicians such as Augustin-Louis Cauchy [3], Karl Weierstrass [4] and Bernhard Riemann [5], mathematical analysis gained a more rigorous and structured framework. Mathematical analysis encompasses various subfields, including real and complex function analysis, infinite series, differential equations, measure theory, and functional analysis. While classical analysis typically examines functions defined on real and complex numbers, functional analysis deals with infinite-dimensional vector spaces and operators. Additionally, mathematicians working on differentiation and integration have developed more advanced theories, exploring conditions for differentiability and integrability, leading to more general integral definitions such as the Lebesgue integral. Today, mathematical analysis has a wide range of applications in engineering, physics, economics, biology, and data science. For instance, differential equations play a crucial role in modeling physical systems, Fourier analysis is essential in signal and image processing, and probability theory is fundamental in statistics and financial mathematics. Moreover, the rigorous proof methods and theorem demonstrations used in analysis provide a theoretical foundation for other branches of mathematics. Therefore, mathematical analysis holds great significance both in pure mathematics and applied sciences [6, 7].

Newton's inequality is an important mathematical inequality that expresses the relationship between symmetric polynomials. This inequality fundamentally states that lower-degree symmetric means are greater than or equal to higher-degree ones. Newton's inequality holds a significant place in fields such as standard mathematics, analysis and algebra. In addition to helping us understand the properties of symmetric functions, it also allows us to make inferences about the roots of polynomials. Newton's inequality is widely used in mathematical optimization problems, particularly in determining the maximum and minimum values of multivariable functions. [8]. The basic form of the Newton inequality [9] is as follows:

Let $\mathfrak{h} : [\sigma, \delta] \to \mathbb{R}$ be a differentiable function on interval (σ, δ) and $\mathfrak{h}' \in L^1[\sigma, \delta]$. If $|\mathfrak{h}'|$ is a convex function, then the following inequality

holds:

$$\left| \frac{1}{8} \left[\mathfrak{h}(\sigma) + 3\mathfrak{h}\left(\frac{\sigma+2\delta}{3} \right) + 3\mathfrak{h}\left(\frac{2\sigma+\delta}{3} \right) + \mathfrak{h}(\delta) \right] - \frac{1}{\delta-\sigma} \int_\sigma^\delta \mathfrak{h}(t)dt \right| \leq \frac{25(\delta-\sigma)}{576} \left[|\mathfrak{h}'(\sigma)| + |\mathfrak{h}'(\delta)| \right].$$

Newton's inequality has been extended in the literature for various types of fractional integrals, including Riemann-Liouville fractional integrals [10, 11], local-fractional integrals [12], conformable fractional integrals [13, 14], tempered fractional integrals [15], generalized fractional integrals [16]. Additionally, Newton-type inequalities have been studied in the context of different convexity concepts, such as harmonic-convex functions [17], generalized harmonic-convex functions [18]. For more detailed information, please refer to [19–21].

Between 1967 and 1970, Michael Grossman and Robert Katz developed a new calculus system called multiplicative calculus by replacing the subtraction and addition operations of classical calculus with division and multiplication. This system defines derivatives and integrals through division and multiplication and is proposed as an alternative to the traditional calculus, sometimes referred to as alternative or non-Newtonian calculus. While Newton and Leibniz's calculus is based on subtraction and addition operations between numbers, multiplicative calculus replaces these operations with division and multiplication, providing a more suitable approach for modeling continuously changing, growing, or decreasing systems. However, multiplicative calculus has unfortunately not been as widely adopted as the calculus of Newton and Leibniz. The primary reason for this is the lack of sufficient promotion and dissemination of the multiplicative calculus. However, this system perfectly meets all the criteria expected from calculus theories. By working with both positive and negative numbers, multiplicative calculus allows for more precise modeling of complex growth or decline processes, such as economic and financial systems. In situations where traditional calculus encounters limitations, multiplicative calculus has the potential to offer an effective alternative [22, 23].

In multiplicative derivatives, integrals are presented in the work of Bashirov et al. [24]. Very recently, Ali et al. [25] obtained the following Hermite-Hadamard inequality. In addition, using multiplicative calculus, Ali et al. [26] derived the Ostrowski inequality. Furthermore, Chasreechai et al. [27], were the first to obtain the Newton inequality using multiplicative integrals. The basic form of this inequality is as follows:

Let $\mathfrak{h} : [\sigma, \delta] \to \mathbb{R}^+$ be a multiplicatively differentiable function on the interval (σ, δ) and let $\mathfrak{h}^*$ be a multiplicatively integrable function on $[\sigma, \delta]$. If $\mathfrak{h}^*$ is a multiplicatively convex function, then the following inequality holds:

$$\left| \left[\mathfrak{h}(\sigma) \left[\mathfrak{h}\left(\frac{\sigma+2\delta}{3} \right) \right]^3 \left[\mathfrak{h}\left(\frac{2\sigma+\delta}{3} \right) \right]^3 \mathfrak{h}(\delta) \right]^{\frac{1}{8}} \left(\int_\sigma^\delta (\mathfrak{h}(t))^{dt} \right)^{\frac{1}{\sigma-\delta}} \right| \leq (\mathfrak{h}^*(\sigma)\mathfrak{h}^*(\delta))^{\frac{25(\delta-\sigma)}{576}}.$$

In the same paper, the researchers also established Simpson-type inequalities for multiplicative convex functions. In recent years, numerous studies have focused on inequalities related to multiplicative integrals. For instance; Zhan et al. [28] investigated Ostrowski and Simpson-type integral inequalities for multiplicative differentiable functions. Similarly, Meftah et al. [29] formulated the Ostrowski inequality within the context of multiplicative differentiable functions. Boulares et al. [30] introduced a novel fractional identity for such functions, leveraging it to derive new fractional multiplicative Bullen-type inequalities for multiplicatively differentiable convex functions. Moreover, Moumen et al. [31] proposed another fractional identity for multiplicatively differentiable functions and utilized it to establish Simpson-type inequalities for multiplicative convexity. Additionally, by exploring the properties of preinvex and multiplicatively h-preinvex functions, new inequalities involving multiplicative integrals were developed. Furthermore, Özcan [32] proved Hermite-Hadamard type inequalities for multiplicatively h-convex functions and obtained new integral inequalities involving multiplicative integrals for the product and quotient of multiplicatively h-convex and convex positive functions. Kashuri et al. [33] have established generalized multiplicative fractional Hermite-Hadamard type inequalities for both multiplicative convex functions and their products. Additionally, they formulated inequalities related to generalized multiplicative fractional integrals by utilizing a newly derived identity for multiplicative convex functions. Meftah [34] also introduced a new identity in his research, which enabled him to prove Maclaurin-type inequalities for multiplicatively convex functions. Recently, Abdeljawad and Grossman [35] introduced the concept of multiplicative Riemann-Liouville fractional integrals(MRLFI), and later, Budak and Özçelik [36] obtained Hermite-Hadamard type inequalities for these integrals. In another study, Ali [37] proved two fundamental identities for differentiable functions and, based on these, established multiplicative fractional forms of Simpson and Newton's formulas for differentiable multiplicative convex functions. Additionally, Meftah et al. [29] proposed a new fractional identity for multiplicative differentiable functions, which they utilized to obtain fractional Ostrowski-type inequalities for multiplicative convex functions. Du and Long [38] introduced a multivariable fractional integral identity for differentiable functions using MRLFI, and derived a sequence of three-point Newton-Cotes type inequalities from this identity. For further studies in the fields of multiplicative calculus, references [39–43] provide additional insights.

More recently, Budak and Ergün [44] introduced multiplicative conformable fractional integrals(MCFI) and established Hermite-Hadamard type inequalities for these fractional integrals. They also formulated midpoint and trapezoidal inequalities based on these integrals. In this study, we aim to present new Newton-type inequalities associated with MCFI.

This paper investigates the development of a new form of Newton-type inequalities for MCFI. Section 2 reviews the fundamental concepts of multiplicative derivatives and multiplicative integrals, presenting various properties related to these concepts. The basic form of Newton's inequality is then discussed, followed by a comprehensive analysis in the context of multiplicative integrals. Additionally, the definitions of Riemann-Liouville fractional integrals (RLFI) and conformable fractional integrals (CFI) are provided, and Newton's inequalities for these fractional integrals are recalled. In this section, the definitions of MRLFI are give,n and Newton's inequalities for these fractional integrals are presented. Furthermore, the definitions of MCFI are introduced, and various properties of these fractional integrals are discussed. Section 3 presents an identity necessary to derive the main results. Section 4, the aim is to develop a new form of Newton-type inequalities for multiplicatively differentiable and multiplicatively convex functions with the help of MCFI. Moreover we present Netwton type inequalities for functions whose multiplicative derivatives are bounded in Section 5. Finally, in Section 6, the results of the study will be evaluated, and potential avenues for further research will be explored.

2. Preliminaries

In this section we present several definitions and their properties.

2.1. Multiplicative calculus

Proposition 2.1. *[24] If $\mathfrak{h}$ is positive and Riemann integrable on $[\sigma, \delta]$, then $\mathfrak{h}$ is multiplicative integrable on $[\sigma, \delta]$ and*

$$\int_{\sigma}^{\delta} (\mathfrak{h}(x))^{dx} = \exp\left\{\int_{\sigma}^{\delta} \ln(\mathfrak{h}(x))dx\right\}.$$

Proposition 2.2. *[24] Under the condition that the functions $\mathfrak{h}$ and g, being positive, are multiplicative integrable on the interval $[\sigma, \delta]$, it is evident that the properties given below are applicable.*

1. $\int_{\sigma}^{\delta} ((\mathfrak{h}(x))^p)^{dx} = \left(\int_{\sigma}^{\delta}(\mathfrak{h}(x))^{dx}\right)^p$, $p \in \mathbb{R}$,

2. $\int_{\sigma}^{\delta} (\mathfrak{h}(x)g(x))^{dx} = \int_{\sigma}^{\delta}(\mathfrak{h}(x))^{dx} \cdot \int_{\sigma}^{\delta}(g(x))^{dx}$,

3. $\int_{\sigma}^{\delta} \left(\frac{\mathfrak{h}(x)}{g(x)}\right)^{dx} = \frac{\int_{\sigma}^{\delta}(\mathfrak{h}(x))^{dx}}{\int_{\sigma}^{\delta}(g(x))^{dx}}$,

4. $\int_{\sigma}^{\delta}(\mathfrak{h}(x))^{dx} = \int_{\sigma}^{c}(\mathfrak{h}(x))^{dx} \cdot \int_{c}^{\delta}(\mathfrak{h}(x))^{dx}$, $\sigma \leq c \leq \delta$,

5. $\int_{\sigma}^{\sigma}(\mathfrak{h}(x))^{dx} = 1$ *and* $\int_{\sigma}^{\delta}(\mathfrak{h}(x))^{dx} = \left(\int_{\delta}^{\sigma}(\mathfrak{h}(x))^{dx}\right)^{-1}$.

Definition 2.3. *[24] Consider the function $\mathfrak{h} : I \to \mathbb{R}^+$ and assume that its *derivative exists. The notation $\mathfrak{h}^*$ symbolizes multiplicative derivative of $\mathfrak{h}$ (shortly *derivative of the function $\mathfrak{h}$), which is expressed as*

$$\mathfrak{h}^*(x) = \frac{d^*\mathfrak{h}(x)}{dx} = \exp\left\{(\ln\mathfrak{h}(x))'\right\}.$$

Proposition 2.4. *[24] Presuming that the functions $\mathfrak{h}, g : I \to \mathbb{R}^+$ are *differentiable, and the function $\varpi : I \to \mathbb{R}$ is differentiable on I°. If the constant $c > 0$, then the functions $c\mathfrak{h}$, $\mathfrak{h} + g$, $\mathfrak{h}g$, $\frac{\mathfrak{h}}{g}$, $\mathfrak{h}^\varpi$ and $\mathfrak{h} \circ \varpi$ are all *differentiable on I° as well, and the listed below properties holds:*

1. $(c\mathfrak{h})^*(x) = \mathfrak{h}^*(x)$,
2. $(\mathfrak{h} + g)^*(x) = [\mathfrak{h}^*(x)]^{\frac{\mathfrak{h}(x)}{\mathfrak{h}(x)+g(x)}} [g^*(x)]^{\frac{g(x)}{\mathfrak{h}(x)+g(x)}}$,
3. $(\mathfrak{h}g)^*(x) = \mathfrak{h}^*(x)g^*(x)$,
4. $\left(\frac{\mathfrak{h}}{g}\right)^*(x) = \frac{\mathfrak{h}^*(x)}{g^*(x)}$,
5. $\left(\mathfrak{h}^\varpi\right)^*(x) = \mathfrak{h}^*(x)^{\varpi(x)}\mathfrak{h}(x)^{\varpi'(x)}$,
6. $(\mathfrak{h} \circ \varpi)^*(x) = \mathfrak{h}^*(\varpi(x))^{\varpi'(x)}$.

The following theorems give the integral-by-parts formulas for multiplicative integrals, which will be used in the main results.

Theorem 2.5. *[24] Let $\mathfrak{h} : [\sigma, \delta] \to \mathbb{R}$ be multiplicative differentiable and $g : [\sigma, \delta] \to \mathbb{R}$ be differentiable so the $\mathfrak{h}^g$ is multiplicative integrable. Then*

$$\int_{\sigma}^{\delta} \left((\mathfrak{h}^*(x))^{g(x)}\right)^{dx} = \frac{(\mathfrak{h}(\delta))^{g(\delta)}}{(\mathfrak{h}(\sigma))^{g(\sigma)}} \cdot \frac{1}{\int_{\sigma}^{\delta}\left((\mathfrak{h}(x))^{g'(x)}\right)^{dx}}.$$

Theorem 2.6. *[26] Let $\mathfrak{h} : [\sigma, \delta] \to \mathbb{R}$ be multiplicative differentiable, let $g : [\sigma, \delta] \to \mathbb{R}$ and $\varpi : I \subset \mathbb{R} \to [\sigma, \delta]$ be two differentiable functions. Then we have*

$$\int_{\sigma}^{\delta} \left((\mathfrak{h}^*(\varpi(x)))^{g(x)\varpi'(x)}\right)^{dx} = \frac{\mathfrak{h}(\varpi(\delta))^{g(\delta)}}{\mathfrak{h}(\varpi(\sigma))^{g(\sigma)}} \cdot \frac{1}{\int_{\sigma}^{\delta}\left((\mathfrak{h}(\varpi(x)))^{g'(x)}\right)^{dx}}.$$

2.2. Some definitions and several Ostrowski inequalities

Definition 2.7. *[45] A non-empty set K is said to be convex, if for every $\sigma, \delta \in K$ we have*

$$\sigma + t(\delta - \sigma) \in K, \forall t \in [0,1].$$

Definition 2.8. *[45] A function $\mathfrak{h}$ is said to be convex function on the set K, if*

$$\mathfrak{h}(tx + (1-t)y) \leq t\mathfrak{h}(x) + (1-t)\mathfrak{h}(y)$$

for all $\sigma, \delta \in K$ and all $t \in [0,1]$.

Definition 2.9. *[46] A function $\mathfrak{h}$ is said to be log or multiplicatively convex function on set K, if*

$$\mathfrak{h}(t\sigma + (1-t)\delta) \leq [\mathfrak{h}(x)]^t [\mathfrak{h}(y)]^{(1-t)}$$

for all $\sigma, \delta \in K$ and all $t \in [0,1]$.

Remark 2.10. *If a positive function $\mathfrak{h}$ is a multiplicatively convex, then the function $\ln \mathfrak{h}$ is a convex function.*

Theorem 2.11 (Newton Inequality for Multiplicative Integrals). *[27] Let $\mathfrak{h} : [\sigma, \delta] \to \mathbb{R}^+$ be a multiplicatively differentiable function on the interval (σ, δ) and let $\mathfrak{h}^*$ be a multiplicatively integrable function on $[\sigma, \delta]$. If $\mathfrak{h}^*$ is a multiplicatively convex function, then the following inequality holds:*

$$\left| \left[\mathfrak{h}(\sigma) \left[\mathfrak{h}\left(\frac{\sigma + 2\delta}{3} \right) \right]^3 \left[\mathfrak{h}\left(\frac{2\sigma + \delta}{3} \right) \right]^3 \mathfrak{h}(\delta) \right]^{\frac{1}{8}} \left(\int_\sigma^\delta (\mathfrak{h}(t))^{dt} \right)^{\frac{1}{\sigma - \delta}} \right| \leq (\mathfrak{h}^*(\sigma)\mathfrak{h}^*(\delta))^{\frac{25(\delta - \sigma)}{576}} .$$

Definition 2.12. *The Euler Gamma function, Beta function, and Incomplete Beta function are defined by*

$$\Gamma(x) := \int_0^\infty \xi^{x-1} e^{-t} d\xi,$$

$$B(x,y) := \int_0^1 \xi^{x-1}(1-\xi)^{y-1} d\xi,$$

and

$$\mathfrak{B}(x,y,r) := \int_0^r \xi^{x-1}(1-\xi)^{y-1} d\xi,$$

respectively, for $0 < x, y < \infty$ and $r \in [0,1]$.

Definition 2.13. *[47] Let the function $\mathfrak{h} \in L_1([\sigma, \delta])$. For the order $\beta > 0$, the Riemann-Liouville Fractional Integrals (RLFI) $J_{\sigma+}^\beta \mathfrak{h}(x)$ and $J_{\delta-}^\beta \mathfrak{h}(x)$ are defined by*

$$J_{\sigma+}^\beta \mathfrak{h}(x) = \frac{1}{\Gamma(\beta)} \int_\sigma^x (x-t)^{\beta-1} \mathfrak{h}(t) dt, \ x > \sigma$$

and

$$J_{\delta-}^\beta \mathfrak{h}(x) = \frac{1}{\Gamma(\beta)} \int_x^\delta (t-x)^{\beta-1} \mathfrak{h}(t) dt, \ \delta > x$$

respectively. Here Γ represents Euler Gamma function.

Theorem 2.14 (Newton-type İnequality for RLFI). *[10] Let $\mathfrak{h} : [\sigma, \delta] \to \mathbb{R}$ be an absolutely continuous function and let $\mathfrak{h}' \in L^1[\sigma, \delta]$. If $|\mathfrak{h}'|$ is a convex function on the interval $[\sigma, \delta]$, then we obtain the following inequality:*

$$\left| \frac{1}{8} \left[\mathfrak{h}(\sigma) + 3\mathfrak{h}\left(\frac{2\sigma + \delta}{3} \right) + 3\mathfrak{h}\left(\frac{\sigma + 2\delta}{3} \right) + \mathfrak{h}(\delta) \right] - \frac{2^{\beta-1}\Gamma(\beta+1)}{(\delta - \sigma)^\beta} \left[J_{\frac{\sigma+\delta}{2}-}^\beta \mathfrak{h}(\sigma) + J_{\frac{\sigma+\delta}{2}+}^\beta \mathfrak{h}(\delta) \right] \right|$$

$$\leq \frac{\delta - \sigma}{4} (\Omega_1(\beta) + \Omega_2(\beta)) \left[|\mathfrak{h}'(\sigma)| + |\mathfrak{h}'(\delta)| \right].$$

Here,

$$\Omega_1(\beta) = \int_0^{\frac{2}{3}} \left| t^\beta - \frac{1}{4} \right| dt = \begin{cases} \frac{2\beta}{\beta+1} \left(\frac{1}{4} \right)^{1+\frac{1}{\beta}} + \frac{1}{\beta+1} \left(\frac{2}{3} \right)^{\beta+1} - \frac{1}{6}, & 0 < \beta < \frac{\ln\left(\frac{1}{4}\right)}{\ln\left(\frac{2}{3}\right)}, \\ \\ \frac{1}{6} - \frac{1}{\beta+1} \left(\frac{2}{3} \right)^{\beta+1}, & \frac{\ln\left(\frac{1}{4}\right)}{\ln\left(\frac{2}{3}\right)} < \beta \end{cases}$$

and

$$\Omega_2(\beta) = \int_{\frac{2}{3}}^1 \left(1 - t^\beta \right) dt = \frac{1}{3} - \frac{1}{\beta+1} + \frac{1}{\beta+1} \left(\frac{2}{3} \right)^{\beta+1} .$$

Definition 2.15. *[36] The multiplicative left Riemann-Liouville Fractional Integral $\left(_\sigma I_*^\beta \mathfrak{h}\right)(x)$ of order $\beta > 0$ starting from β is defined by*

$$\left(_\sigma I_*^\beta \mathfrak{h}\right)(x) = \exp\left\{(J_{\sigma+}^\beta(\ln \circ \mathfrak{h}))(x)\right\}$$

and the multiplicative right one $\left(_* I_\delta^\beta \mathfrak{h}\right)(x)$ is defined by

$$\left(_* I_\delta^\beta \mathfrak{h}\right)(x) = \exp\left\{(J_{\delta-}^\beta(\ln \circ \mathfrak{h}))(x)\right\}.$$

Theorem 2.16 (Newton Inequality for MRLFI). *[37] Let $\mathfrak{h} : [\sigma, \delta] \to \mathbb{R}^+$ be a multiplicative differentiable function on (σ, δ) and suppose that $\mathfrak{h}^*$ is multiplicatively integrable on $[\sigma, \delta]$. If $\mathfrak{h}^*$ is a multiplicative convex function, then for $v = \left(\frac{1}{8}\right)^{\frac{1}{\beta}}, \xi = \left(\frac{1}{2}\right)^{\frac{1}{\beta}}$ and $\kappa = \left(\frac{7}{8}\right)^{\frac{1}{\beta}}$, the following inequality holds:*

$$\left| \frac{\left[\mathfrak{h}(\sigma)\left[\mathfrak{h}\left(\frac{\sigma+2\delta}{3}\right)\right]^3\left[\mathfrak{h}\left(\frac{2\sigma+\delta}{3}\right)\right]^3\mathfrak{h}(\delta)\right]^{\frac{1}{8}}}{\left[_\sigma I_*^\beta \mathfrak{h}(\delta)_* I_\delta^\beta \mathfrak{h}(\sigma)\right]^{\frac{\Gamma(\beta+1)}{2(\delta-\sigma)^\beta}}} \right| \leq [\mathfrak{h}^*(\sigma)\mathfrak{h}^*(\delta)]^{\frac{[\Omega_3(\beta)+\Omega_4(\beta)+\Omega_5(\beta)](\delta-\sigma)}{2}},$$

where

$$\Omega_3(\beta) = \int_0^{\frac{1}{3}}\left|t^\beta - \frac{1}{8}\right|dt = \begin{cases} \frac{2\beta v^{\beta+1}}{\beta+1} + \frac{1}{3^{\beta+1}(\beta+1)} - \frac{1}{24}, & 0 < \beta < \frac{\ln(1/8)}{\ln(1/3)}, \\[2ex] \frac{1}{24} - \frac{1}{3^{\beta+1}(\beta+1)}, & \beta > \frac{\ln(1/8)}{\ln(1/3)}, \end{cases}$$

$$\Omega_4(\beta) = \int_{\frac{1}{3}}^{\frac{2}{3}}\left|t^\beta - \frac{1}{2}\right|dt = \begin{cases} \frac{2^{\beta+1}-1}{3^{\beta+1}(\beta+1)} - \frac{1}{6} & 0 < \beta < \frac{\ln(1/2)}{\ln(1/3)} \\[2ex] \frac{\beta\xi}{\beta+1} + \frac{2^{\beta+1}+1}{3^{\beta+1}(\beta+1)} - \frac{1}{2}, & \frac{\ln(1/2)}{\ln(1/3)} < \beta < \frac{\ln(1/2)}{\ln(2/3)}, \\[2ex] \frac{1}{6} - \frac{2^{\beta+1}-1}{3^{\beta+1}(\beta+1)}, & \beta > \frac{\ln(1/2)}{\ln(2/3)}, \end{cases}$$

$$\Omega_5(\beta) = \int_{\frac{2}{3}}^{1}\left|t^\beta - \frac{7}{8}\right|dt = \begin{cases} \frac{2\beta \kappa^{\beta+1}}{\beta+1} + \frac{3^{\beta+1}+2^{\beta+1}}{3^{\beta+1}(\beta+1)} - \frac{35}{24}, & \beta > \frac{\ln(7/8)}{\ln(2/3)}, \\[2ex] \frac{3^{\beta+1}-2^{\beta+1}}{3^{\beta+1}(\beta+1)} - \frac{7}{24}, & 0 < \beta < \frac{\ln(7/8)}{\ln(2/3)}. \end{cases}$$

Definition 2.17. *[48] Let the function $\mathfrak{h} \in L_1([\sigma, \delta])$. For the order $\beta > 0$ and $\alpha \in (0, 1]$, the Conformable Fractional Integrals (CFI) $_+^\beta I_\sigma^\alpha \mathfrak{h}(x)$ and $_-^\beta I_\delta^\alpha \mathfrak{h}(x)$, correspondingly, are defined by*

$$_+^\beta I_\sigma^\alpha \mathfrak{h}(x) = \frac{1}{\Gamma(\beta)} \int_\sigma^x \left(\frac{(x-\sigma)^\alpha - (t-\sigma)^\alpha}{\alpha}\right)^{\beta-1} (t-\sigma)^{\alpha-1}\mathfrak{h}(t)dt, x > \sigma$$

and

$$_-^\beta I_\delta^\alpha \mathfrak{h}(x) = \frac{1}{\Gamma(\beta)} \int_x^\delta \left(\frac{(\delta-x)^\alpha - (\delta-t)^\alpha}{\alpha}\right)^{\beta-1} (\delta-t)^{\alpha-1}\mathfrak{h}(t)dt, \delta > x$$

respectively. Here, Γ represents Euler Gamma function.

Definition 2.18. *[44] The multiplicative left conformable fractional integral $(_\sigma^\beta \mathscr{I}_*^\alpha \mathfrak{h})(x)$ of order $\beta > 0$ and $\alpha \in (0, 1]$ by*

$$\begin{aligned} (_\sigma^\beta \mathscr{I}_*^\alpha \mathfrak{h})(x) &= \exp\left\{_+^\beta I_\sigma^\alpha((\ln \circ \mathfrak{h})(x))\right\} \\[2ex] &= \exp\left\{\frac{1}{\Gamma(\beta)}\int_\sigma^x \left(\frac{(x-\sigma)^\alpha - (t-\sigma)^\alpha}{\alpha}\right)^{\beta-1}\frac{(\ln \circ \mathfrak{h})(t)}{(t-\sigma)^{1-\alpha}}dt, x > \sigma\right\}, \end{aligned}$$

and the multiplicative right conformable fractional integral $(_*^\beta \mathscr{I}_\delta^\alpha \mathfrak{h})(x)$ is defined by

$$\begin{aligned} (_*^\beta \mathscr{I}_\delta^\alpha \mathfrak{h})(x) &= \exp\left\{_-^\beta I_\delta^\alpha((\ln \circ \mathfrak{h})(x))\right\} \\[2ex] &= \exp\left\{\frac{1}{\Gamma(\beta)}\int_x^\delta \left(\frac{(\delta-x)^\alpha - (\delta-t)^\alpha}{\alpha}\right)^{\beta-1}\frac{(\ln \circ \mathfrak{h})(t)}{(\delta-t)^{1-\alpha}}dt, \delta > x\right\}. \end{aligned}$$

Here, Γ is Euler Gamma function.

Theorem 2.19. *[44]We have the following properties for multiplicative conformable fractional integrals:*

1. *It is postulated that the function* $\mathfrak{h} : [\sigma, \delta] \to (0, +\infty)$ *is *integrable. Then, both* ${}^{\beta}_{\sigma}\mathscr{I}^{\alpha}_{*}\mathfrak{h}(x)$ *and* ${}^{\beta}_{*}\mathscr{I}^{\alpha}_{\delta}\mathfrak{h}(x)$ *operators are multiplicative integrable on* $[\sigma, \delta]$.

2. *Assume that the function* $\mathfrak{h} : [\sigma, \delta] \to (0, +\infty)$ *is integrable. Then, we arrive at the conclusion that, both* $ln\left({}^{\beta}_{\sigma}\mathscr{I}^{\alpha}_{*}\mathfrak{h}(x)\right)$ *and* $ln\left({}^{\beta}_{*}\mathscr{I}^{\alpha}_{\delta}\mathfrak{h}(x)\right)$ *operators exhibit continuity on* $[\sigma, \delta]$.

3. *Suppose that* $\mathfrak{h} : [\sigma, \delta] \to (0, +\infty)$ *is a *integrable function and is bounded on* $[\sigma, \delta]$. *Then, both* ${}^{\beta}_{\sigma}\mathscr{I}^{\alpha}_{*}\mathfrak{h}(x)$ *and* ${}^{\beta}_{*}\mathscr{I}^{\alpha}_{\delta}\mathfrak{h}(x)$ *operators are correspondingly bounded on* $[\sigma, \delta]$ *as well.*

4. *Suppose that the functions* $\mathfrak{h}$ *and* $g : [\sigma, \delta] \to (0, +\infty)$ *are *integrable on* (σ, δ). *The operators* ${}^{\beta}_{\sigma}\mathscr{I}^{\alpha}_{*}\mathfrak{h}(x)$ *and* ${}^{\beta}_{*}\mathscr{I}^{\alpha}_{\delta}\mathfrak{h}(x)$ *are multiplicatively linear. That is, we can get*

$$
{}^{\beta}_{\sigma}\mathscr{I}^{\alpha}_{*}((\mathfrak{h}^{m} \cdot g^{n})(x)) = \left[{}^{\beta}_{\sigma}\mathscr{I}^{\alpha}_{*}\mathfrak{h}(x)\right]^{m} \left[{}^{\beta}_{\sigma}\mathscr{I}^{\alpha}_{*}g(x)\right]^{n}, m, n \in \mathbb{R}
$$

and

$$
{}^{\beta}_{*}\mathscr{I}^{\alpha}_{\delta}((\mathfrak{h}^{m} \cdot g^{n})(x)) = \left[{}^{\beta}_{*}\mathscr{I}^{\alpha}_{\delta}\mathfrak{h}(x)\right]^{m} \left[{}^{\beta}_{*}\mathscr{I}^{\alpha}_{\delta}g(x)\right]^{n}, m, n \in \mathbb{R}.
$$

5. *Let* $\mathfrak{h} : [\sigma, \delta] \to (0, +\infty)$ *be a continuous function, where* $0 < \sigma < \delta$, *and with* α, β *and* γ *all positive. Then, it follows that for all* $x \in [\sigma, \delta]$, *we obtain*

$$
{}^{\beta}_{\sigma}\mathscr{I}^{\alpha}_{*}\left[{}^{\gamma}_{\sigma}\mathscr{I}^{\alpha}_{*}\mathfrak{h}(x)\right] = {}^{\beta+\gamma}_{\sigma}\mathscr{I}^{\alpha}_{*}\mathfrak{h}(x) = {}^{\gamma}_{\sigma}\mathscr{I}^{\alpha}_{*}\left[{}^{\beta}_{\sigma}\mathscr{I}^{\alpha}_{*}\mathfrak{h}(x)\right]
$$

and

$$
{}^{\beta}_{*}\mathscr{I}^{\alpha}_{\delta}\left[{}^{\gamma}_{*}\mathscr{I}^{\alpha}_{\delta}\mathfrak{h}(x)\right] = {}^{\beta+\gamma}_{*}\mathscr{I}^{\alpha}_{\delta}\mathfrak{h}(x) = {}^{\gamma}_{*}\mathscr{I}^{\alpha}_{\delta}\left[{}^{\beta}_{*}\mathscr{I}^{\alpha}_{\delta}\mathfrak{h}(x)\right].
$$

3. A Key Identity for MCFI

In this section, we will prove an identity involving MCFI for multiplicative differentiable functions.

Lemma 3.1. *Let* $\mathfrak{h} : [\sigma, \delta] \to \mathbb{R}^{+}$ *be multiplicative differentiable function over* (σ, δ). *If* $\mathfrak{h}^{*}$ *is multiplicative integrable on* $[\sigma, \delta]$, *then the following equality holds:*

$$
\frac{\left[\mathfrak{h}(\sigma).\mathfrak{h}\left(\frac{2\sigma+\delta}{3}\right)^{3}.\mathfrak{h}\left(\frac{\sigma+2\delta}{3}\right)^{3}.\mathfrak{h}(\delta)\right]^{\frac{1}{8}}}{\left[{}^{\beta}_{*}\mathscr{I}^{\alpha}_{\delta}\mathfrak{h}(\sigma).{}^{\beta}_{\sigma}\mathscr{I}^{\alpha}_{*}\mathfrak{h}(\delta)\right]^{\frac{\alpha^{\beta}\Gamma(\beta+1)}{2(\delta-\sigma)^{\alpha\beta}}}} = [I_1 \times I_2 \times I_3 \times I_4 \times I_5 \times I_6]^{\frac{\alpha^{\beta}(\delta-\sigma)}{2}}. \tag{3.1}
$$

Here,

$$
I_1 \quad : \quad = \int_{0}^{\frac{1}{3}} \left([\mathfrak{h}^{*}(t\delta+(1-t)\sigma)]^{\left(\left(\frac{1-(1-t)^{\alpha}}{\alpha}\right)^{\beta}-\frac{1}{8\alpha^{\beta}}\right)}\right)^{dt},
$$

$$
I_2 \quad : \quad = \int_{0}^{\frac{1}{3}} \left([\mathfrak{h}^{*}(t\sigma+(1-t)\delta)]^{\left(\frac{1}{8\alpha^{\beta}}-\left(\frac{1-(1-t)^{\alpha}}{\alpha}\right)^{\beta}\right)}\right)^{dt},
$$

$$
I_3 \quad : \quad = \int_{\frac{1}{3}}^{\frac{2}{3}} \left([\mathfrak{h}^{*}(t\delta+(1-t)\sigma)]^{\left(\left(\frac{1-(1-t)^{\alpha}}{\alpha}\right)^{\beta}-\frac{1}{2\alpha^{\beta}}\right)}\right)^{dt},
$$

$$
I_4 \quad : \quad = \int_{\frac{1}{3}}^{\frac{2}{3}} \left([\mathfrak{h}^{*}(t\sigma+(1-t)\delta)]^{\left(\frac{1}{2\alpha^{\beta}}-\left(\frac{1-(1-t)^{\alpha}}{\alpha}\right)^{\beta}\right)}\right)^{dt},
$$

$$
I_5 \quad : \quad = \int_{\frac{2}{3}}^{1} \left([\mathfrak{h}^{*}(t\delta+(1-t)\sigma)]^{\left(\left(\frac{1-(1-t)^{\alpha}}{\alpha}\right)^{\beta}-\frac{7}{8\alpha^{\beta}}\right)}\right)^{dt},
$$

$$
I_6 \quad : \quad = \int_{\frac{2}{3}}^{1} \left([\mathfrak{h}^{*}(t\sigma+(1-t)\delta)]^{\left(\frac{7}{8\alpha^{\beta}}-\left(\frac{1-(1-t)^{\alpha}}{\alpha}\right)^{\beta}\right)}\right)^{dt},
$$

and Γ *is Euler Gamma function.*

Proof. By using Theorem 2.6, we have

$$
\begin{aligned}
I_1 &= \int_0^{\frac{1}{3}} \left([\mathfrak{h}^*(t\delta + (1-t)\sigma)]^{\left(\left(\frac{1-(1-t)^\alpha}{\alpha} \right)^\beta - \frac{1}{8\alpha^\beta} \right)} \right)^{dt} \\[2mm]
&= \left[\int_0^{\frac{1}{3}} \left([\mathfrak{h}^*(t\delta + (1-t)\sigma)]^{\left(\left(\frac{1-(1-t)^\alpha}{\alpha} \right)^\beta - \frac{1}{8\alpha^\beta} \right)(\delta-\sigma)} \right)^{dt} \right]^{\frac{1}{\delta-\sigma}} \\[2mm]
&= \frac{\left[\mathfrak{h}\left(\frac{\delta+2\sigma}{3} \right) \right]^{\frac{1}{\delta-\sigma} \left[\left(\frac{3^\alpha - 2^\alpha}{\alpha 3^\alpha} \right)^\beta - \frac{1}{8\alpha^\beta} \right]}}{\mathfrak{h}(\sigma)^{-\frac{1}{(\delta-\sigma)8\alpha^\beta}}} \cdot \frac{1}{\left[\int_0^{\frac{1}{3}} \left([\mathfrak{h}(t\delta+(1-t)\sigma)]^{\beta(1-t)^{\alpha-1} \left(\frac{1-(1-t)^\alpha}{\alpha} \right)^{\beta-1}} \right)^{dt} \right]^{\frac{1}{\delta-\sigma}}} \\[2mm]
&= \frac{\left[\mathfrak{h}\left(\frac{\delta+2\sigma}{3} \right) \right]^{\frac{1}{\delta-\sigma} \left[\left(\frac{3^\alpha - 2^\alpha}{\alpha 3^\alpha} \right)^\beta - \frac{1}{8\alpha^\beta} \right]} \cdot \mathfrak{h}(\sigma)^{\frac{1}{8(\delta-\sigma)\alpha^\beta}}}{\exp\left\{ \frac{1}{\delta-\sigma} \int_0^{\frac{1}{3}} \beta(1-t)^{\alpha-1} \left(\frac{1-(1-t)^\alpha}{\alpha} \right)^{\beta-1} \ln \mathfrak{h}(t\delta+(1-t)\sigma)\,dt \right\}} \\[2mm]
&= \frac{\left[\mathfrak{h}\left(\frac{\delta+2\sigma}{3} \right) \right]^{\frac{1}{\delta-\sigma} \left[\left(\frac{3^\alpha - 2^\alpha}{\alpha 3^\alpha} \right)^\beta - \frac{1}{8\alpha^\beta} \right]} \cdot \mathfrak{h}(\sigma)^{\frac{1}{8(\delta-\sigma)\alpha^\beta}}}{\exp\left\{ \frac{1}{\delta-\sigma} \int_\sigma^{\frac{\delta+2\sigma}{3}} \beta \left(\frac{\delta-u}{\delta-\sigma} \right)^{\alpha-1} \left(\frac{(\delta-\sigma)^\alpha - (\delta-u)^\alpha}{\alpha(\delta-\sigma)^\alpha} \right)^{\beta-1} \ln \mathfrak{h}(u)\,\frac{1}{\delta-\sigma}\,du \right\}} \\[2mm]
&= \frac{\left[\mathfrak{h}\left(\frac{\delta+2\sigma}{3} \right) \right]^{\frac{1}{\delta-\sigma} \left[\left(\frac{3^\alpha - 2^\alpha}{\alpha 3^\alpha} \right)^\beta - \frac{1}{8\alpha^\beta} \right]} \cdot \mathfrak{h}(\sigma)^{\frac{1}{8(\delta-\sigma)\alpha^\beta}}}{\exp\left\{ \frac{\Gamma(\beta+1)}{(\delta-\sigma)^{\alpha\beta+1}\Gamma(\beta)} \int_\sigma^{\frac{\delta+2\sigma}{3}} (\delta-u)^{\alpha-1} \left(\frac{(\delta-\sigma)^\alpha - (\delta-u)^\alpha}{\alpha} \right)^{\beta-1} \ln \mathfrak{h}(u)\,du \right\}},
\end{aligned}
$$

$$(3.2)$$

$$
\begin{aligned}
I_2 &= \int_0^{\frac{1}{3}} \left([\mathfrak{h}^*(t\sigma + (1-t)\delta)]^{\left(\frac{1}{8\alpha^\beta} - \left(\frac{1-(1-t)^\alpha}{\alpha} \right)^\beta \right)} \right)^{dt} \\[2mm]
&= \frac{\left[\mathfrak{h}\left(\frac{\sigma+2\delta}{3} \right) \right]^{\frac{1}{\delta-\sigma} \left[\left(\frac{3^\alpha - 2^\alpha}{\alpha 3^\alpha} \right)^\beta - \frac{1}{8\alpha^\beta} \right]} \cdot \mathfrak{h}(\delta)^{\frac{1}{8(\delta-\sigma)\alpha^\beta}}}{\exp\left\{ \frac{\Gamma(\beta+1)}{(\delta-\sigma)^{\alpha\beta+1}\Gamma(\beta)} \int_{\frac{2\delta+\sigma}{3}}^{\delta} (k-\sigma)^{\alpha-1} \left(\frac{(\delta-\sigma)^\alpha - (k-\sigma)^\alpha}{\alpha} \right)^{\beta-1} \ln \mathfrak{h}(k)\,dk \right\}},
\end{aligned}
$$

$$(3.3)$$

$$
\begin{aligned}
I_3 &= \int_{\frac{1}{3}}^{\frac{2}{3}} \left([\mathfrak{h}^*(t\delta + (1-t)\sigma)]^{\left(\left(\frac{1-(1-t)^\alpha}{\alpha} \right)^\beta - \frac{1}{2\alpha^\beta} \right)} \right)^{dt} \\[2mm]
&= \left[\int_{\frac{1}{3}}^{\frac{2}{3}} \left([\mathfrak{h}^*(t\delta + (1-t)\sigma)]^{\left(\left(\frac{1-(1-t)^\alpha}{\alpha} \right)^\beta - \frac{1}{2\alpha^\beta} \right)(\delta-\sigma)} \right)^{dt} \right]^{\frac{1}{\delta-\sigma}} \\[2mm]
&= \frac{\left[\mathfrak{h}\left(\frac{\sigma+2\delta}{2} \right) \right]^{\frac{1}{\delta-\sigma} \left[\left(\frac{3^\alpha - 1}{3^\alpha \alpha} \right)^\beta - \frac{1}{2\alpha^\beta} \right]}}{\left[\mathfrak{h}\left(\frac{\delta+2\sigma}{3} \right) \right]^{\frac{1}{\delta-\sigma} \left[\left(\frac{3^\alpha - 2^\alpha}{\alpha 3^\alpha} \right)^\beta - \frac{1}{2\alpha^\beta} \right]}} \cdot \frac{1}{\left[\int_{\frac{1}{3}}^{\frac{2}{3}} \left([\mathfrak{h}(t\delta+(1-t)\sigma)]^{\beta(1-t)^{\alpha-1} \left(\frac{1-(1-t)^\alpha}{\alpha} \right)^{\beta-1}} \right)^{dt} \right]^{\frac{1}{\delta-\sigma}}} \\[2mm]
&= \frac{\left[\mathfrak{h}\left(\frac{\sigma+2\delta}{2} \right) \right]^{\frac{1}{\delta-\sigma} \left(\left(\frac{3^\alpha - 1}{3^\alpha \alpha} \right)^\beta - \frac{1}{2\alpha^\beta} \right)} \cdot \left[\mathfrak{h}\left(\frac{\delta+2\sigma}{3} \right) \right]^{\frac{1}{\delta-\sigma} \left(\frac{1}{2\alpha^\beta} - \left(\frac{3^\alpha - 2^\alpha}{\alpha 3^\alpha} \right)^\beta \right)}}{\exp\left\{ \frac{1}{\delta-\sigma} \int_{\frac{2}{3}}^{\frac{1}{3}} \beta(1-t)^{\alpha-1} \left(\frac{1-(1-t)^\alpha}{\alpha} \right)^{\beta-1} \ln \mathfrak{h}(t\delta+(1-t)\sigma)\,dt \right\}}
\end{aligned}
$$

$$(3.4)$$

$$= \frac{\left[\hbar\left(\frac{\sigma+2\delta}{2}\right)\right]^{\frac{1}{\delta-\sigma}\left(\left(\frac{3^{\alpha}-1}{3^{\alpha}\alpha}\right)^{\beta}-\frac{1}{2\alpha^{\beta}}\right)} \cdot \left[\hbar\left(\frac{\delta+2\sigma}{3}\right)\right]^{\frac{1}{\delta-\sigma}\left(\frac{1}{2\alpha^{\beta}}-\left(\frac{3^{\alpha}-2^{\alpha}}{\alpha3^{\alpha}}\right)^{\beta}\right)}}{\exp\left\{\frac{1}{\delta-\sigma}\int_{\frac{2\sigma+\delta}{3}}^{\frac{\sigma+2\delta}{3}} \beta\left(\frac{\delta-k}{\delta-\sigma}\right)^{\alpha-1}\left(\frac{(\delta-\sigma)^{\alpha}-(\delta-k)^{\alpha}}{\alpha}\right)^{\beta-1}\ln\hbar(k)\frac{1}{\delta-\sigma}dk\right\}}$$

$$= \frac{\left[\hbar\left(\frac{\sigma+2\delta}{2}\right)\right]^{\frac{1}{\delta-\sigma}\left(\left(\frac{3^{\alpha}-1}{3^{\alpha}\alpha}\right)^{\beta}-\frac{1}{2\alpha^{\beta}}\right)} \cdot \left[\hbar\left(\frac{\delta+2\sigma}{3}\right)\right]^{\frac{1}{\delta-\sigma}\left(\frac{1}{2\alpha^{\beta}}-\left(\frac{3^{\alpha}-2^{\alpha}}{\alpha3^{\alpha}}\right)^{\beta}\right)}}{\exp\left\{\frac{\Gamma(\beta+1)}{(\delta-\sigma)^{\alpha\beta+1}\Gamma(\beta)}\int_{\frac{\delta+2\sigma}{3}}^{\frac{\sigma+2\delta}{3}} (\delta-k)^{\alpha-1}\left(\frac{(\delta-\sigma)^{\alpha}-(\delta-k)^{\alpha}}{\alpha}\right)^{\beta-1}\ln\hbar(k)dk\right\}},$$

$$I_4 = \int_{\frac{1}{3}}^{\frac{2}{3}} \left([\hbar^*(t\sigma+(1-t)\delta)]^{\left(\frac{1}{2\alpha^{\beta}}-\left(\frac{1-(1-t)^{\alpha}}{\alpha}\right)^{\beta}\right)}\right)^{dt} \qquad (3.5)$$

$$= \frac{\left[\hbar\left(\frac{2\sigma+\delta}{2}\right)\right]^{\frac{1}{\delta-\sigma}\left(\left(\frac{3^{\alpha}-1}{3^{\alpha}\alpha}\right)^{\beta}-\frac{1}{2\alpha^{\beta}}\right)} \cdot \left[\hbar\left(\frac{2\delta+\sigma}{3}\right)\right]^{\frac{1}{\delta-\sigma}\left(\frac{1}{2\alpha^{\beta}}-\left(\frac{3^{\alpha}-2^{\alpha}}{\alpha3^{\alpha}}\right)^{\beta}\right)}}{\exp\left\{\frac{\Gamma(\beta+1)}{(\delta-\sigma)^{\alpha\beta+1}\Gamma(\beta)}\int_{\frac{2\sigma+\delta}{3}}^{\frac{\sigma+2\delta}{3}} (k-\sigma)^{\alpha-1}\left(\frac{(\delta-\sigma)^{\alpha}-(k-\sigma)^{\alpha}}{\alpha}\right)^{\beta-1}\ln\hbar(k)dk\right\}},$$

$$I_5 = \int_{\frac{2}{3}}^{1} \left([\hbar^*(t\delta+(1-t)\sigma)]^{\left(\left(\frac{1-(1-t)^{\alpha}}{\alpha}\right)^{\beta}-\frac{7}{8\alpha^{\beta}}\right)}\right)^{dt} \qquad (3.6)$$

$$= \left[\int_{\frac{2}{3}}^{1} \left([\hbar^*(t\delta+(1-t)\sigma)]^{\left(\left(\frac{1-(1-t)^{\alpha}}{\alpha}\right)^{\beta}-\frac{7}{8\alpha^{\beta}}\right)(\delta-\sigma)}\right)^{dt}\right]^{\frac{1}{\delta-\sigma}}$$

$$= \frac{[\hbar(\delta)]^{\frac{1}{(\delta-\sigma)8\alpha^{\beta}}}}{\left[\hbar\left(\frac{\sigma+2\delta}{3}\right)\right]^{\frac{1}{\delta-\sigma}\left[\left(\frac{3^{\alpha}-1}{\alpha3^{\alpha}}\right)^{\beta}-\frac{7}{8\alpha^{\beta}}\right]}} \cdot \frac{1}{\left[\int_{\frac{2}{3}}^{1}\left([\hbar(t\delta+(1-t)\sigma)]^{\beta(1-t)^{\alpha-1}\left(\frac{1-(1-t)^{\alpha}}{\alpha}\right)^{\beta-1}}\right)^{dt}\right]^{\frac{1}{\delta-\sigma}}}$$

$$= \frac{[\hbar(\delta)]^{\frac{1}{(\delta-\sigma)8\alpha^{\beta}}} \cdot \left[\hbar\left(\frac{\sigma+2\delta}{3}\right)\right]^{\frac{1}{\delta-\sigma}\left(\frac{7}{8\alpha^{\beta}}-\left(\frac{3^{\alpha}-1}{\alpha3^{\alpha}}\right)^{\beta}\right)}}{\exp\left\{\frac{1}{\delta-\sigma}\int_{\frac{2}{3}}^{1}\beta(1-t)^{\alpha-1}\left(\frac{1-(1-t)^{\alpha}}{\alpha}\right)^{\beta-1}\ln\hbar(t\delta+(1-t)\sigma)dt\right\}}$$

$$= \frac{[\hbar(\delta)]^{\frac{1}{(\delta-\sigma)8\alpha^{\beta}}} \cdot \left[\hbar\left(\frac{\sigma+2\delta}{3}\right)\right]^{\frac{1}{\delta-\sigma}\left(\frac{7}{8\alpha^{\beta}}-\left(\frac{3^{\alpha}-1}{\alpha3^{\alpha}}\right)^{\beta}\right)}}{\exp\left\{\frac{1}{\delta-\sigma}\int_{\frac{\sigma+2\delta}{3}}^{\delta}\beta\left(\frac{\delta-k}{\delta-\sigma}\right)^{\alpha-1}\left(\frac{(\delta-\sigma)^{\alpha}-(\delta-k)^{\alpha}}{\alpha}\right)^{\beta-1}\ln\hbar(k)\frac{1}{\delta-\sigma}dk\right\}}$$

$$= \frac{[\hbar(\delta)]^{\frac{1}{(\delta-\sigma)8\alpha^{\beta}}} \cdot \left[\hbar\left(\frac{\sigma+2\delta}{3}\right)\right]^{\frac{1}{\delta-\sigma}\left(\frac{7}{8\alpha^{\beta}}-\left(\frac{3^{\alpha}-1}{\alpha3^{\alpha}}\right)^{\beta}\right)}}{\exp\left\{\frac{\Gamma(\beta+1)}{(\delta-\sigma)^{\alpha\beta+1}\Gamma(\beta)}\int_{\frac{\sigma+2\delta}{3}}^{\delta} (\delta-k)^{\alpha-1}\left(\frac{(\delta-\sigma)^{\alpha}-(\delta-k)^{\alpha}}{\alpha}\right)^{\beta-1}\ln\hbar(k)dk\right\}},$$

and

$$I_6 = \int_{\frac{2}{3}}^{1} \left([\hbar^*(t\sigma+(1-t)\delta)]^{\left(\frac{7}{8\alpha^{\beta}}-\left(\frac{1-(1-t)^{\alpha}}{\alpha}\right)^{\beta}\right)}\right)^{dt} \qquad (3.7)$$

$$= \frac{[\hbar(\sigma)]^{\frac{1}{(\delta-\sigma)8\alpha^{\beta}}} \cdot \left[\hbar\left(\frac{2\sigma+\delta}{3}\right)\right]^{\frac{1}{\delta-\sigma}\left(\frac{7}{8\alpha^{\beta}}-\left(\frac{3^{\alpha}-1}{\alpha3^{\alpha}}\right)^{\beta}\right)}}{\exp\left\{\frac{\Gamma(\beta+1)}{(\delta-\sigma)^{\alpha\beta+1}\Gamma(\beta)}\int_{\sigma}^{\frac{2\sigma+\delta}{3}} (k-\sigma)^{\alpha-1}\left(\frac{(\delta-\sigma)^{\alpha}-(k-\sigma)^{\alpha}}{\alpha}\right)^{\beta-1}\ln\hbar(k)dk\right\}}.$$

By multiplying the results of (3.2)-(3.7) and raising both sides of the obtained identity to the power of $\frac{(\delta-\sigma)\alpha^{\beta}}{2}$, we obtain the equality (3.1). $\square$

Remark 3.2. *If we pick $\alpha = 1$ in Lemma 3.1, then we obtain the next identity holds for MRLFI:*

$$\frac{\left[\mathfrak{h}(\sigma).\mathfrak{h}\left(\frac{2\sigma+\delta}{3}\right)^3.\mathfrak{h}\left(\frac{\sigma+2\delta}{3}\right)^3.\mathfrak{h}(\delta)\right]^{\frac{1}{8}}}{\left[_*I_\delta^\beta\mathfrak{h}(\sigma)._\sigma I_*^\beta\mathfrak{h}(\delta)\right]^{\frac{\Gamma(\beta+1)}{2(\delta-\sigma)\beta}}} = [K_1 \times K_2 \times K_3 \times K_4 \times K_5 \times K_6]^{\frac{\delta-\sigma}{2}} .$$

Here,

$$K_1 \quad : \quad = \int_0^{\frac{1}{3}} \left([\mathfrak{h}^*(t\delta+(1-t)\sigma)]^{\left(t^\beta-\frac{1}{8}\right)}\right)^{dt},$$

$$K_2 \quad : \quad = \int_0^{\frac{1}{3}} \left([\mathfrak{h}^*(t\sigma+(1-t)\delta)]^{\left(\frac{1}{8}-t^\beta\right)}\right)^{dt},$$

$$K_3 \quad : \quad = \int_{\frac{1}{3}}^{\frac{2}{3}} \left([\mathfrak{h}^*(t\delta+(1-t)\sigma)]^{\left(t^\beta-\frac{1}{2}\right)}\right)^{dt},$$

$$K_4 \quad : \quad = \int_{\frac{1}{3}}^{\frac{2}{3}} \left([\mathfrak{h}^*(t\sigma+(1-t)\delta)]^{\left(\frac{1}{2}-t^\beta\right)}\right)^{dt},$$

$$K_5 \quad : \quad = \int_{\frac{2}{3}}^{1} \left([\mathfrak{h}^*(t\delta+(1-t)\sigma)]^{\left(t^\beta-\frac{7}{8}\right)}\right)^{dt},$$

$$K_6 \quad : \quad = \int_{\frac{2}{3}}^{1} \left([\mathfrak{h}^*(t\sigma+(1-t)\delta)]^{\left(\frac{7}{8}-t^\beta\right)}\right)^{dt}.$$

This result is presented by Ali in [37, Lemma 3.2]

Remark 3.3. *Picking $\beta = \alpha = 1$ in Lemma 3.1, then we obtain the next identity holds for multiplicative integrals:*

$$\frac{\left[\mathfrak{h}(\sigma).\mathfrak{h}\left(\frac{2\sigma+\delta}{3}\right)^3.\mathfrak{h}\left(\frac{\sigma+2\delta}{3}\right)^3.\mathfrak{h}(\delta)\right]^{\frac{1}{8}}}{\left[\int_\sigma^\delta(\mathfrak{h}(t))^{dt}\right]^{\frac{1}{(\delta-\sigma)}}} = [A_1 \times A_2 \times A_3]^{(\delta-\sigma)},$$

here

$$A_1 \quad = \quad \int_0^{\frac{1}{3}} \left([\mathfrak{h}^*(x\delta+(1-x)\sigma)]^{\left(x-\frac{1}{8}\right)}\right)^{dt},$$

$$A_2 \quad = \quad \int_{\frac{1}{3}}^{\frac{2}{3}} \left([\mathfrak{h}^*(x\delta+(1-x)\sigma)]^{\left(x-\frac{1}{2}\right)}\right)^{dt},$$

$$A_3 \quad = \quad \int_{\frac{2}{3}}^{1} \left([\mathfrak{h}^*(x\delta+(1-x)\sigma)]^{\left(x-\frac{7}{8}\right)}\right)^{dt},$$

which is presented by Chasreechai et al. in [27, Lemma 3.2]

4. Newton-type Inequalities by Multiplicative Convex Functions

In this section, we will prove the new form of Newton-type inequalities involving MCFI for multiplicative convex functions.

Theorem 4.1. *Assume that all conditions of Lemma 3.1 are satisfy. If $\mathfrak{h}^*$ is increasing and multiplicatively convex over $[\sigma, \delta]$, then for $\alpha \in (0, 1]$ and $\beta > 0$, we establish the following inequality:*

$$\left| \frac{\left[\mathfrak{h}(\sigma).\mathfrak{h}\left(\frac{2\sigma+\delta}{3}\right)^3.\mathfrak{h}\left(\frac{\sigma+2\delta}{3}\right)^3.\mathfrak{h}(\delta)\right]^{\frac{1}{8}}}{\left[_*^\beta\mathscr{I}_\delta^\alpha\mathfrak{h}(\sigma)._\sigma^\beta\mathscr{I}_*^\alpha\mathfrak{h}(\delta)\right]^{\frac{\alpha\beta\Gamma(\beta+1)}{2(\delta-\sigma)\alpha\beta}}} \right| \leq [\mathfrak{h}^*(\sigma)\mathfrak{h}^*(\delta)]^{\frac{\alpha\beta(\delta-\sigma)}{2}[\Psi_1(\alpha,\beta)+\Psi_2(\alpha,\beta)+\Psi_3(\alpha,\beta)]} .$$

Here

$$\Psi_1(\alpha,\beta) = \int_0^{\frac{1}{3}} \left| \frac{1}{8\alpha^\beta} - \left(\frac{1-(1-t)^\alpha}{\alpha} \right)^\beta \right| dt$$

$$= \begin{cases} \frac{1}{\alpha^\beta} \left[\frac{6T-1}{24} + \frac{1}{\alpha} \left(2\mathfrak{B}\left(\frac{1}{\alpha}, \beta+1, 1-\left(\frac{1}{8}\right)^{\frac{1}{\beta}} \right) \right. \right. \\ \left. \left. -\mathfrak{B}\left(\frac{1}{\alpha}, \beta+1, \left(\frac{2}{3}\right)^\alpha \right) - B\left(\frac{1}{\alpha}, \beta \right) \right) \right], & 0 < \beta < \frac{\ln\left(\frac{1}{8}\right)}{\ln\left(1-\left(\frac{2}{3}\right)^\alpha\right)} \\[4mm] \frac{1}{\alpha^\beta} \left[\frac{1}{24} - \frac{1}{\alpha} \left(B\left(\frac{1}{\alpha}, \beta+1 \right) - \mathfrak{B}\left(\frac{1}{\alpha}, \beta+1, \left(\frac{1}{3}\right)^\alpha \right) \right) \right], & \beta > \frac{\ln\left(\frac{1}{8}\right)}{\ln\left(1-\left(\frac{2}{3}\right)^\alpha\right)} \end{cases}$$

$$\Psi_2(\alpha,\beta) = \int_{\frac{1}{3}}^{\frac{2}{3}} \left| \frac{1}{2\alpha^\beta} - \left(\frac{1-(1-t)^\alpha}{\alpha} \right)^\beta \right| dt$$

$$= \begin{cases} \frac{1}{\alpha^\beta} \left[\frac{1}{\alpha} \left(\mathfrak{B}\left(\frac{1}{\alpha}, \beta+1, \left(\frac{2}{3}\right)^\alpha \right) - \mathfrak{B}\left(\frac{1}{\alpha}, \beta+1, \left(\frac{1}{3}\right)^\alpha \right) \right) - \frac{1}{6} \right], & \beta < \frac{\ln\left(\frac{1}{2}\right)}{\ln\left(1-\left(\frac{2}{3}\right)^\alpha\right)} \\[4mm] \frac{1}{\alpha^\beta} \left[\frac{2K-1}{2} + \frac{1}{\alpha} \left(2\mathfrak{B}\left(\frac{1}{\alpha}, \beta+1, \left(1-\left(\frac{1}{2}\right)^{\frac{1}{\beta}}\right) \right) \right. \right. \\ \left. \left. -\mathfrak{B}\left(\frac{1}{\alpha}, \beta+1, \left(\frac{2}{3}\right)^\alpha \right) - \mathfrak{B}\left(\frac{1}{\alpha}, \beta+1, \left(\frac{1}{3}\right)^\alpha \right) \right) \right], & \frac{\ln\left(\frac{1}{2}\right)}{\ln\left(1-\left(\frac{2}{3}\right)^\alpha\right)} < \beta < \frac{\ln\left(\frac{1}{2}\right)}{\ln\left(1-\left(\frac{1}{3}\right)^\alpha\right)} \\[4mm] \frac{1}{\alpha^\beta} \left[\frac{1}{6} + \frac{1}{\alpha} \left(\mathfrak{B}\left(\frac{1}{\alpha}, \beta+1, \left(\frac{1}{3}\right)^\alpha \right) - \mathfrak{B}\left(\frac{1}{\alpha}, \beta+1, \left(\frac{2}{3}\right)^\alpha \right) \right) \right], & \beta > \frac{\ln\left(\frac{1}{2}\right)}{\ln\left(1-\left(\frac{1}{3}\right)^\alpha\right)} \end{cases}$$

and

$$\Psi_3(\alpha,\beta) = \int_{\frac{1}{3}}^{1} \left| \frac{7}{8\alpha^\beta} - \left(\frac{1-(1-t)^\alpha}{\alpha} \right)^\beta \right| dt$$

$$= \begin{cases} \frac{1}{\alpha^\beta} \left[\frac{7}{12} - \frac{1}{\alpha} \mathfrak{B}\left(\frac{1}{\alpha}, \beta+1, \left(\frac{2}{3}\right)^\alpha \right) \right] & \beta < \frac{\ln\left(\frac{7}{8}\right)}{\ln\left(1-\left(\frac{2}{3}\right)^\alpha\right)} \\[4mm] \frac{1}{\alpha^\beta} \left[\frac{21C-14}{12} + \frac{1}{\alpha} \left(2\mathfrak{B}\left(\frac{1}{\alpha}, \beta+1, 1-\left(\frac{7}{8}\right)^{\frac{1}{\beta}} \right) - \mathfrak{B}\left(\frac{1}{\alpha}, \beta+1, \left(\frac{2}{3}\right)^\alpha \right) \right) \right] & \beta > \frac{\ln\left(\frac{7}{8}\right)}{\ln\left(1-\left(\frac{2}{3}\right)^\alpha\right)} \end{cases}$$

with $T = 1 - \left(1-\left(\frac{1}{8}\right)^{\frac{1}{\beta}}\right)^{\frac{1}{\alpha}}$, $K = 1 - \left(1-\left(\frac{1}{2}\right)^{\frac{1}{\beta}}\right)^{\frac{1}{\alpha}}$, $C = 1 - \left(1-\left(\frac{7}{8}\right)^{\frac{1}{\beta}}\right)^{\frac{1}{\alpha}}$ *and B is the Beta function and $\mathfrak{B}$ is the incomplete Beta function.*

Proof. Consider modulus in Lemma 3.1. Then, we obtain the following inequality

$$\left| \frac{\left[\mathfrak{h}(\sigma).\mathfrak{h}\left(\frac{2\sigma+\delta}{3}\right)^3.\mathfrak{h}\left(\frac{\sigma+2\delta}{3}\right)^3.\mathfrak{h}(\delta) \right]^{\frac{1}{8}}}{\left[{}_*^\beta\mathscr{I}_\delta^\alpha \mathfrak{h}(\sigma).{}_\sigma^\beta\mathscr{I}_*^\alpha \mathfrak{h}(\delta) \right]^{\frac{\alpha^\beta \Gamma(\beta+1)}{2(\delta-\sigma)\alpha^\beta}}} \right| \tag{4.1}$$

$$\leq \exp\left\{ \frac{\alpha^\beta(\delta-\sigma)}{2} \int_0^{\frac{1}{3}} \left| \left(\frac{1-(1-t)^\alpha}{\alpha} \right)^\beta - \frac{1}{8\alpha^\beta} \right| |\ln \mathfrak{h}^*(t\delta+(1-t)\sigma)| dt \right\}$$

$$\times \exp\left\{ \frac{\alpha^\beta(\delta-\sigma)}{2} \int_0^{\frac{1}{3}} \left| \frac{1}{8\alpha^\beta} - \left(\frac{1-(1-t)^\alpha}{\alpha} \right)^\beta \right| |\ln \mathfrak{h}^*(t\sigma+(1-t)\delta)| dt \right\}$$

$$\times \exp\left\{ \frac{\alpha^\beta(\delta-\sigma)}{2} \int_{\frac{1}{3}}^{\frac{2}{3}} \left| \left(\frac{1-(1-t)^\alpha}{\alpha} \right)^\beta - \frac{1}{2\alpha^\beta} \right| |\ln \mathfrak{h}^*(t\delta+(1-t)\sigma)| dt \right\}$$

$$\times \exp\left\{ \frac{\alpha^\beta(\delta-\sigma)}{2} \int_{\frac{1}{3}}^{\frac{2}{3}} \left| \frac{1}{2\alpha^\beta} - \left(\frac{1-(1-t)^\alpha}{\alpha} \right)^\beta \right| |\ln \mathfrak{h}^*(t\sigma+(1-t)\delta)| dt \right\}$$

$$\times \exp\left\{ \frac{\alpha^\beta(\delta-\sigma)}{2} \int_{\frac{2}{3}}^{1} \left| \left(\frac{1-(1-t)^\alpha}{\alpha}\right)^\beta - \frac{7}{8\alpha^\beta}\right| |\ln \mathfrak{h}^*(t\delta+(1-t)\sigma)| \, dt\right\}$$

$$\times \exp\left\{ \frac{\alpha^\beta(\delta-\sigma)}{2} \int_{\frac{2}{3}}^{1} \left| \frac{7}{8\alpha^\beta} - \left(\frac{1-(1-t)^\alpha}{\alpha}\right)^\beta\right| |\ln \mathfrak{h}^*(t\sigma+(1-t)\delta)| \, dt\right\}.$$

Leveraging the multiplicatively convex characteristic of $\mathfrak{h}^*$ on the domain $[\sigma, \delta]$, we can subsequently infer

$$|\ln \mathfrak{h}^*(t\delta+(1-t)\sigma)| \leq t\ln \mathfrak{h}^*(\delta) + (1-t)\ln \mathfrak{h}^*(\sigma) \tag{4.2}$$

and

$$|\ln \mathfrak{h}^*(t\sigma+(1-t)\delta)| \leq t\ln \mathfrak{h}^*(\sigma) + (1-t)\ln \mathfrak{h}^*(\delta) \tag{4.3}$$

for all $t \in [0,1]$. When the inequalities (4.2) and (4.3) are applied to (4.1), we obtain following inequality:

$$\left| \frac{\left[\mathfrak{h}(\sigma).\mathfrak{h}\left(\frac{2\sigma+\delta}{3}\right)^3.\mathfrak{h}\left(\frac{\sigma+2\delta}{3}\right)^3.\mathfrak{h}(\delta)\right]^{\frac{1}{8}}}{\left[{}^\beta_*\mathscr{I}^\alpha_\delta \mathfrak{h}(\sigma).{}^\beta_\sigma\mathscr{I}^\alpha_* \mathfrak{h}(\delta)\right]^{\frac{\alpha^\beta\Gamma(\beta+1)}{2(\delta-\sigma)^{\alpha\beta}}}} \right|$$

$$\leq \exp\left\{ \frac{\alpha^\beta(\delta-\sigma)}{2} \int_{0}^{\frac{1}{3}} \left| \left(\frac{1-(1-t)^\alpha}{\alpha}\right)^\beta - \frac{1}{8\alpha^\beta}\right| (t\ln \mathfrak{h}^*(\delta) + (1-t)\ln \mathfrak{h}^*(\sigma)) \, dt\right\}$$

$$\times \exp\left\{ \frac{\alpha^\beta(\delta-\sigma)}{2} \int_{0}^{\frac{1}{3}} \left| \frac{1}{8\alpha^\beta} - \left(\frac{1-(1-t)^\alpha}{\alpha}\right)^\beta\right| (t\ln \mathfrak{h}^*(\sigma) + (1-t)\ln \mathfrak{h}^*(\delta)) \, dt\right\}$$

$$\times \exp\left\{ \frac{\alpha^\beta(\delta-\sigma)}{2} \int_{\frac{1}{3}}^{\frac{2}{3}} \left| \left(\frac{1-(1-t)^\alpha}{\alpha}\right)^\beta - \frac{1}{2\alpha^\beta}\right| (t\ln \mathfrak{h}^*(\delta) + (1-t)\ln \mathfrak{h}^*(\sigma)) \, dt\right\}$$

$$\times \exp\left\{ \frac{\alpha^\beta(\delta-\sigma)}{2} \int_{\frac{1}{3}}^{\frac{2}{3}} \left| \frac{1}{2\alpha^\beta} - \left(\frac{1-(1-t)^\alpha}{\alpha}\right)^\beta\right| (t\ln \mathfrak{h}^*(\sigma) + (1-t)\ln \mathfrak{h}^*(\delta)) \, dt\right\}$$

$$\times \exp\left\{ \frac{\alpha^\beta(\delta-\sigma)}{2} \int_{\frac{2}{3}}^{1} \left| \left(\frac{1-(1-t)^\alpha}{\alpha}\right)^\beta - \frac{7}{8\alpha^\beta}\right| (t\ln \mathfrak{h}^*(\delta) + (1-t)\ln \mathfrak{h}^*(\sigma)) \, dt\right\}$$

$$\times \exp\left\{ \frac{\alpha^\beta(\delta-\sigma)}{2} \int_{\frac{2}{3}}^{1} \left| \frac{7}{8\alpha^\beta} - \left(\frac{1-(1-t)^\alpha}{\alpha}\right)^\beta\right| (t\ln \mathfrak{h}^*(\sigma) + (1-t)\ln \mathfrak{h}^*(\delta)) \, dt\right\}$$

$$= \exp\left\{ \frac{\alpha^\beta(\delta-\sigma)}{2} \int_{0}^{\frac{1}{3}} \left| \left(\frac{1-(1-t)^\alpha}{\alpha}\right)^\beta - \frac{1}{8\alpha^\beta}\right| \ln \mathfrak{h}^*(\delta)\,(t+1-t) \, dt\right\}$$

$$\times \exp\left\{ \frac{\alpha^\beta(\delta-\sigma)}{2} \int_{0}^{\frac{1}{3}} \left| \frac{1}{8\alpha^\beta} - \left(\frac{1-(1-t)^\alpha}{\alpha}\right)^\beta\right| \ln \mathfrak{h}^*(\sigma)\,(t+1-t) \, dt\right\}$$

$$\times \exp\left\{ \frac{\alpha^\beta(\delta-\sigma)}{2} \int_{\frac{1}{3}}^{\frac{2}{3}} \left| \left(\frac{1-(1-t)^\alpha}{\alpha}\right)^\beta - \frac{1}{2\alpha^\beta}\right| \ln \mathfrak{h}^*(\delta)\,(t+1-t) \, dt\right\}$$

$$\times \exp\left\{ \frac{\alpha^\beta(\delta-\sigma)}{2} \int_{\frac{1}{3}}^{\frac{2}{3}} \left| \frac{1}{2\alpha^\beta} - \left(\frac{1-(1-t)^\alpha}{\alpha}\right)^\beta\right| \ln \mathfrak{h}^*(\sigma)\,(t+1-t) \, dt\right\}$$

$$\times \exp\left\{ \frac{\alpha^\beta(\delta-\sigma)}{2} \int_{\frac{2}{3}}^{1} \left| \left(\frac{1-(1-t)^\alpha}{\alpha}\right)^\beta - \frac{7}{8\alpha^\beta}\right| \ln \mathfrak{h}^*(\delta)\,(t+1-t) \, dt\right\}$$

$$\times \exp\left\{ \frac{\alpha^\beta(\delta-\sigma)}{2} \int_{\frac{2}{3}}^{1} \left| \frac{7}{8\alpha^\beta} - \left(\frac{1-(1-t)^\alpha}{\alpha}\right)^\beta\right| \ln \mathfrak{h}^*(\sigma)\,(t+1-t) \, dt\right\}$$

$$= \exp\left\{\frac{\alpha^{\beta}(\delta-\sigma)}{2}\left(\ln\mathfrak{h}^{*}(\sigma)+\ln\mathfrak{h}^{*}(\delta)\right)\int_{0}^{\frac{1}{3}}\left|\frac{1}{8\alpha^{\beta}}-\left(\frac{1-(1-t)^{\alpha}}{\alpha}\right)^{\beta}\right|dt\right\}$$

$$\times\exp\left\{\frac{\alpha^{\beta}(\delta-\sigma)}{2}\left(\ln\mathfrak{h}^{*}(\sigma)+\ln\mathfrak{h}^{*}(\delta)\right)\int_{\frac{1}{3}}^{\frac{2}{3}}\left|\frac{1}{2\alpha^{\beta}}-\left(\frac{1-(1-t)^{\alpha}}{\alpha}\right)^{\beta}\right|dt\right\}$$

$$\times\exp\left\{\frac{\alpha^{\beta}(\delta-\sigma)}{2}\left(\ln\mathfrak{h}^{*}(\sigma)+\ln\mathfrak{h}^{*}(\delta)\right)\int_{\frac{2}{3}}^{1}\left|\frac{7}{8\alpha^{\beta}}-\left(\frac{1-(1-t)^{\alpha}}{\alpha}\right)^{\beta}\right|dt\right\}$$

$$= \exp\left\{\left(\ln\mathfrak{h}^{*}(\sigma)+\ln\mathfrak{h}^{*}(\delta)\right)\frac{\alpha^{\beta}(\delta-\sigma)}{2}\left[\Psi_{1}\left(\alpha,\beta\right)+\Psi_{2}\left(\alpha,\beta\right)+\Psi_{3}\left(\alpha,\beta\right)\right]\right\}$$

$$= \left[\mathfrak{h}^{*}(\sigma)\mathfrak{h}^{*}(\delta)\right]^{\frac{\alpha^{\beta}(\delta-\sigma)}{2}\left[\Psi_{1}(\alpha,\beta)+\Psi_{2}(\alpha,\beta)+\Psi_{3}(\alpha,\beta)\right]}.$$

This is the end of the proof of Theorem 4.1.   □

Remark 4.2. *Picking* $\alpha=1$ *in Theorem 4.1 gives the subsequent inequality of Newton-type for MRLFI:*

$$\left|\frac{\left[\mathfrak{h}(\sigma).\mathfrak{h}\left(\frac{2\sigma+\delta}{3}\right)^{3}.\mathfrak{h}\left(\frac{\sigma+2\delta}{3}\right)^{3}.\mathfrak{h}(\delta)\right]^{\frac{1}{8}}}{\left[{}_{*}I^{\beta}_{\frac{\sigma+\delta}{2}}\mathfrak{h}(\sigma).\frac{\sigma+\delta}{2}I^{\beta}_{*}\mathfrak{h}(\delta)\right]^{\frac{\Gamma(\beta+1)}{2(\delta-\sigma)^{\beta}}}}\right|\leq\left[\mathfrak{h}^{*}(\sigma)\mathfrak{h}^{*}(\delta)\right]^{\frac{(\delta-\sigma)}{2}\left[\Upsilon_{1}(\beta)+\Upsilon_{2}(\beta)+\Upsilon_{3}(\beta)\right]}.$$

Here

$$\Upsilon_{1}\left(\beta\right) = \int_{0}^{\frac{1}{3}}\left|t^{\beta}-\frac{1}{8}\right|dt$$

$$= \begin{cases} \dfrac{2\beta}{8^{\frac{\beta+1}{\beta}}}+\dfrac{1}{3^{\beta+1}(\beta+1)}-\dfrac{1}{24}, & 0<\beta\leq\dfrac{\ln\left(\frac{1}{8}\right)}{\ln\left(\frac{1}{3}\right)}, \\[4mm] \dfrac{1}{24}-\dfrac{1}{3^{\beta+1}(\beta+1)}, & \beta>\dfrac{\ln\left(\frac{1}{8}\right)}{\ln\left(\frac{1}{3}\right)}, \end{cases}$$

$$\Upsilon_{2}\left(\beta\right) = \int_{\frac{1}{3}}^{\frac{2}{3}}\left|t^{\beta}-\frac{1}{2}\right|dt$$

$$= \begin{cases} \dfrac{2^{\beta+1}-1}{3^{\beta+1}(\beta+1)}-\dfrac{1}{6}, & \beta<\dfrac{\ln\left(\frac{1}{2}\right)}{\ln\left(\frac{1}{3}\right)}, \\[4mm] \dfrac{\beta}{2^{\frac{1}{\beta}}(\beta+1)}+\dfrac{2^{\beta+1}+1}{3^{\beta+1}(\beta+1)}-\dfrac{1}{2}, & \dfrac{\ln\left(\frac{1}{2}\right)}{\ln\left(\frac{1}{3}\right)}<\beta<\dfrac{\ln\left(\frac{1}{2}\right)}{\ln\left(\frac{2}{3}\right)}, \\[4mm] \dfrac{1}{6}-\dfrac{2^{\beta+1}-1}{3^{\beta+1}(\beta+1)}, & \beta>\dfrac{\ln\left(\frac{1}{2}\right)}{\ln\left(\frac{2}{3}\right)}, \end{cases}$$

and

$$\Upsilon_{3}\left(\beta\right) = \int_{\frac{2}{3}}^{1}\left|t^{\beta}-\frac{7}{8}\right|dt$$

$$= \begin{cases} \dfrac{2\beta 7^{\frac{\beta+1}{\beta}}}{8^{\frac{\beta+1}{\beta}}(\beta+1)}+\dfrac{3^{\beta+1}+2^{\beta+1}}{3^{\beta+1}(\beta+1)}-\dfrac{35}{24}, & \beta>\dfrac{\ln\left(\frac{7}{8}\right)}{\ln\left(\frac{2}{3}\right)}, \\[4mm] \dfrac{3^{\beta+1}-2^{\beta+1}}{3^{\beta+1}(\beta+1)}-\dfrac{7}{24}, & 0<\beta<\dfrac{\ln\left(\frac{7}{8}\right)}{\ln\left(\frac{2}{3}\right)}. \end{cases}$$

This result is the sam with [37, Theorem 5.1].

Remark 4.3. *If we take* $\alpha=\beta=1$ *in Theorem 4.1, we obtain the following inequality of Newton-type:*

$$\left|\left[\mathfrak{h}(\sigma)\left[\mathfrak{h}\left(\frac{\sigma+2\delta}{3}\right)\right]^{3}\left[\mathfrak{h}\left(\frac{2\sigma+\delta}{3}\right)\right]^{3}\mathfrak{h}(\delta)\right]^{\frac{1}{8}}\left(\int_{\sigma}^{\delta}(\mathfrak{h}(t))^{dt}\right)^{\frac{1}{\sigma-\delta}}\right|\leq\left(\mathfrak{h}^{*}(\sigma)\mathfrak{h}^{*}(\delta)\right)^{\frac{25(\delta-\sigma)}{576}},$$

which is presented by Chasreechai et al. in [27, Theorem 5.1].

Theorem 4.4. *Assume that all conditions of Lemma 3.1 are satisfy. Let also $\mathfrak{h} : [\sigma, \delta] \to \mathbb{R}^+$ be an increasing function on $[\sigma, \delta]$. If $(\ln \mathfrak{h}^*)^q$ is a convex on $[\sigma, \delta]$ with $q > 1$ and $\frac{1}{p} + \frac{1}{q} = 1$, then, for $\beta > 0$ and $\alpha \in (0, 1]$, we have the following inequality:*

$$
\left| \frac{\left[\mathfrak{h}(\sigma).\mathfrak{h}\left(\frac{2\sigma+\delta}{3}\right)^3.\mathfrak{h}\left(\frac{\sigma+2\delta}{3}\right)^3.\mathfrak{h}(\delta) \right]^{\frac{1}{8}}}{\left[{}^{\beta}_{*}\mathscr{I}^{\alpha}_{\delta}\mathfrak{h}(\sigma).{}^{\beta}_{\sigma}\mathscr{I}^{\alpha}_{*}\mathfrak{h}(\delta) \right]^{\frac{\alpha^{\beta}\Gamma(\beta+1)}{2(\delta-\sigma)\alpha\beta}}} \right|
$$
$$
\leq \quad [\mathfrak{h}^*(\sigma)\mathfrak{h}^*(\delta)]^{\frac{\alpha^{\beta}(\delta-\sigma)}{6}} \left[[18\Psi_4(\alpha,\beta)]^{\frac{1}{p}} + [6\Psi_5(\alpha,\beta)]^{\frac{1}{p}} + [18\Psi_6(\alpha,\beta)]^{\frac{1}{p}} \right].
$$

Here

$$
\Psi_4(\alpha,\beta) = \int_0^{\frac{1}{3}} \left| \frac{1}{8\alpha^{\beta}} - \left(\frac{1-(1-t)^{\alpha}}{\alpha} \right)^{\beta} \right|^p dt,
$$

$$
\Psi_5(\alpha,\beta) = \int_{\frac{1}{3}}^{\frac{2}{3}} \left| \frac{1}{2\alpha^{\beta}} - \left(\frac{1-(1-t)^{\alpha}}{\alpha} \right)^{\beta} \right|^p dt,
$$

$$
\Psi_6(\alpha,\beta) = \int_{\frac{2}{3}}^{1} \left| \frac{7}{8\alpha^{\beta}} - \left(\frac{1-(1-t)^{\alpha}}{\alpha} \right)^{\beta} \right|^p dt.
$$

Proof. Taking advantage of Lemma 3.1, it follows that

$$
\left| \frac{\left[\mathfrak{h}(\sigma).\mathfrak{h}\left(\frac{2\sigma+\delta}{3}\right)^3.\mathfrak{h}\left(\frac{\sigma+2\delta}{3}\right)^3.\mathfrak{h}(\delta) \right]^{\frac{1}{8}}}{\left[{}^{\beta}_{*}\mathscr{I}^{\alpha}_{\delta}\mathfrak{h}(\sigma).{}^{\beta}_{\sigma}\mathscr{I}^{\alpha}_{*}\mathfrak{h}(\delta) \right]^{\frac{\alpha^{\beta}\Gamma(\beta+1)}{2(\delta-\sigma)\alpha\beta}}} \right|
$$
$$
\leq \exp\left\{ \frac{\alpha^{\beta}(\delta-\sigma)}{2} \int_0^{\frac{1}{3}} \left| \frac{1}{8\alpha^{\beta}} - \left(\frac{1-(1-t)^{\alpha}}{\alpha} \right)^{\beta} \right| [|\ln \mathfrak{h}^*(t\delta+(1-t)\sigma)| + |\ln \mathfrak{h}^*(t\sigma+(1-t)\delta)|] dt \right\}
$$
$$
\times \exp\left\{ \frac{\alpha^{\beta}(\delta-\sigma)}{2} \int_{\frac{1}{3}}^{\frac{2}{3}} \left| \frac{1}{2\alpha^{\beta}} - \left(\frac{1-(1-t)^{\alpha}}{\alpha} \right)^{\beta} \right| [|\ln \mathfrak{h}^*(t\delta+(1-t)\sigma)| + |\ln \mathfrak{h}^*(t\sigma+(1-t)\delta)|] dt \right\}
$$
$$
\times \exp\left\{ \frac{\alpha^{\beta}(\delta-\sigma)}{2} \int_{\frac{2}{3}}^{1} \left| \frac{7}{8\alpha^{\beta}} - \left(\frac{1-(1-t)^{\alpha}}{\alpha} \right)^{\beta} \right| [|\ln \mathfrak{h}^*(t\delta+(1-t)\sigma)| + |\ln \mathfrak{h}^*(t\sigma+(1-t)\delta)|] dt \right\}.
$$

In terms of the Hölder's inequality, we have

$$
\left| \frac{\left[\mathfrak{h}(\sigma).\mathfrak{h}\left(\frac{2\sigma+\delta}{3}\right)^3.\mathfrak{h}\left(\frac{\sigma+2\delta}{3}\right)^3.\mathfrak{h}(\delta) \right]^{\frac{1}{8}}}{\left[{}^{\beta}_{*}\mathscr{I}^{\alpha}_{\delta}\mathfrak{h}(\sigma).{}^{\beta}_{\sigma}\mathscr{I}^{\alpha}_{*}\mathfrak{h}(\delta) \right]^{\frac{\alpha^{\beta}\Gamma(\beta+1)}{2(\delta-\sigma)\alpha\beta}}} \right| \tag{4.4}
$$
$$
\leq \exp\left\{ \frac{\alpha^{\beta}(\delta-\sigma)}{2} \left(\int_0^{\frac{1}{3}} \left| \frac{1}{8\alpha^{\beta}} - \left(\frac{1-(1-t)^{\alpha}}{\alpha} \right)^{\beta} \right|^p dt \right)^{\frac{1}{p}} \left[\left(\int_0^{\frac{1}{3}} |\ln \mathfrak{h}^*(t\delta+(1-t)\sigma)|^q dt \right)^{\frac{1}{q}} \right. \right.
$$
$$
\left. \left. + \left(\int_0^{\frac{1}{3}} |\ln \mathfrak{h}^*(t\sigma+(1-t)\delta)|^q dt \right)^{\frac{1}{q}} \right] \right\}
$$
$$
\times \exp\left\{ \frac{\alpha^{\beta}(\delta-\sigma)}{2} \left(\int_{\frac{1}{3}}^{\frac{2}{3}} \left| \frac{1}{2\alpha^{\beta}} - \left(\frac{1-(1-t)^{\alpha}}{\alpha} \right)^{\beta} \right|^p dt \right)^{\frac{1}{p}} \left[\left(\int_{\frac{1}{3}}^{\frac{2}{3}} |\ln \mathfrak{h}^*(t\delta+(1-t)\sigma)|^q dt \right)^{\frac{1}{q}} \right. \right.
$$
$$
\left. \left. + \left(\int_{\frac{1}{3}}^{\frac{2}{3}} |\ln \mathfrak{h}^*(t\sigma+(1-t)\delta)|^q dt \right)^{\frac{1}{q}} \right] \right\}
$$

$$\times \exp \left\{ \begin{array}{c} \dfrac{\alpha^{\beta}(\delta-\sigma)}{2} \left(\displaystyle\int_{\frac{2}{3}}^{1} \left| \dfrac{7}{8\alpha^{\beta}} - \left(\dfrac{1-(1-t)^{\alpha}}{\alpha} \right)^{\beta} \right|^{p} dt \right)^{\frac{1}{p}} \left[\left(\displaystyle\int_{\frac{2}{3}}^{1} |\ln \mathfrak{h}^{*}(t\delta+(1-t)\sigma)|^{q} dt \right)^{\frac{1}{q}} \right. \\ \left. + \left(\displaystyle\int_{\frac{2}{3}}^{1} |\ln \mathfrak{h}^{*}(t\sigma+(1-t)\delta)|^{q} dt \right)^{\frac{1}{q}} \right] \end{array} \right\}.$$

Using the convexity of $(\ln \mathfrak{h}^{*})^{q}$, we get

$$\int_{0}^{\frac{1}{3}} |\ln \mathfrak{h}^{*}(t\delta+(1-t)\sigma)|^{q} dt \quad \leq \quad \int_{0}^{\frac{1}{3}} \left[t(\ln \mathfrak{h}^{*}(\delta))^{q} + (1-t)(\ln \mathfrak{h}^{*}(\sigma))^{q} \right] dt \tag{4.5}$$

$$= \quad \frac{1}{18}(\ln \mathfrak{h}^{*}(\delta))^{q} + \frac{5}{18}(\ln \mathfrak{h}^{*}(\sigma))^{q}.$$

Similarly, we have

$$\int_{0}^{\frac{1}{3}} |\ln \mathfrak{h}^{*}(t\sigma+(1-t)\delta)|^{q} dt \quad \leq \quad \frac{1}{18}(\ln \mathfrak{h}^{*}(\sigma))^{q} + \frac{5}{18}(\ln \mathfrak{h}^{*}(\delta))^{q},$$

$$\int_{\frac{1}{3}}^{\frac{2}{3}} |\ln \mathfrak{h}^{*}(t\delta+(1-t)\sigma)|^{q} dt \quad \leq \quad \frac{1}{6}(\ln \mathfrak{h}^{*}(\delta))^{q} + \frac{1}{6}(\ln \mathfrak{h}^{*}(\sigma))^{q},$$

$$\int_{\frac{1}{3}}^{\frac{2}{3}} |\ln \mathfrak{h}^{*}(t\sigma+(1-t)\delta)|^{q} dt \quad \leq \quad \frac{1}{6}(\ln \mathfrak{h}^{*}(\sigma))^{q} + \frac{1}{6}(\ln \mathfrak{h}^{*}(\delta))^{q},$$

$$\int_{\frac{2}{3}}^{1} |\ln \mathfrak{h}^{*}(t\delta+(1-t)\sigma)|^{q} dt \quad \leq \quad \frac{5}{18}(\ln \mathfrak{h}^{*}(\delta))^{q} + \frac{1}{18}(\ln \mathfrak{h}^{*}(\sigma))^{q},$$

$$\int_{\frac{2}{3}}^{1} |\ln \mathfrak{h}^{*}(t\sigma+(1-t)\delta)|^{q} dt \quad \leq \quad \frac{5}{18}(\ln \mathfrak{h}^{*}(\sigma))^{q} + \frac{1}{18}(\ln \mathfrak{h}^{*}(\delta))^{q}. \tag{4.6}$$

If we apply the formulas from (4.5) to (4.6) into the inequality (4.4), then we obtain that

$$\left| \frac{\left[\mathfrak{h}(\sigma).\mathfrak{h}\left(\frac{2\sigma+\delta}{3}\right)^{3}.\mathfrak{h}\left(\frac{\sigma+2\delta}{3}\right)^{3}.\mathfrak{h}(\delta) \right]^{\frac{1}{8}}}{\left[{}_{*}^{\beta}\mathscr{I}_{\delta}^{\alpha}\mathfrak{h}(\sigma).{}_{\sigma}^{\beta}\mathscr{I}_{*}^{\alpha}\mathfrak{h}(\delta) \right]^{\frac{\alpha^{\beta}\Gamma(\beta+1)}{2(\delta-\sigma)^{\alpha\beta}}}} \right| \tag{4.7}$$

$$\leq \quad \exp \left\{ \frac{\alpha^{\beta}(\delta-\sigma)}{2} \left(\int_{0}^{\frac{1}{3}} \left| \frac{1}{8\alpha^{\beta}} - \left(\frac{1-(1-t)^{\alpha}}{\alpha} \right)^{\beta} \right|^{p} dt \right)^{\frac{1}{p}} \left[\left(\frac{(\ln \mathfrak{h}^{*}(\delta))^{q}+5(\ln \mathfrak{h}^{*}(\sigma))^{q}}{18} \right)^{\frac{1}{q}} \right. \right.$$
$$\left. \left. + \left(\frac{(\ln \mathfrak{h}^{*}(\sigma))^{q}+5(\ln \mathfrak{h}^{*}(\delta))^{q}}{18} \right)^{\frac{1}{q}} \right] \right\}$$

$$\times \exp \left\{ \frac{\alpha^{\beta}(\delta-\sigma)}{2} \left(\int_{\frac{1}{3}}^{\frac{2}{3}} \left| \frac{1}{2\alpha^{\beta}} - \left(\frac{1-(1-t)^{\alpha}}{\alpha} \right)^{\beta} \right|^{p} dt \right)^{\frac{1}{p}} \left[\left(\frac{(\ln \mathfrak{h}^{*}(\delta))^{q}+(\ln \mathfrak{h}^{*}(\sigma))^{q}}{6} \right)^{\frac{1}{q}} \right. \right.$$
$$\left. \left. + \left(\frac{(\ln \mathfrak{h}^{*}(\sigma))^{q}+(\ln \mathfrak{h}^{*}(\delta))^{q}}{6} \right)^{\frac{1}{q}} \right] \right\}$$

$$\times \exp \left\{ \frac{\alpha^{\beta}(\delta-\sigma)}{2} \left(\int_{\frac{2}{3}}^{1} \left| \frac{7}{8\alpha^{\beta}} - \left(\frac{1-(1-t)^{\alpha}}{\alpha} \right)^{\beta} \right|^{p} dt \right)^{\frac{1}{p}} \left[\left(\frac{5(\ln \mathfrak{h}^{*}(\delta))^{q}+(\ln \mathfrak{h}^{*}(\sigma))^{q}}{18} \right)^{\frac{1}{q}} \right. \right.$$
$$\left. \left. + \left(\frac{5(\ln \mathfrak{h}^{*}(\sigma))^{q}+(\ln \mathfrak{h}^{*}(\delta))^{q}}{18} \right)^{\frac{1}{q}} \right] \right\}.$$

It is known that

$$\sum_{k=1}^{n}(\sigma_{k}+\delta_{k})^{p} \leq \sum_{k=1}^{n}(\sigma_{k})^{p} + \sum_{k=1}^{n}(\delta_{k})^{p} \tag{4.8}$$

for $0 \leq p < 1$ and $\sigma_{k} \geq 0, \delta_{k} \geq 0$ $(k=1,2,..,n)$. If we use the inequality (4.8) and the inequalities $\left(\frac{5^{\frac{1}{q}}+1}{2 \times 18^{\frac{1}{q}}} \right) \leq \frac{18^{\frac{1}{p}}}{6}$ and $\left(\frac{1}{6^{\frac{1}{q}}} \right) \leq \frac{6^{\frac{1}{p}}}{6}$ in the expression (4.7), we obtain

$$\left| \frac{\left[\mathfrak{h}(\sigma).\mathfrak{h}\left(\frac{2\sigma+\delta}{3}\right)^{3}.\mathfrak{h}\left(\frac{\sigma+2\delta}{3}\right)^{3}.\mathfrak{h}(\delta) \right]^{\frac{1}{8}}}{\left[{}_{*}^{\beta}\mathscr{I}_{\delta}^{\alpha}\mathfrak{h}(\sigma).{}_{\sigma}^{\beta}\mathscr{I}_{*}^{\alpha}\mathfrak{h}(\delta) \right]^{\frac{\alpha^{\beta}\Gamma(\beta+1)}{2(\delta-\sigma)^{\alpha\beta}}}} \right|$$

$$
\leq \quad \exp\left\{ \begin{array}{c} \frac{\alpha^\beta(\delta-\sigma)}{2}\left(\Psi_3\left(\alpha,\beta\right)\right)^{\frac{1}{p}}\left[\left(\frac{1}{18}\right)^{\frac{1}{q}}\ln\mathfrak{h}^*(\delta)+\left(\frac{5}{18}\right)^{\frac{1}{q}}\ln\mathfrak{h}^*(\sigma)\right. \\ \left. +\left(\frac{1}{18}\right)^{\frac{1}{q}}\ln\mathfrak{h}^*(\sigma)+\left(\frac{5}{18}\right)^{\frac{1}{q}}\ln\mathfrak{h}^*(\delta)\right] \end{array}\right\}
$$

$$
\times \exp\left\{ \begin{array}{c} \frac{\alpha^\beta(\delta-\sigma)}{2}\left(\Psi_4\left(\alpha,\beta\right)\right)^{\frac{1}{p}}\left[\left(\frac{1}{6}\right)^{\frac{1}{q}}\ln\mathfrak{h}^*(\delta)+\left(\frac{1}{6}\right)^{\frac{1}{q}}\ln\mathfrak{h}^*(\sigma)\right. \\ \left. +\left(\frac{1}{6}\right)^{\frac{1}{q}}\ln\mathfrak{h}^*(\sigma)+\left(\frac{1}{6}\right)^{\frac{1}{q}}\ln\mathfrak{h}^*(\delta)\right] \end{array}\right\}
$$

$$
\times \exp\left\{ \begin{array}{c} \frac{\alpha^\beta(\delta-\sigma)}{2}\left(\Psi_5\left(\alpha,\beta\right)\right)^{\frac{1}{p}}\left[\left(\frac{5}{18}\right)^{\frac{1}{q}}\ln\mathfrak{h}^*(\delta)+\left(\frac{1}{18}\right)^{\frac{1}{q}}\ln\mathfrak{h}^*(\sigma)\right. \\ \left. +\left(\frac{5}{18}\right)^{\frac{1}{q}}\ln\mathfrak{h}^*(\sigma)+\left(\frac{1}{18}\right)^{\frac{1}{q}}\ln\mathfrak{h}^*(\delta)\right] \end{array}\right\}
$$

$$
= \quad \exp\left\{(\ln\mathfrak{h}^*(\delta)+\ln\mathfrak{h}^*(\sigma))\frac{\alpha^\beta(\delta-\sigma)}{2}\left(\Psi_4\left(\alpha,\beta\right)\right)^{\frac{1}{p}}\left[\left(\frac{1}{18}\right)^{\frac{1}{q}}+\left(\frac{5}{18}\right)^{\frac{1}{q}}\right]\right\}
$$

$$
\times \exp\left\{(\ln\mathfrak{h}^*(\delta)+\ln\mathfrak{h}^*(\sigma))\frac{\alpha^\beta(\delta-\sigma)}{2}\left(\Psi_5\left(\alpha,\beta\right)\right)^{\frac{1}{p}}\left[\left(\frac{1}{6}\right)^{\frac{1}{q}}+\left(\frac{1}{6}\right)^{\frac{1}{q}}\right]\right\}
$$

$$
\times \exp\left\{(\ln\mathfrak{h}^*(\delta)+\ln\mathfrak{h}^*(\sigma))\frac{\alpha^\beta(\delta-\sigma)}{2}\left(\Psi_6\left(\alpha,\beta\right)\right)^{\frac{1}{p}}\left[\left(\frac{5}{18}\right)^{\frac{1}{q}}+\left(\frac{1}{18}\right)^{\frac{1}{q}}\right]\right\}
$$

$$
= \quad \left[\mathfrak{h}^*(\sigma)\mathfrak{h}^*(\delta)\right]^{\left(\left(\frac{5}{18}\right)^{\frac{1}{q}}+\left(\frac{1}{18}\right)^{\frac{1}{q}}\right)[\Psi_3(\alpha,\beta)]^{\frac{1}{p}}+\left(\left(\frac{1}{6}\right)^{\frac{1}{q}}+\left(\frac{1}{6}\right)^{\frac{1}{q}}\right)[\Psi_4(\alpha,\beta)]^{\frac{1}{p}}+\left(\left(\frac{5}{18}\right)^{\frac{1}{q}}+\left(\frac{1}{18}\right)^{\frac{1}{q}}[\Psi_5(\alpha,\beta)]^{\frac{1}{p}}\right)\right]^{\frac{\alpha^\beta(\delta-\sigma)}{2}}
$$

$$
\leq \quad \left[\mathfrak{h}^*(\sigma)\mathfrak{h}^*(\delta)\right]^{\frac{\alpha^\beta(\delta-\sigma)}{6}\left[18\Psi_4(\alpha,\beta)\right]^{\frac{1}{p}}+[6\Psi_5(\alpha,\beta)]^{\frac{1}{p}}+[18\Psi_6(\alpha,\beta)]^{\frac{1}{p}}}.
$$

This finalizes the proof. $\qquad\qquad\square$

Corollary 4.5. *Picking $\alpha=1$ in Theorem 4.4 gives the subsequent inequality of Newton-type for MRLFI:*

$$
\left| \frac{\left[\mathfrak{h}(\sigma).\mathfrak{h}\left(\frac{2\sigma+\delta}{3}\right)^3.\mathfrak{h}\left(\frac{\sigma+2\delta}{3}\right)^3.\mathfrak{h}(\delta)\right]^{\frac{1}{8}}}{\left[{}_*I_\delta^\beta\mathfrak{h}(\sigma).{}_\sigma I_*^\beta\mathfrak{h}(\delta)\right]^{\frac{\Gamma(\beta+1)}{2(\delta-\sigma)^\beta}}} \right|
$$

$$
\leq \quad \left[\mathfrak{h}^*(\sigma)\mathfrak{h}^*(\delta)\right]^{\frac{(\delta-\sigma)}{6}\left[18\Phi_1(\beta,p)\right]^{\frac{1}{p}}+[6\Phi_2(\beta,p)]^{\frac{1}{p}}+[18\Phi_3(\beta,p)]^{\frac{1}{p}}}.
$$

Here

$$
\Phi_1\left(\beta,p\right) \quad = \quad \int_0^{\frac{1}{3}}\left|\frac{1}{8}-t^\beta\right|^p dt,
$$

$$
\Phi_2(\beta,p) \quad = \quad \int_{\frac{1}{3}}^{\frac{2}{3}}\left|\frac{1}{2}-t^\beta\right|^p dt,
$$

$$
\Phi_3(\beta,p) \quad = \quad \int_{\frac{2}{3}}^1\left|\frac{7}{8}-t^\beta\right|^p dt.
$$

Corollary 4.6. *Assuming $\beta=1$ Remark 4.5 yields the next Newton-type inequality:*

$$
\left|\left[\mathfrak{h}(\sigma).\mathfrak{h}\left(\frac{2\sigma+\delta}{3}\right)^3.\mathfrak{h}\left(\frac{\sigma+2\delta}{3}\right)^3.\mathfrak{h}(\delta)\right]^{\frac{1}{8}}\left(\int_\sigma^\delta(\mathfrak{h}(t))^{dt}\right)^{\frac{-1}{\sigma-\delta}}\right| \leq \left[\mathfrak{h}^*(\sigma)\mathfrak{h}^*(\delta)\right]^{\frac{(\delta-\sigma)}{6}\left[18E_1\right]^{\frac{1}{p}}+[6E_2]^{\frac{1}{p}}+[18E_2]^{\frac{1}{p}}},
$$

where

$$
E_1 \quad = \quad \frac{1}{(p+1)}\left[\frac{1}{8^{p+1}}-\left(\frac{5}{24}\right)^{p+1}\right],
$$

$$
E_2 \quad = \quad \frac{2}{6^{p+1}(p+1)},
$$

$$
E_3 \quad = \quad \frac{5^{p+1}+1}{\left(24^{p+1}+8^{p+1}\right)(p+1)}.
$$

5. Newton-type Inequalities By Bounded Functions

In this section, we preesent some Newton-type inequalities for functions whose multiplicative derivatives are bounded.

Theorem 5.1. *Postulate that the constraints of Lemma 3.1 are satisfied. If there are $m, M \in \mathbb{R}^+$ so that $m \leq \mathfrak{h}^*(x) \leq M$ for all $x \in [\sigma, \delta]$, then we have the following Newton-type inequalities for MCFI*

$$\left| \frac{\left[\mathfrak{h}(\sigma).\mathfrak{h}\left(\frac{2\sigma+\delta}{3}\right)^3.\mathfrak{h}\left(\frac{\sigma+2\delta}{3}\right)^3.\mathfrak{h}(\delta) \right]^{\frac{1}{8}}}{\left[{}_*^\beta\mathscr{I}_\delta^\alpha\mathfrak{h}(\sigma).{}_\sigma^\beta\mathscr{I}_*^\alpha\mathfrak{h}(\delta) \right]^{\frac{\alpha^\beta\Gamma(\beta+1)}{2(\delta-\sigma)\alpha^\beta}}} \right| \leq \left(\frac{M}{m}\right)^{\frac{(\delta-\sigma)\alpha^\beta}{2}[\Psi_1(\alpha,\beta)+\Psi_2(\alpha,\beta)+\Psi_3(\alpha,\beta)]},$$

where Ψ_1, Ψ_2 and Ψ_3 are defined as in Theorem 4.1.

Proof. By using Lemma 3.1, we have

$$\frac{\left[\mathfrak{h}(\sigma).\mathfrak{h}\left(\frac{2\sigma+\delta}{3}\right)^3.\mathfrak{h}\left(\frac{\sigma+2\delta}{3}\right)^3.\mathfrak{h}(\delta) \right]^{\frac{1}{8}}}{\left[{}_*^\beta\mathscr{I}_\delta^\alpha\mathfrak{h}(\sigma).{}_\sigma^\beta\mathscr{I}_*^\alpha\mathfrak{h}(\delta) \right]^{\frac{\alpha^\beta\Gamma(\beta+1)}{2(\delta-\sigma)\alpha^\beta}}} \tag{5.1}$$

$$= \exp\left\{ \frac{\alpha^\beta(\delta-\sigma)}{2}\int_0^{\frac{1}{3}}\left(\left(\frac{1-(1-t)^\alpha}{\alpha}\right)^\beta - \frac{1}{8\alpha^\beta}\right)\left(\ln\mathfrak{h}^*(t\delta+(1-t)\sigma) - \frac{\ln M+\ln m}{2}\right)dt \right\}$$

$$\times \exp\left\{ \frac{\alpha^\beta(\delta-\sigma)}{2}\int_0^{\frac{1}{3}}\left(\frac{1}{8\alpha^\beta} - \left(\frac{1-(1-t)^\alpha}{\alpha}\right)^\beta\right)\left(\ln\mathfrak{h}^*(t\sigma+(1-t)\delta) - \frac{\ln M+\ln m}{2}\right)dt \right\}$$

$$\times \exp\left\{ \frac{\alpha^\beta(\delta-\sigma)}{2}\int_{\frac{1}{3}}^{\frac{2}{3}}\left(\left(\frac{1-(1-t)^\alpha}{\alpha}\right)^\beta - \frac{1}{2\alpha^\beta}\right)\left(\ln\mathfrak{h}^*(t\delta+(1-t)\sigma) - \frac{\ln M+\ln m}{2}\right)dt \right\}$$

$$\times \exp\left\{ \frac{\alpha^\beta(\delta-\sigma)}{2}\int_{\frac{1}{3}}^{\frac{2}{3}}\left(\frac{1}{2\alpha^\beta} - \left(\frac{1-(1-t)^\alpha}{\alpha}\right)^\beta\right)\left(\ln\mathfrak{h}^*(t\sigma+(1-t)\delta) - \frac{\ln M+\ln m}{2}\right)dt \right\}$$

$$\times \exp\left\{ \frac{\alpha^\beta(\delta-\sigma)}{2}\int_{\frac{2}{3}}^{1}\left(\left(\frac{1-(1-t)^\alpha}{\alpha}\right)^\beta - \frac{7}{8\alpha^\beta}\right)\left(\ln\mathfrak{h}^*(t\delta+(1-t)\sigma) - \frac{\ln M+\ln m}{2}\right)dt \right\}$$

$$\times \exp\left\{ \frac{\alpha^\beta(\delta-\sigma)}{2}\int_{\frac{2}{3}}^{1}\left(\frac{7}{8\alpha^\beta} - \left(\frac{1-(1-t)^\alpha}{\alpha}\right)^\beta\right)\left(\ln\mathfrak{h}^*(t\sigma+(1-t)\delta) - \frac{\ln M+\ln m}{2}\right)dt \right\}.$$

By using the absolute value of (5.1), we obtain

$$\left| \frac{\left[\mathfrak{h}(\sigma).\mathfrak{h}\left(\frac{2\sigma+\delta}{3}\right)^3.\mathfrak{h}\left(\frac{\sigma+2\delta}{3}\right)^3.\mathfrak{h}(\delta) \right]^{\frac{1}{8}}}{\left[{}_*^\beta\mathscr{I}_\delta^\alpha\mathfrak{h}(\sigma).{}_\sigma^\beta\mathscr{I}_*^\alpha\mathfrak{h}(\delta) \right]^{\frac{\alpha^\beta\Gamma(\beta+1)}{2(\delta-\sigma)\alpha^\beta}}} \right|$$

$$\leq \exp\left\{ \frac{\alpha^\beta(\delta-\sigma)}{2}\int_0^{\frac{1}{3}}\left|\left(\frac{1-(1-t)^\alpha}{\alpha}\right)^\beta - \frac{1}{8\alpha^\beta}\right|\left|\ln\mathfrak{h}^*(t\delta+(1-t)\sigma) - \frac{\ln M+\ln m}{2}\right|dt \right\}$$

$$\times \exp\left\{ \frac{\alpha^\beta(\delta-\sigma)}{2}\int_0^{\frac{1}{3}}\left|\frac{1}{8\alpha^\beta} - \left(\frac{1-(1-t)^\alpha}{\alpha}\right)^\beta\right|\left|\ln\mathfrak{h}^*(t\sigma+(1-t)\delta) - \frac{\ln M+\ln m}{2}\right|dt \right\}$$

$$\times \exp\left\{ \frac{\alpha^\beta(\delta-\sigma)}{2}\int_{\frac{2}{3}}^{\frac{2}{3}}\left|\left(\frac{1-(1-t)^\alpha}{\alpha}\right)^\beta - \frac{1}{2\alpha^\beta}\right|\left|\ln\mathfrak{h}^*(t\delta+(1-t)\sigma) - \frac{\ln M+\ln m}{2}\right|dt \right\}$$

$$\times \exp\left\{ \frac{\alpha^\beta(\delta-\sigma)}{2}\int_{\frac{1}{3}}^{\frac{2}{3}}\left|\frac{1}{2\alpha^\beta} - \left(\frac{1-(1-t)^\alpha}{\alpha}\right)^\beta\right|\left|\ln\mathfrak{h}^*(t\sigma+(1-t)\delta) - \frac{\ln M+\ln m}{2}\right|dt \right\}$$

$$\times \exp\left\{ \frac{\alpha^\beta(\delta-\sigma)}{2} \int_{\frac{2}{3}}^{1} \left| \left(\frac{1-(1-t)^\alpha}{\alpha} \right)^\beta - \frac{7}{8\alpha^\beta} \right| \left| \ln\mathfrak{h}^*(t\delta+(1-t)\sigma) - \frac{\ln M+\ln m}{2} \right| dt \right\}$$

$$\times \exp\left\{ \frac{\alpha^\beta(\delta-\sigma)}{2} \int_{\frac{2}{3}}^{1} \left| \frac{7}{8\alpha^\beta} - \left(\frac{1-(1-t)^\alpha}{\alpha} \right)^\beta \right| \left| \ln\mathfrak{h}^*(t\sigma+(1-t)\delta) - \frac{\ln M+\ln m}{2} \right| dt \right\}.$$

Since the function $\mathfrak{h}^*$ is bounded and the function ln is increasing, then the function $\ln\mathfrak{h}^*$ is bounded by $\ln m$ and $\ln M$. Thus we conclude

$$\left| \ln\mathfrak{h}^*\left(\frac{t}{2}\delta + \frac{2-t}{2}\sigma \right) - \frac{\ln M+\ln m}{2} \right| \le \frac{\ln M-\ln m}{2} \tag{5.2}$$

and

$$\left| \ln\mathfrak{h}^*\left(\frac{t}{2}\sigma + \frac{2-t}{2}\delta \right) - \frac{\ln M+\ln m}{2} \right| \le \frac{\ln M-\ln m}{2}. \tag{5.3}$$

If we consider (5.2) and (5.3), then we obtain

$$\left| \frac{\left[\mathfrak{h}(\sigma).\mathfrak{h}\left(\frac{2\sigma+\delta}{3} \right)^3 .\mathfrak{h}\left(\frac{\sigma+2\delta}{3} \right)^3 .\mathfrak{h}(\delta) \right]^{\frac{1}{8}}}{\left[{}_*^\beta\mathscr{I}_\delta^\alpha\mathfrak{h}(\sigma).{}_\sigma^\beta\mathscr{I}_*^\alpha\mathfrak{h}(\delta) \right]^{\frac{\alpha^\beta\Gamma(\beta+1)}{2(\delta-\sigma)\alpha^\beta}}} \right|$$

$$\le \exp\left\{ \frac{\alpha^\beta(\delta-\sigma)}{2} \left(\frac{\ln M-\ln m}{2} \right) \int_0^{\frac{1}{3}} \left| \left(\frac{1-(1-t)^\alpha}{\alpha} \right)^\beta - \frac{1}{8\alpha^\beta} \right| dt \right\}$$

$$\times \exp\left\{ \frac{\alpha^\beta(\delta-\sigma)}{2} \left(\frac{\ln M-\ln m}{2} \right) \int_0^{\frac{1}{3}} \left| \frac{1}{8\alpha^\beta} - \left(\frac{1-(1-t)^\alpha}{\alpha} \right)^\beta \right| dt \right\}$$

$$\times \exp\left\{ \frac{\alpha^\beta(\delta-\sigma)}{2} \left(\frac{\ln M-\ln m}{2} \right) \int_{\frac{1}{3}}^{\frac{2}{3}} \left| \left(\frac{1-(1-t)^\alpha}{\alpha} \right)^\beta - \frac{1}{2\alpha^\beta} \right| dt \right\}$$

$$\times \exp\left\{ \frac{\alpha^\beta(\delta-\sigma)}{2} \left(\frac{\ln M-\ln m}{2} \right) \int_{\frac{1}{3}}^{\frac{2}{3}} \left| \frac{1}{2\alpha^\beta} - \left(\frac{1-(1-t)^\alpha}{\alpha} \right)^\beta \right| dt \right\}$$

$$\times \exp\left\{ \frac{\alpha^\beta(\delta-\sigma)}{2} \left(\frac{\ln M-\ln m}{2} \right) \int_{\frac{2}{3}}^{1} \left| \left(\frac{1-(1-t)^\alpha}{\alpha} \right)^\beta - \frac{7}{8\alpha^\beta} \right| dt \right\}$$

$$\times \exp\left\{ \frac{\alpha^\beta(\delta-\sigma)}{2} \left(\frac{\ln M-\ln m}{2} \right) \int_{\frac{2}{3}}^{1} \left| \frac{7}{8\alpha^\beta} - \left(\frac{1-(1-t)^\alpha}{\alpha} \right)^\beta \right| dt \right\}$$

$$= \exp\left\{ \frac{\alpha^\beta(\delta-\sigma)}{2} (\ln M-\ln m) \left[\Psi_1(\alpha,\beta) + \Psi_2(\alpha,\beta) + \Psi_3(\alpha,\beta) \right] \right\}$$

$$= \left(\frac{M}{m} \right)^{\frac{(\delta-\sigma)\alpha^\beta}{2}[\Psi_1(\alpha,\beta)+\Psi_2(\alpha,\beta)+\Psi_3(\alpha,\beta)]}.$$

Here, we take advantage of Ψ_1-Ψ_3 as defined in Theorem 4.1. This ends the proof. $\qquad\square$

Corollary 5.2. *If we set $\alpha = 1$ in Theorem 5.1, we obtain the next Newton-type inequality with MRLFI:*

$$\left| \frac{\left[\mathfrak{h}(\sigma).\mathfrak{h}\left(\frac{2\sigma+\delta}{3} \right)^3 .\mathfrak{h}\left(\frac{\sigma+2\delta}{3} \right)^3 .\mathfrak{h}(\delta) \right]^{\frac{1}{8}}}{\left[{}_*I_\delta^\beta\mathfrak{h}(\sigma).{}_\sigma I_*^\beta\mathfrak{h}(\delta) \right]^{\frac{\Gamma(\beta+1)}{2(\delta-\sigma)^\beta}}} \right| \le \left(\frac{M}{m} \right)^{\frac{\delta-\sigma}{2}[\Upsilon_1(\beta)+\Upsilon_2(\beta)+\Upsilon_3(\beta)]}.$$

Here we take advantage of $\Upsilon_1(\beta), \Upsilon_2(\beta), \Upsilon_3(\beta)$ as defined Remark 4.2.

Corollary 5.3. *Setting $\beta = 1$ Corollary 5.2 gives the upcoming Newton-type inequality with multiplicative integrals:*

$$\left| \left[\mathfrak{h}(\sigma).\mathfrak{h}\left(\frac{2\sigma+\delta}{3} \right)^3 .\mathfrak{h}\left(\frac{\sigma+2\delta}{3} \right)^3 .\mathfrak{h}(\delta) \right]^{\frac{1}{8}} \left(\int_\sigma^\delta (\mathfrak{h}(t))^{dt} \right)^{\frac{-1}{\sigma-\delta}} \right| \le \left(\frac{M}{m} \right)^{\frac{25(\delta-\sigma)}{576}}.$$

6. Conclusion

In this study, a new Newton-type inequality form is derived for multiplicative conformable fractional integrals for multiplicatively convex functions. To obtain the main results, an important identity is first introduced. Using this identity along with MCFI, an innovative Newton-type inequality for multiplicative convex functions is presented. Furthermore, new Newton-type inequalities are obtained by incorporating bounded multiplicative derivatives. Future research may explore generalizing the results presented here to other types of multiplicative convex functions. Additionally, the method used in this study could be applied to different fractional integral operators, potentially leading to the development of new forms of Newton-type inequalities.

Article Information

References

[1] J. Gleick, *Isaac Newton*, Vintage, New York, 2007.
[2] G. W. Leibniz, *Gottfried Wilhelm Leibniz*, Leibniz-Forschungsstelle d. Univ. Münster, 1991.
[3] B. Belhoste, *Augustin-Louis Cauchy: A Biography*, Springer Science & Business Media, 2012.
[4] R. Bölling, Karl Weierstrass and some basic notions of the calculus, In: *The Second W. Killing and K. Weierstraß Colloquium*, Braniewo (Poland), March 2010, pp. 24–26.
[5] A. Plotnitsky, Bernhard Riemann, In: G. Jones (Ed.), *Deleuze's Philosophical Lineage*, Edinburgh University Press, 2009, pp. 190–208.
[6] S. C. Malik, S. Arora, *Mathematical Analysis*, New Age International, 1992.
[7] A. Browder, *Mathematical Analysis: An Introduction*, Springer Science & Business Media, 2012.
[8] C. P. Niculescu, *A new look at Newton's inequalities*, J. Inequal. Pure Appl. Math., **1**(2) (2000), Article ID 17.
[9] T. Sitthiwirattham, K. Nonlaopon, M. A. Ali, et al., *Riemann–Liouville fractional Newton's type inequalities for differentiable convex functions*, Fractal Fract., **6**(3) (2022), Article ID 175. https://doi.org/10.3390/fractalfract6030175
[10] F. Hezenci, H. Budak, *Fractional Newton-type integral inequalities by means of various function classes*, Math. Methods Appl. Sci., **48**(1) (2025), 1198–1215. https://doi.org/10.1002/mma.10378
[11] F. Hezenci, H. Budak, P. Kösem, *A new version of Newton's inequalities for Riemann–Liouville fractional integrals*, Rocky Mountain J. Math., **53**(1) (2023), 49–64. https://doi.org/10.1216/rmj.2023.53.49
[12] S. Iftikhar, P. Kumam, S. Erden, *Newton's-type integral inequalities via local fractional integrals*, Fractals, **28**(3) (2020), Article ID 2050037. https://doi.org/10.1142/S0218348X20500371
[13] C. Ünal, F. Hezenci, H. Budak, *Conformable fractional Newton-type inequalities with respect to differentiable convex functions*, J. Inequal. Appl., **2023**(1) (2023), Article ID 85. https://doi.org/10.1186/s13660-023-02996-0
[14] H. Xu, M. U. Awan, B. Meftah, et al., *On conformable fractional Newton-type inequalities*, Fractals, (2025), Early Access. https://doi.org/10.1142/s0218348x25500458
[15] F. Hezenci, H. Budak, *Note on Newton-type inequalities involving tempered fractional integrals*, Korean J. Math., **32**(2) (2024), 349–364. https://doi.org/10.11568/kjm.2024.32.2.349
[16] J. Soontharanon, M. A. Ali, H. Budak, et al., *Some new generalized fractional Newton's type inequalities for convex functions*, J. Funct. Spaces, **2022**(1) (2022), Article ID 6261970. https://doi.org/10.1155/2022/6261970
[17] M. A. Noor, K. I. Noor, S. Iftikhar, *Some Newton's type inequalities for harmonic convex functions*, J. Adv. Math. Stud., **9**(1) (2016), 7-16.
[18] S. Iftikhar, S. Erden, P. Kumam, et al., *Local fractional Newton's inequalities involving generalized harmonic convex functions*, Adv. Differ. Equ., **2020** (2020), Article ID 185, 1–14. https://doi.org/10.1186/s13662-020-02637-6
[19] W. Saleh, A. Lakhdari, T. Abdeljawad, et al., *On fractional biparameterized Newton-type inequalities*, J. Inequal. Appl., **2023**(1) (2023), Article ID 122. https://doi.org/10.1186/s13660-023-03033-w
[20] Y. Mahajan, H. Nagar, *Fractional Newton-type integral inequalities for the Caputo fractional operator*, Math. Methods Appl. Sci., **48**(4) (2025), 5244–5254. https://doi.org/10.1002/mma.10600
[21] M. A. Noor, K. I. Noor, S. Iftikhar, *Newton inequalities for p-harmonic convex functions*, Honam Math. J., **40**(2) (2018), 239–250. https://doi.org/10.5831/HMJ.2018.40.2.239
[22] D. Stanley, *A multiplicative calculus*, PRIMUS, **9**(4) (1999), 310–326. https://doi.org/10.1080/10511979908965937
[23] M. Grossman, *An introduction to non-Newtonian calculus*, Int. J. Math. Educ. Sci. Technol., **10**(4) (1979), 525–528. https://doi.org/10.1080/0020739790100406
[24] A. E. Bashirov, E. M. Kurpınar, A. Özyapıcı, *Multiplicative calculus and its applications*, J. Math. Anal. Appl., **337**(1) (2008), 36–48. https://doi.org/10.1016/j.jmaa.2007.03.081
[25] M. A. Ali, M. Abbas, Z. Zhang, et al., *On integral inequalities for product and quotient of two multiplicatively convex functions*, Asian Res. J. Math., **12**(3) (2019), 1–11. https://doi.org/10.9734/ARJOM/2019/V12I330084
[26] M. A. Ali, H. Budak, M. Z. Sarikaya, et al., *Ostrowski and Simpson type inequalities for multiplicative integrals*, Proyecciones (Antofagasta), **40**(3) (2021), 743–763. http://dx.doi.org/10.22199/issn.0717-6279-4136
[27] S. Chasreechai, M. A. Ali, S. Naowarat, et al., *On some Simpson's and Newton's type of inequalities in multiplicative calculus with applications*, AIMS Math., **8**(2) (2023), 3885–3896. https://doi.org/10.3934/math.2023193
[28] X. Zhan, A. Mateen, M. Toseef, et al., *Some Simpson- and Ostrowski-type integral inequalities for generalized convex functions in multiplicative calculus with their computational analysis*, Mathematics, **12**(11) (2024), Article ID 1721. https://doi.org/10.3390/math12111721
[29] B. Meftah, H. Boulares, A. Khan, et al., *Fractional multiplicative Ostrowski-type inequalities for multiplicative differentiable convex functions*, Jordan J. Math. Stat., **17**(1) (2024), 113–128.
[30] H. Boulares, B. Meftah, A. Moumen, et al.,*Fractional multiplicative Bullen-type inequalities for multiplicative differentiable functions*, Symmetry, **15**(2) (2023), Article ID 451. https://doi.org/10.3390/sym15020451
[31] A. Moumen, H. Boulares, B. Meftah, et al., *Multiplicatively Simpson type inequalities via fractional integral*, Symmetry, **15**(2) (2023), Article ID 460. https://doi.org/10.3390/sym15020460
[32] S. Özcan, *Hermite-Hadamard type inequalities for multiplicatively h-convex functions*, Konuralp J. Math., **8**(1) (2020), 158–164.
[33] A. Kashuri, S. K. Sahoo, M. Aljuaid, et al., *Some new Hermite–Hadamard type inequalities pertaining to generalized multiplicative fractional integrals*, Symmetry, **15**(4) (2023), Article ID 868. https://doi.org/10.3390/sym15040868

[34] B. Meftah, *Maclaurin type inequalities for multiplicatively convex functions*, Proc. Amer. Math. Soc., **151** (2023), 2115–2125. https://doi.org/10.1090/proc/16292

[35] T. Abdeljawad, M. Grossman, *On geometric fractional calculus*, J. Semigroup Theory Appl., **2016** (2016), Article ID 2, 14 pages.

[36] H. Budak, K. Özçelik, *On Hermite-Hadamard type inequalities for multiplicative fractional integrals*, Miskolc Math. Notes, **21**(1) (2020), 91–99. https://doi.org/10.18514/MMN.2020.3129

[37] M. A. Ali, *On Simpson's and Newton's type inequalities in multiplicative fractional calculus*, Filomat, **37**(30) (2023), 10133–10144. https://doi.org/10.2298/FIL2330133A

[38] T. Du, Y. Long, *The multi-parameterized integral inequalities for multiplicative Riemann–Liouville fractional integrals*, J. Math. Anal. Appl., **541**(1) (2025), Article ID 128692. https://doi.org/10.1016/j.jmaa.2024.128692

[39] D. Ai, T. Du, *A study on Newton-type inequalities bounds for twice differentiable functions under multiplicative Katugampola fractional integrals*, Fractals, **33**(5) (2025), Article ID 2550032. https://doi.org/10.1142/S0218348X2550032X

[40] A. Lakhdari, D. C. Benchettah, B. Meftah, *Fractional multiplicative Newton-type inequalities for multiplicative s-convex positive functions with application*, J. Comput. Appl. Math., **465** (2025), Article ID 116600. https://doi.org/10.1016/j.cam.2025.116600

[41] S. Özcan, *Hermite-Hadamard type inequalities for multiplicatively h-preinvex functions*, Turk. J. Anal. Number Theory, **9**(3) (2021), 65–70. https://doi.org/10.12691/tjant-9-3-5

[42] S. Özcan, A. Urus, S. I. Butt, *Hermite–Hadamard-type inequalities for multiplicative harmonic s-convex functions*, Ukr. Math. J., **76**(9) (2024), 1537–1558. https://doi.org/10.1007/s11253-025-02404-4

[43] M. Umar, S. I. Butt, Y. Seol, *Hybrid fractional integral inequalities in multiplicative calculus with applications*, Fractals, **33**(1) (2025), Article ID 2550019. https://doi.org/10.1142/S0218348X25500197

[44] H. Budak, B. B. Ergün, *On multiplicative conformable fractional integrals: Theory and applications*, Bound. Value Probl., **2025** (2025), Article ID 30. https://doi.org/10.1186/s13661-025-02026-6

[45] J. E. Pečarić, Y. L. Tong, *Convex Functions, Partial Orderings, and Statistical Applications*, Academic Press, 1992.

[46] C. Niculescu, L. E. Persson, *Convex Functions and Their Applications*, Vol. 23, Springer, New York, 2006.

[47] A. A. Kilbas, H. M. Srivastava, J. J. Trujillo, *Theory and Applications of Fractional Differential Equations*, Vol. 204, Elsevier, Amsterdam, 2006.

[48] F. Jarad, E. Ugurlu, T. Abdeljawad, et al., *On a new class of fractional operators*, Adv. Differ. Equ., **2017** (2017), Article ID 247. https://doi.org/10.1186/s13662-017-1306-z